CHALMERS
UNIVERSITY OF TECHNOLOGY

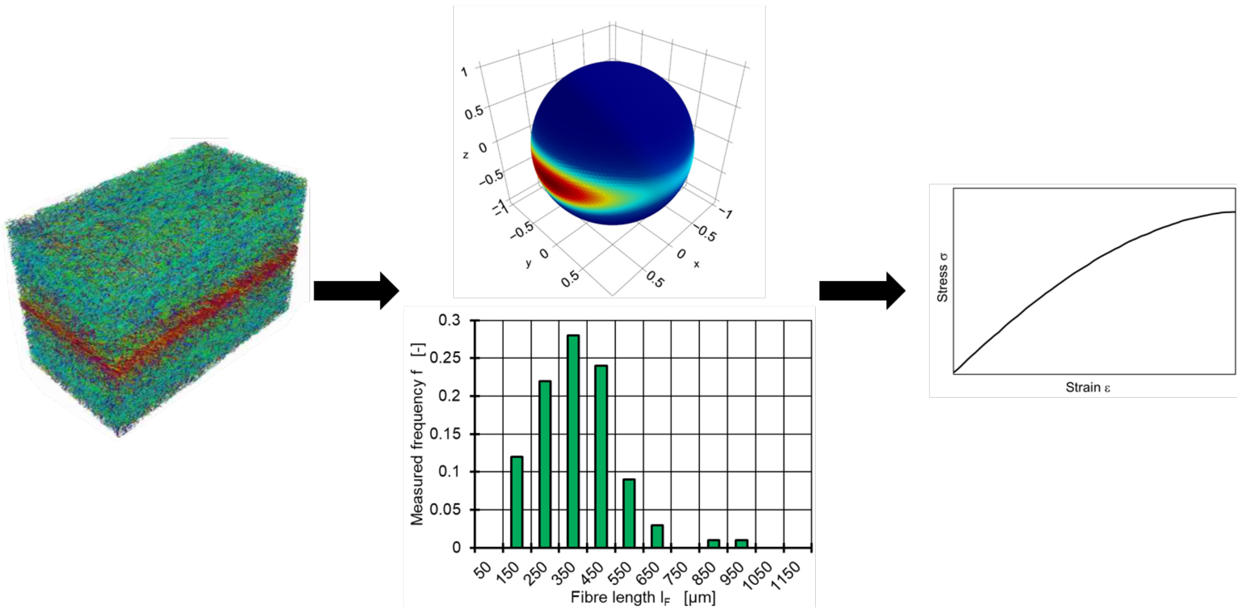

Micro-mechanical modelling of length distributions in short fibre reinforced composites

Using the two-step Orientation Averaging method

Master's thesis in Polymer Engineering

NOAH MENTGES

DEPARTMENT OF INDUSTRIAL AND MATERIALS SCIENCE
DIVISION OF MATERIAL AND COMPUTATIONAL MECHANICS

CHALMERS UNIVERSITY OF TECHNOLOGY
Gothenburg, Sweden 2021
www.chalmers.se

Master's thesis 2021

Micro-mechanical modelling of length distributions in short fibre reinforced composites

Using the two-step Orientation Averaging method

NOAH MENTGES

CHALMERS
UNIVERSITY OF TECHNOLOGY

Department of Industrial and Materials Science
Division of Material and Computational Mechanics
Chalmers University of Technology
Gothenburg, Sweden 2021

Micro-mechanical modelling of length distributions in short fibre reinforced composites
Using the two-step Orientation Averaging method
NOAH MENTGES

Supervisor: Mohsen Mirkhalaf, Physics Department at Gothenburg University
Examiner: Martin Fagerström, Department of Industrial and Materials Science

Master's Thesis 2021
Department of Industrial and Materials Science
Division of Material and Computational Mechanics
Chalmers University of Technology
SE-412 96 Gothenburg
Telephone +46 31 772 1000

Cover: Path from a local micro-CT scan [27] over a statistical representation of fibre length distribution and fibre orientation distribution of the composite to a homogenised material response.

Typeset in LaTeX
Printed by Chalmers Reproservice
Gothenburg, Sweden 2021

Micro-mechanical modelling of length distributions in short fibre reinforced composites
Using the two-step Orientation Averaging method
NOAH MENTGES
Department of Industrial and Materials Science
Chalmers University of Technology

Abstract

The material behaviour of short fibre reinforced composites is dependent on several micro-structural properties, such as the fibre orientation distribution and the geometrical fibre properties. Hence, in order to accurately predict the mechanical response of these materials, micro-mechanical models are used. Those models estimate a homogenised material response for these rather heterogeneous materials.
The length of the short fibres inside the composite is not uniform due to the manufacturing process of these materials. Hence, it is necessary to represent the distribution of fibre lengths inside a composite within the micro-mechanical model. In this work, a two-step Orientation Averaging model is extended to account for fibre length distributions for the linear elastic and elasto-plastic material behaviour. Three different methods for modelling the fibre length distributions are investigated and compared. Two of them are then implemented for further investigations. The first method uses Unit Cell simulations for different fibre length classes, which are combined to a composite behaviour in an additional averaging scheme. For the second method, a single representative fibre length is obtained from the fibre length distribution, and the two-step Orientation Averaging is applied with this single fibre length. For that, a novel method for a representative fibre length is presented with the stiffness-averaged fibre length.
The predictions obtained with the models show good agreement with the experimental results as well as in comparison to each other. Due to the better computational performance, the method using a single representative fibre length is preferred and recommended for the ongoing investigations.

Keywords: Composite mechanics, Short fibre reinforced composites, Micro-mechanics, Orientation Averaging, Fibre length distribution, Elasto-plasticity, Fibre-matrix debonding.

Acknowledgements

This thesis was written during an international exchange program organised by the IDEA League in cooperation with the Institute of Plastics Processing (IKV) at RWTH Aachen University and the Department of Industrial and Materials Science at Chalmers University of Technology. I want to thank these institutions for their support in making this exchange possible for me.
I want to thank my supervisor Mohsen Mirkhalaf, Assistant Professor at the Department of Physics at the University of Gothenburg, who contributed greatly to the success of the work with his helpful advice and fruitful discussion about the many challenges I faced during the project. His revision of the thesis drafts improved the scientific value of the report significantly. Hakan Çelik, Research Assistant at the Institute of Plastics Processing, acted as supervisor of my thesis on behalf of my home university, RWTH Aachen University. During our online meetings, he supported my work with helpful suggestions and new perspectives in several occasions. Further, I want to thank Martin Fagerström, Associate Professor at the Division of Materials and Computational Mechanics, Department of Industrial and Materials Science, who acted as examiner of the thesis. He contributed many helpful comments and suggestions in the project and revising the thesis, and provided the necessary infrastructure for the success of this work, such as the access to the departments facilities and computational resources.
I always enjoyed the time I spent at the Division of Material and Computational Mechanics. This is especially thanks to the many colleagues at the division who warmly welcomed me into their community and also included me in common leisure activities. I would also like to express my gratitude for that. This friendly atmosphere certainly contributed to the success of the project.
Finally, I would like to thank my family and friends for their everlasting support during the international experience and the thesis project itself.

The numerical simulations in this work were mostly conducted on resources provided by the Swedish National Infrastructure for Computing (SNIC) at Chalmers Centre for Computational Science and Engineering (C3SE) partially funded by the Swedish Research Council through grant agreement no. 2018-05973.

Noah Mentges, Aachen, April 2021

CONTENTS

LIST OF FIGURES

LIST OF TABLES

SUMMARY

Descriptors: fibre length, fibre orientation, mechanical load, micromechanics, simulation, material models

Keywords: micro-mechanical modelling, Orientation Averaging, fibre length distribution

For the design of short fibre reinforced plastic components, it is essential to make efficient use of the locally varying reinforcement properties. Consequently, it is important to understand the material-specific behaviour and to model it appropriately.

In addition to the material properties of the composites, the locally variable material parameters fibre volume content, orientation distribution and length distribution have a significant impact on the mechanical behaviour of an SFRC. Current material models usually account for the fibre volume content and the fibre orientation distribution. However, the fibre length distribution is approximated by a single average fibre length. The two-stage Orientation Averaging model uses numerical simulations of a single fibre Unit Cell to capture the homogenised material response of a unidirectional SFRC with a defined fibre volume fraction. For the elasto-plastic material response, a transversal isotropic surrogate model is calibrated based on the numerical simulations, providing an analytical description of the homogenised material response. In a second step, the fibre orientation distribution is introduced by imposing different Unit Cell orientations and combining them to obtain an average homogenised material response of the composite.

The impact of fibre length distributions is investigated and modelled using three different approaches. The first method uses unidirectional RVEs with multiple fibres representing the fibre length distribution. Second, the Orientation Averaging algorithm is applied with a second averaging method over the range of fibre lengths. This requires multiple Unit Cell simulations, each representing a fibre length class within the range of the fibre length distribution. Finally, the representation of the fibre length distribution with a single fibre length is investigated. Three different representative fibre lengths are considered. These include a novel approach called stiffness-weighted average fibre length. Some initial theoretical analysis of the three proposed methods leads to the conclusion that the latter two are the most promising methods for a comprehensive and simultaneously time-efficient modelling technique for the Orientation Averaging process.

The implemented models are applied on examples from the literature and compared to experimental results. Both fibre length averaging, and the use of single representative fibre lengths show convincing predictive capabilities in both the linear elastic and elasto-plastic loading domains. The comparison of the two methods shows great similarities with a deviation in the predicted stress response of ±3 %. Considering the considerable advantage in computational effort resulting from the use of only a single representative fibre length, this method is assessed as advantageous. Compared to the fibre length averaging model, the stiffness-averaged fibre length usually gives the closest prediction. Figure 0.1 gives an overview of the problem and the solutions considered.

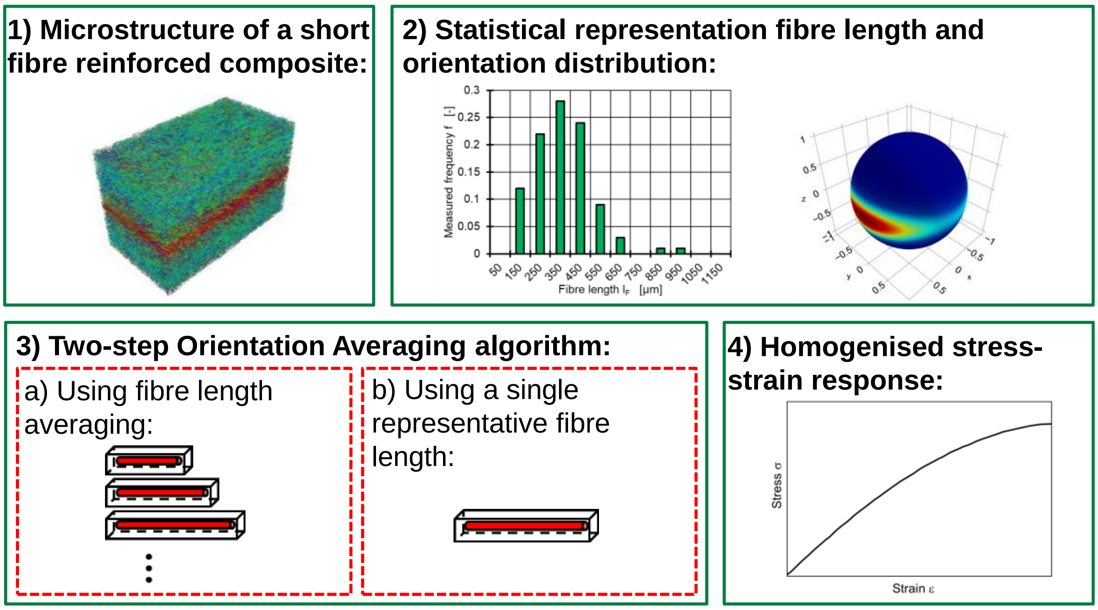

Figure 0.1: Modelling fibre length distributions in short fibre reinforced composites using Orientation Averaging (CT-Scan from [27]).

An investigation of the elasto-plastic orientation averaging predictions reveals a significant overestimation of the composite's stress response at higher strain loads. This is traced back to the negligence of material damage in the elasto-plastic material model. As a common failure mechanism in SFRC, fibre-matrix debonding is implemented in the numerical Unit Cell model and the surrogate material model is calibrated based on these simulations to provide an initial proof of concept for modelling material damage with the present material model.

The results of the Unit Cell simulation underestimate the stress behaviour of the material in the unidirectional composite significantly. Nevertheless, a surrogate material model is calibrated using the simulation results and an Orientation Averaging prediction is calculated. The application of this method to an exemplary material dataset reveals weaknesses in modelling material damage with the currently implemented Orientation Averaging model. The problems are identified, and possible solutions are presented.

1 INTRODUCTION

The usage of short fibre reinforced composites (SFRCs) has increased over the recent years in automotive applications as well as in other high-performance structural components [21]. These materials benefit from the combination of high specific mechanical properties and the relatively easy processing. In the case of short fibre reinforced plastics, the material can be formed in the injection moulding process. Hence, parts made from these materials can be produced in large series with relatively low production costs [21].

During the injection moulding process, the processed fibres are exposed to great stresses due to the viscous melt flow. Consequently, fibres break during the processing due to contact with the screw or tool walls, or fibre-fibre interaction [45]. This results in a distribution of fibre lengths in the injection moulded SFRC parts.

Designing SFRC components requires a sufficient understanding of the complex material behaviour. This behaviour is mainly influenced by the fibre and matrix properties as well as the locally varying microscopic configuration of the material. The latter is defined by the fibre volume fraction, fibre orientation distribution, and the fibre length distribution. The parameters must be represented adequately in a material model [9]. In order to describe the macroscopic mechanical behaviour of the material, micro-mechanical models have been developed. Different modelling approaches using analytical, semi-empirical or computational homogenisation methods have been applied. Computational homogenisation methods, using Representative Volume Elements (RVEs), create a statistical, geometric example of the micro-structure to calculate a homogenised material response.

In case of simple two component SFRCs, those usually cuboidal structures consist of two phases, the fibres and the surrounding matrix. The RVE is generated using a randomised fibre placing algorithm, which considers the desired fibre volume fraction and FOD. The geometry of the RVE is considered as periodic, meaning that the RVE can be interpreted as being surrounded by copies of itself [55]. Periodic Boundary Conditions (PBCs) are applied, in order to eliminate the influence of boundary effects on the microscopic stress state. The RVE is embedded in a periodic structure by kinematic interconnections between the opposing surfaces of the RVE. For obtaining the anisotropic direction dependent material behaviour, 6 independend load cases are simulated in the most generic case. Normal and shear loads are applied sequentially on the three main directions defined by the RVE surfaces [18].

Using microstructure RVEs shows very strong predicting capabilities [3]. On the other hand, in practice, high computational costs and difficulties in the RVE-geometry generation are a limiting factor for the applicability of this method. For example, for higher geometrical fibre aspect ratios and volume fractions, the generation of such RVEs for the homogenisation methods becomes more difficult [37]. These difficulties are a good motivation for using other modelling techniques.

Analytical homogenisation methods have the benefit of delivering reproducible and computationally more efficient solutions to the mechanical response of the composite [49]. As one alternative, the two-step Orientation Averaging (OA) approach, following the study by

Advani and *Tucker* can be used [1]. For this method, first, the material response of a unidirectional short fibre composite is obtained and, in a second step, the material behaviour with different orientations is combined using an interaction assumption. Analytical mean-field homogenisation methods can be used to describe the material response in the unidirectional composite. Examples for these methods are the Mori-Tanaka, the double inclusion, and the self-consistent model [49]. *Mirkhalaf* et al. developed a two-step Orientation Averaging method, using the homogenised material response from the numerical simulation of a single fibre Unit Cell (UC) [36, 39]. The model was used to predict the material response of a SFRC in the linear elastic and in the elasto-plastic domain. In a later project, the model was incorporated in a macroscopic finite element code by Castricum et al. [13]. However, only one single fibre length was considered for the simulations.

In this work, the two-step Orientation Averaging model for SFRCs is extended to also consider the distribution of fibre lengths. Therefore, two modelling methods are proposed. The first uses the full fibre length distribution, by adding another averaging scheme to the method. The other method reduces the fibre length distribution to a single representative fibre length. A novel approach for obtaining this representative fibre length is proposed as the stiffness-average of the fibre length distribution. The developed models are implemented in Python and tested on representative results taken from the literature.

The following parts of the report are structured as follows. In Chapter 2, the micro-mechanical modelling approach, two-step Orientation Averaging, is. In the second part, the modelling of fibre-matrix interfaces in numerical simulations is handled. Chapter 3 addresses the impact of fibre length distributions on the homogenised composite properties and gives suggestions on how to represent them in a micro-mechanical model. Subsequently, in Chapter 4, the implementation of the most essential functions into the Python-script for the Orietnation Averaging model is explained. The extended model is then tested on results from the literature in Chapter 5. In Chapter 6 the presented work is concluded and an outlook on possible further tasks in this project is given.

2 THEORY

In the following part, the theoretical basics on which this work is based on are explained. First, a comprehensive presentation of the two-step Orientation Averaging algorithm is given. In a second part, the methods of modelling cohesive behaviour in numerical simulations are studied.

2.1 Two-step Orientation Averaging method

In contrast to the numerical volumetric homogenisation method using RVE structures, the two-step Orientation Averaging method is an analytical, micromechanics-based homogenisation method for short fibre composite materials. Two homogenisation schemes are applied in this method, first presented in *Advani* and *Tucker* [1]. First, on the local level, the material response of a single fibre surrounded by matrix is obtained. And subsequently, on the global, composite level, the fibre orientation distribution (FOD) is introduced in the Orientation Averaging. In the two-step OA-method, the local material response is obtained by volumetric homogenisation of a single fibre Unit Cell. Figure 2.1 shows a schematic workflow of both volumetric homogenisation and two-step Orientation Averaging procedure. The volumetric

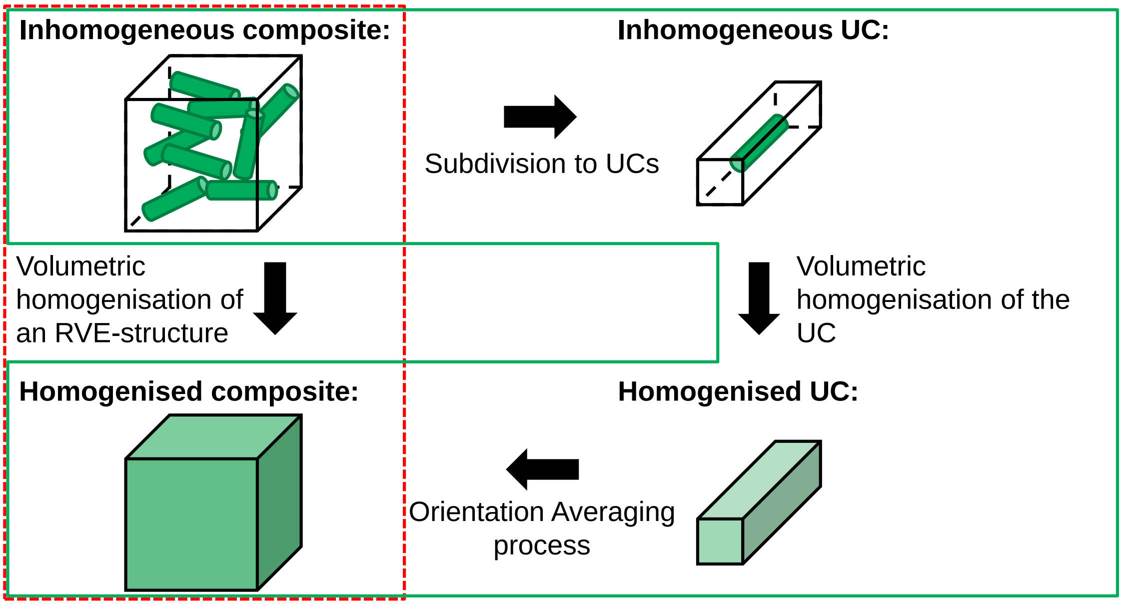

Figure 2.1: Workflow of the Orientation Averaging method in comparison with the volumetric homogenisation method [39].

homogenisation method takes the direct path from an inhomogeneous composite RVE to the homogenised properties, whereas the OA-method takes the aditional step of obtaining the material properties of a unidirectional composite. Besides the advantages of computational savings, the OA-method is also capable of creating reproducable results, since it is not dependent on a randomly generated structure, such as an RVE. In the following chapters, the two-step Orientation Averaging method will be explained in more detail. The presented equations are partially based on tensor algebra. Information about the used notation style and tensor operations can be found in Appendix 0.

2.1.1 Describing the fibre orientation distribution

In order to introduce the orientation of fibres in a micro-mechanical model, a mathematical description of the local constitution must be found. The orientation of a fibre in a 3D space can be described by a unit vector $\boldsymbol{p}$ pointing along the axial direction of the fibre. With the constant length of the orientation vector $|\boldsymbol{p}| = 1$ it can be described in spherical coordinates by the azimuthal angles ϕ and θ. The construction of the vector p in cartesian and spherical coordinates is illustrated in Figure 2.2.

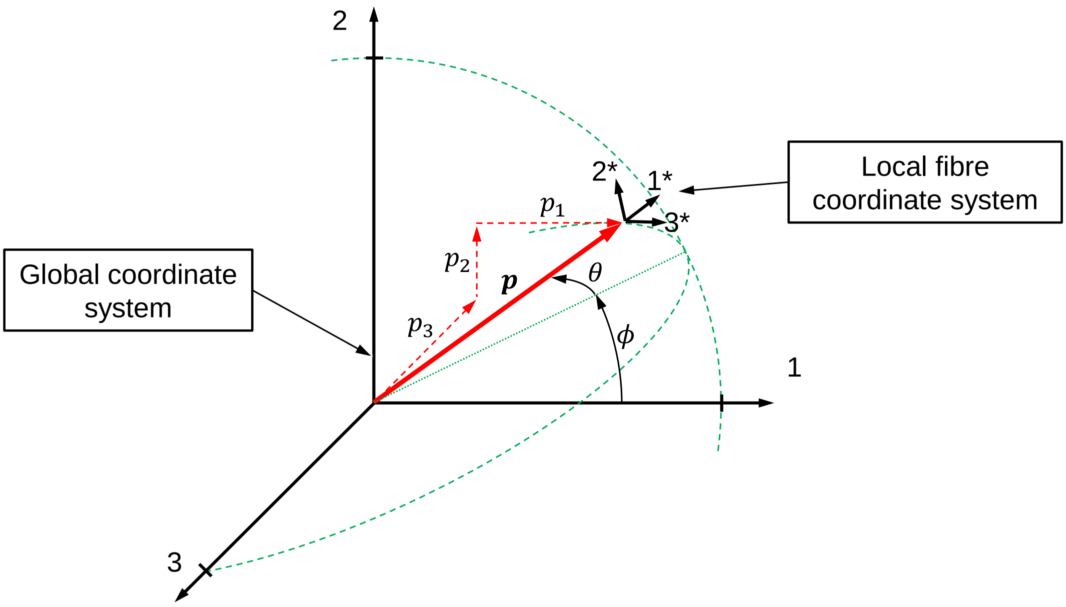

Figure 2.2: Construction of the fibre orientation vector p in cartesian and spherical coordinates.

By defining $\phi = \theta = 0$ as the 1-direction, which is defined as the fibre direction in the local constitution, the orientation vector $\boldsymbol{p}$ can then be written in dependence on the azimuthal angles as

$$\boldsymbol{p} = \begin{pmatrix} \cos\phi\cos\theta \\ \sin\phi\cos\theta \\ -\sin\theta \end{pmatrix}, \tag{2.1}$$

$$\boldsymbol{R}(\boldsymbol{p}) = \boldsymbol{R}(\phi,\theta) = \begin{pmatrix} \cos\phi\cos\theta & \sin\phi & -\cos\phi\sin\theta \\ -\sin\phi\cos\theta & \cos\phi & \sin\phi\sin\theta \\ \sin\theta & 0 & \cos\theta \end{pmatrix}. \tag{2.2}$$

In Equation (2.2), $\boldsymbol{R}$ represents a transformation tensor which performs a coordinate transformation from the global coordinate system to the local fibre coordinate system.

The set of all possible orientation vectors $\boldsymbol{p}$ spans the unit sphere. Hence, the fibre orientation distribution function (FODF) $\psi(\boldsymbol{p})$ can be represented by a function of the angles ϕ and θ. Two main conditions apply to the FODF. It is symmetrical and normalised, meaning that

$$\psi(\boldsymbol{p}) = \psi(-\boldsymbol{p}), \tag{2.3}$$

$$\oint \psi(\boldsymbol{p})\, d\boldsymbol{p} = \int_{\phi=0}^{2\pi} \int_{\theta=-\frac{\pi}{2}}^{\pi\backslash 2} \psi(\theta,\phi)\ \cos\theta\ d\theta\ d\phi = 1. \tag{2.4}$$

Additionally, a time continuity condition is stated, which, however, is irrelevant for this report. [1]

An FOD can also be described as an even order tensor $\boldsymbol{a}$, the fibre orientation distribution tensor (FODT). *Advani* and *Tucker* proposed a method on how these tensors are constructed. The most commonly used tensors are the second and fourth order FODTs. Hence, they are presented in the following relations:

$$a_{ij} = \oint p_i p_j \psi(\boldsymbol{p})\, d\boldsymbol{p}, \tag{2.5}$$

$$a_{ijkl} = \oint p_i p_j p_k p_l \psi(\boldsymbol{p})\, d\boldsymbol{p}. \tag{2.6}$$

For a finite set of fibre orientations, the FODT can be obtained by the sum over all fibre orientation vectors divided by the number of orientations in the set. The FODT is completely symmetric, meaning that

$$a_{ij} = a_{ji}, \tag{2.7}$$

$$a_{ijkl} = a_{jikl} = a_{kijl} = a_{lijk} = a_{klij} \dots \tag{2.8}$$

Additionally, it can be shown that the diagonal of the second order FODT sums up to 1. Higher order FODTs can easily be converted to the lower orders according to the following

$$a_{ij} = a_{ijkk}, \tag{2.9}$$

$$a_{ijkl} = a_{ijklmm}. \tag{2.10}$$

Conversions from lower order FODTs to higher order ones are ambiguous and require closure approximations.The ordinary rules for coordinate transformations can be applied to FODTs. [1]

Orientation distributions are often presented as FODTs, due to their compact notation. However, to perform the Orientation Averaging, a FODF is necessary to assign certain probabilities to the fibre orientations. Although, the transformation from a FODF to a FODT is unambiguous, the transformation back to one explicit FODF is not straight-forward [10]. Multiple distributions of fibre orientations could lead to the same FODT. Hence, assumptions must be taken, to ensure an unambiguous transformation in this direction. Different methods have been developed to address this problem. *Onat* and *Leckie* present a spherical harmonics based approach, in which FODF can be derived directly from the FODT [1, 47]. Another method, presented by *Breuer*, *Stommel et al.* relies on the assumption of maximum entropy

[10]. Fibres are expected to follow a maximum scattering inside the boundaries of the FODT. For this, a distribution function following a *Bingham*-distribution is applied [6].

A *Bingham*-distribution represents a π-periodic projection of a normal distribution on the unit sphere. It is defined by the following equation:

$$f(\boldsymbol{p}) = q \cdot e^{s_1 p_1^2 - s_3 p_3^2}, \tag{2.11}$$

with the parameters s_1 and s_3 defining the shape of the FOD and q being the normalising constant.

In Figure 2.3 some FODFs using Bingham distributions with different parameters are presented. It can be seen that for both parameters equal to 0 a random distribution is found.

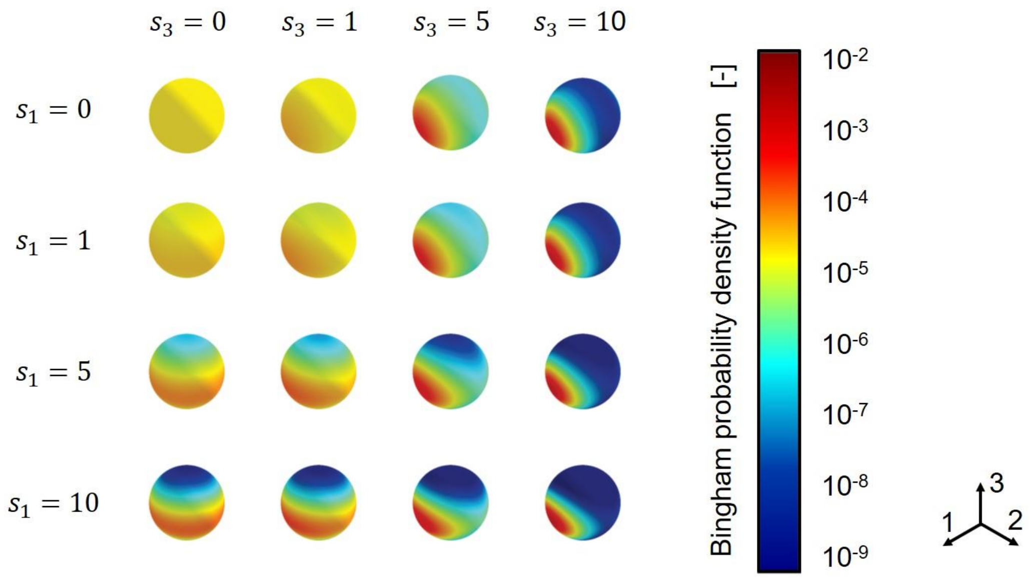

Figure 2.3: The effect of the parameters s_1 and s_3 on the Bingham probability distribution function.

With increasing parameters, the FODF becomes more has a higher concentration in the 1-direction. Note that the global maximum of this probability density function is found at an orientation in 1-direction ($p_1 = 1$), independent from the parameters. The global minimum is found for $p_3 = 1$. A FOD following a *Bingham*-distribution results in a diagonal shaped second order FODT. For different orientations of the distribution's extreme points, a corresponding coordinate transformation must be performed on the fibre orientations $\boldsymbol{p}$ and the FODT $\boldsymbol{a}$. In general, every second order FODT can be converted into a diagonal shape by spectral decomposition [30]. This means that a rotational tensor $\boldsymbol{R}$ can be found that, if applied to the FODT, it results in a diagonal tensor $\boldsymbol{\Lambda}$

$$\boldsymbol{\Lambda} = \boldsymbol{R} \cdot \boldsymbol{a} \cdot \boldsymbol{R}^T, \quad \boldsymbol{\Lambda} = diag(\lambda_1, \lambda_2, \lambda_3), \tag{2.12}$$

with λ_i being the eigenvalues of the FODT in descending order ($\lambda_1 \leq \lambda_2 \leq \lambda_3$) and the column vectors of $\boldsymbol{R}$ representing the principal directions of the FODT [30]. According to this, in order to obtain the FODF for any given FODT, first, the FODT needs to be transformed into a diagonal shape. Then, an optimisation is conducted to find the parameters for the Bingham distribution with the orientation vector $\overline{\boldsymbol{p}_i} = \boldsymbol{R}_C^T \cdot \boldsymbol{p}_{\boldsymbol{\Lambda},\mathrm{i}}$ transformed into the principal directions of $\boldsymbol{a}$. The method for obtaining the Bingham distribution parameters is described in *Breuer, Stommel et al* [30]. A visualisation of the processes for obtaining the fibre orientation distributions is given in Figure 2.4.

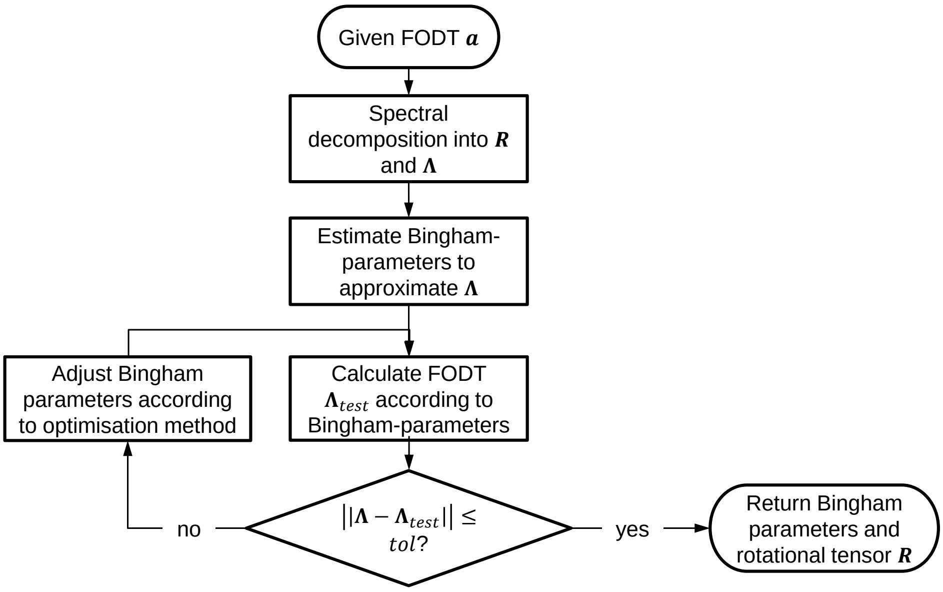

Figure 2.4: Simplified algorithm workflow for obtaining the FODF from the FODT.

2.1.2 Volumetric homogenisation of the single fibre unit cell

The material response of a unidirectional composite can be obtained analytically using so called mean field homogenisation methods. Basic methods of this kind assuming equal stresses or strains in the constituents of the composites deliver upper and lower bounds for the resulting composite stiffnesses independent from the orientation or shape of the inclusion. However, their predictions are usually far off the actual material behaviour. More sophisticated models use mathematical approximations of the inclusions shape in form of an ellipsoid. [49]

Using numerical models enables the user, to use more realistic geometries of the inclusions such as the cylinder shape. Additionally, more sophisticated effects within the material, such as the fibre-matrix boundary can be investigated more thoroughly. In this case, the unidirectional composite is modelled as a single fibre Unit Cell, embedded in a field of copies of itself, defined by periodic boundary conditions.

The geometry of a UC consists of a cuboidal block of matrix material with a quadratic cross section to ensure obtaining the transversal isotropic properties of the unidirectional (UD) UC. The cylindrical fibre is placed in the centre of the block. To fulfil the required fibre volume fraction φ, the dimensions of the UC are dependent on the fibre geometry (length l_{fibre} and diameter d_{fibre}) and the fibre volume fraction itself

$$\varphi = \frac{\pi \cdot l_{fibre} \cdot d_{fibre}^2}{4 \cdot l_{UC} \cdot b_{UC}^2}, \tag{2.13}$$

with the UC-length in fibre direction l_{UC}, and width b_{UC} for the fibre perpendicular directions. These restrictions leave one open degree of freedom for choosing the appropriate UC-geometry.

Figure 2.5 shows that the impact of the relative UC-length (l_{UC}/l_{fibre}) on the homogenised elastic properties of the UC is quite significant. Investigating the fibre parallel UC-stiffness E_{11}, with a relative UC-length equal to one, shows high composite stiffnesses, approximating a continuous fibre reinforced composite. Whereas, choosing the maximum value for l_{UC}, when $b_{UC} = d_{fibre}$, results in a minimum UC-stiffness.

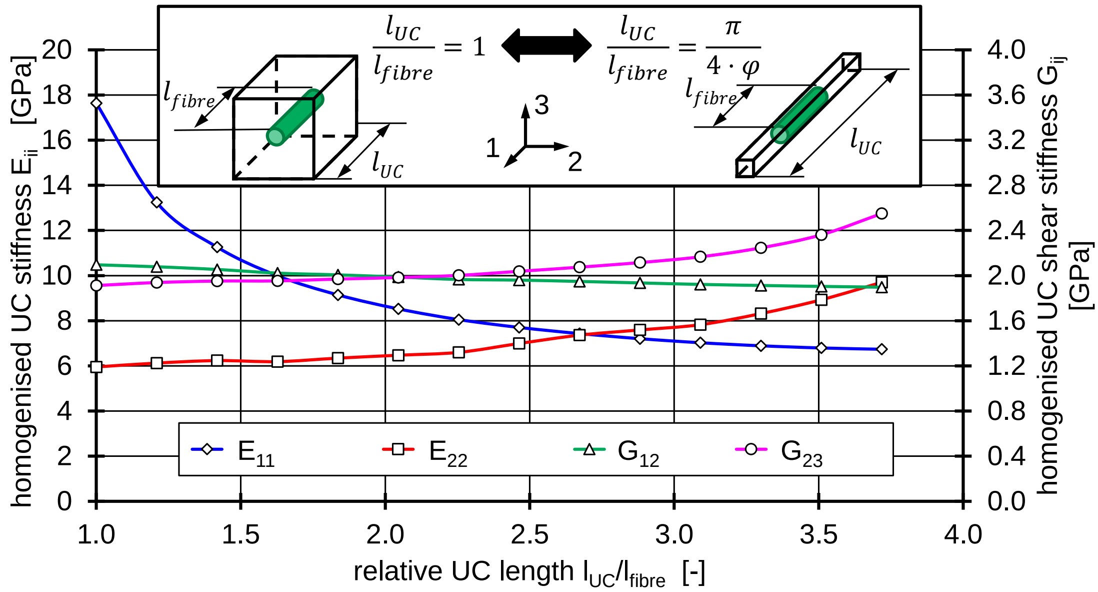

Figure 2.5: Influence of the relative UC-length on the homogenised elastic properties of a single fibre Unit Cell.

This investigation shows that for representing the UC-stiffness adequately, a reasonable method for obtaining the UC-geometry must be used. The method in this work, proposed by *Modniks* and *Andersons*, establishes equidistance between the fibre and UC-surface [40]. The shortest distance between fibre and matrix in all directions is set to a fixed value c, resulting in the new relation

$$\varphi = \frac{\pi \cdot l_{fibre} \cdot d_{fibre}^2}{4 \cdot \left(l_{fibre} + 2c\right) \cdot \left(d_{fibre} + 2c\right)^2}. \tag{2.14}$$

The distance c can be obtained by solving a cubic equation. Note that with this method, the relative UC-length is then dependent on the fibre length. In Figure 2.6, a drawing of the UC is given. The coordinate system in the bottom of the Figure indicates the local coordinate system of the single fibre. Here, the fibre rotational axis is defined in 1-direction. Consequently, the 2- and 3-directions are perpendicular to the fibre axis. In the numerical model the fibre and matrix are assumed to be ideally connected across the full fibre surface including the fibre tips. Periodic boundary conditions are applied

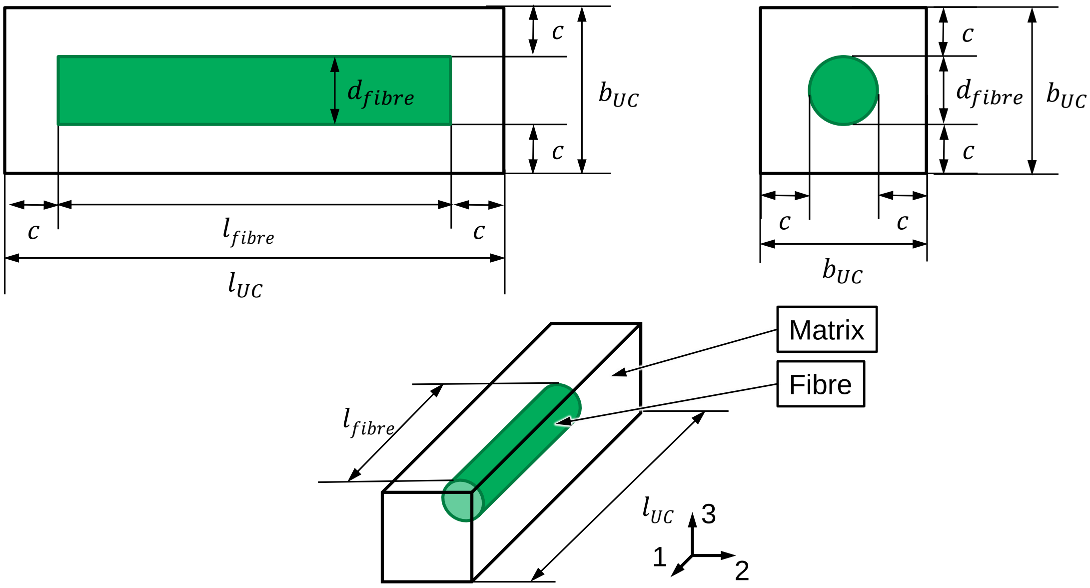

Figure 2.6: The Unit Cell-geometry with equidistant spacing to the Unit Cell boundaries [40].

For an anisotropic material response, six individual load cases have to be applied to fully define the homogenised material parameters. Normal and shear load cases are applied each in three directions. Those load cases are depicted in Figure 2.7. Assuming symmetries in the material behavior can reduce the amount of simulations needed. In this case of a UC-geometry, the number of independent simulations is reduced to 4 due to redundancy in the 2- and 3-directions. The necessary loads in that case are longitudinal and transverse normal and shear loads [18].

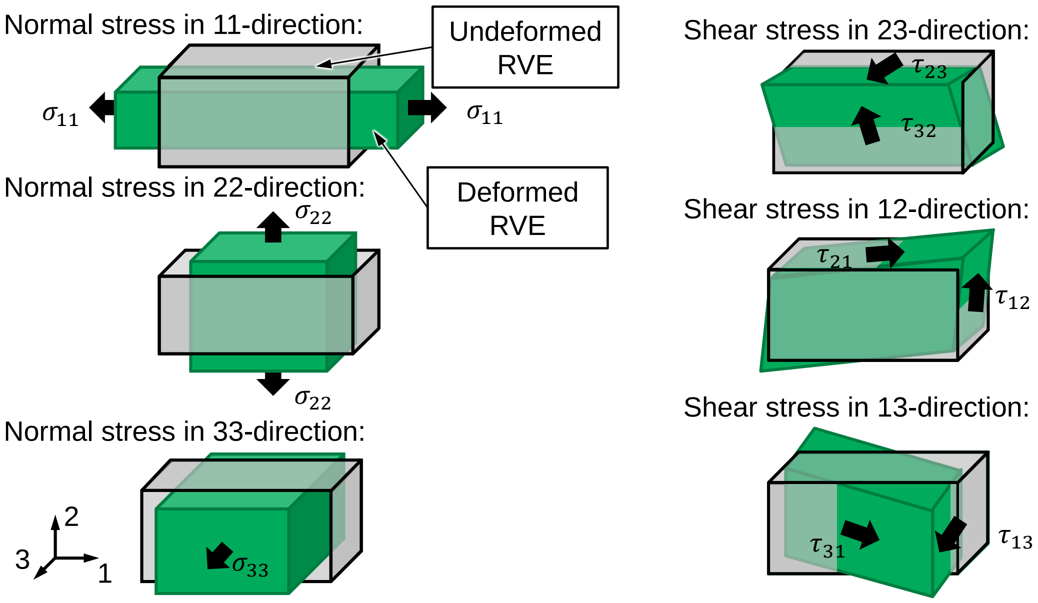

Figure 2.7: Uniaxial stress load-cases for obtaining the complete homogenised composite response.

The homogenised material response is then obtained by extracting the forces $F_j^{RP,i}(t)$ and displacements $u_j^{RP,i}(t)$ in j-direction from reference points (RPs) connecting the opposing surfaces of the UC perpendicular to the i-direction. These values can then be converted to stresses σ_{ij} and strains ε_{ij} using the following equations:

$$\sigma_{ij}(t) = \frac{F_j^{RP,i}(t)}{A_i}, \tag{2.15}$$

$$\varepsilon_{ij}(t) = \frac{u_j^{RP,i}(t)}{l_i}. \tag{2.16}$$

where l_i represents the length of the UC in i-direction and A_i is the area of the cross-section of the UC normal to the i-direction. Note that these equations result in engineering stresses and strains, which are only applicable for small strains. From the simulation results, the full homogenised material response can be obtained. Since the methods for linear elastic and elasto-plastic behaviour are different, they are described seperately in the following subsections.

2.1.2.1 Linear elastic homogenisation

For the linear elastic case, both the fibre and the matrix materials are modelled with linear elastic properties. Small strain increments are applied in the different load directions. The resulting fourth order compliance matrix $\boldsymbol{S}^{\mathbf{4}}$ can then be identified from the four simulations using the inverse *Hooke's* law:

$$\boldsymbol{\varepsilon} = {}^{4}\boldsymbol{S} : \boldsymbol{\sigma}. \tag{2.17}$$

In Voigt notation the case becomes clearer and the identification of the compliance matrix is presented in Figure 2.8. Due to the fact that uniaxial stress loads are applied and, therefore, the

Strain direction

Load direction	11	22	33	23	13	12
11	$\frac{\varepsilon_{11}}{\sigma_{11}}$	$\frac{\varepsilon_{11}}{\sigma_{22}}$	$\frac{\varepsilon_{11}}{\sigma_{33}}$	$\frac{\varepsilon_{11}}{\tau_{23}}$	$\frac{\varepsilon_{11}}{\tau_{13}}$	$\frac{\varepsilon_{11}}{\tau_{12}}$
22	$\frac{\varepsilon_{22}}{\sigma_{11}}$	$\frac{\varepsilon_{22}}{\sigma_{22}}$	$\frac{\varepsilon_{33}}{\sigma_{33}}$	$\frac{\varepsilon_{11}}{\tau_{23}}$	$\frac{\varepsilon_{22}}{\tau_{13}}$	$\frac{\varepsilon_{22}}{\tau_{12}}$
33	$\frac{\varepsilon_{33}}{\sigma_{11}}$	$\frac{\varepsilon_{33}}{\sigma_{22}}$	$\frac{\varepsilon_{22}}{\sigma_{33}}$	$\frac{\varepsilon_{11}}{\tau_{23}}$	$\frac{\varepsilon_{33}}{\tau_{13}}$	$\frac{\varepsilon_{33}}{\tau_{12}}$
23	$2\frac{\varepsilon_{23}}{\sigma_{11}}$	$2\frac{\varepsilon_{23}}{\sigma_{22}}$	$2\frac{\varepsilon_{23}}{\sigma_{33}}$	$2\frac{\varepsilon_{23}}{\tau_{23}}$	$2\frac{\varepsilon_{23}}{\tau_{13}}$	$2\frac{\varepsilon_{23}}{\tau_{12}}$
13	$2\frac{\varepsilon_{13}}{\sigma_{11}}$	$2\frac{\varepsilon_{13}}{\sigma_{22}}$	$2\frac{\varepsilon_{13}}{\sigma_{33}}$	$2\frac{\varepsilon_{13}}{\tau_{23}}$	$2\frac{\varepsilon_{13}}{\tau_{13}}$	$2\frac{\varepsilon_{13}}{\tau_{12}}$
12	$2\frac{\varepsilon_{12}}{\sigma_{11}}$	$2\frac{\varepsilon_{12}}{\sigma_{22}}$	$2\frac{\varepsilon_{12}}{\sigma_{33}}$	$2\frac{\varepsilon_{12}}{\tau_{23}}$	$2\frac{\varepsilon_{12}}{\tau_{13}}$	$2\frac{\varepsilon_{12}}{\tau_{12}}$

Simulations:
Uniaxial stress in
11-direction
22-direction
33-direction
23-direction
13-direction
12-direction

Figure 2.8: Identification of the compliance matrix components based on uniaxial stress simulations.

stresses which are not in load direction are equal to zero, for each load case, the compliance matrix can be filled coloumn wise. The transversal isotropy assumption would reduce the number of entries in the compliance matrix to the diagonal entries of the matrix and the non diagonal entries in the upper left quadrant. Moreover, redundancies could be applied to eliminate the equivalent load cases in the isotropic plane. However for the linear elastic case, the commercial software Digimat FE from MSC Software Corporation, Newport Beach CA, USA, is used to derive the elastic parameters [43]. The software provides an automatic elastic properties derivation method, which conducts simulations with uniaxial stress loads in all 6 different load cases. No assumptions are applied and consequently the compliance matrix is filled according to Figure 2.8. However, in case of the resulting stiffness and compliance tensors from the UC simulations, the entries in the negligible directions are significantly smaller than the relevant entries. The resulting stiffness tensor can be used directly in the Orientation Averaging step.

2.1.2.2 Elasto-plastic surrogate model

The homogenised elasto-plastic material behaviour is described using a surrogate model, which is calibrated on the results of the UC-simulations. In this case elasto-plastic properties are defined for the matrix material, while the fibre remains linear elastic. Figures 2.9 and 2.10 give an example for a material response of a UC in the 4 independent load directions, taken from numerical simulations. Note the inverted vertical axis of the graph showing the homogenised

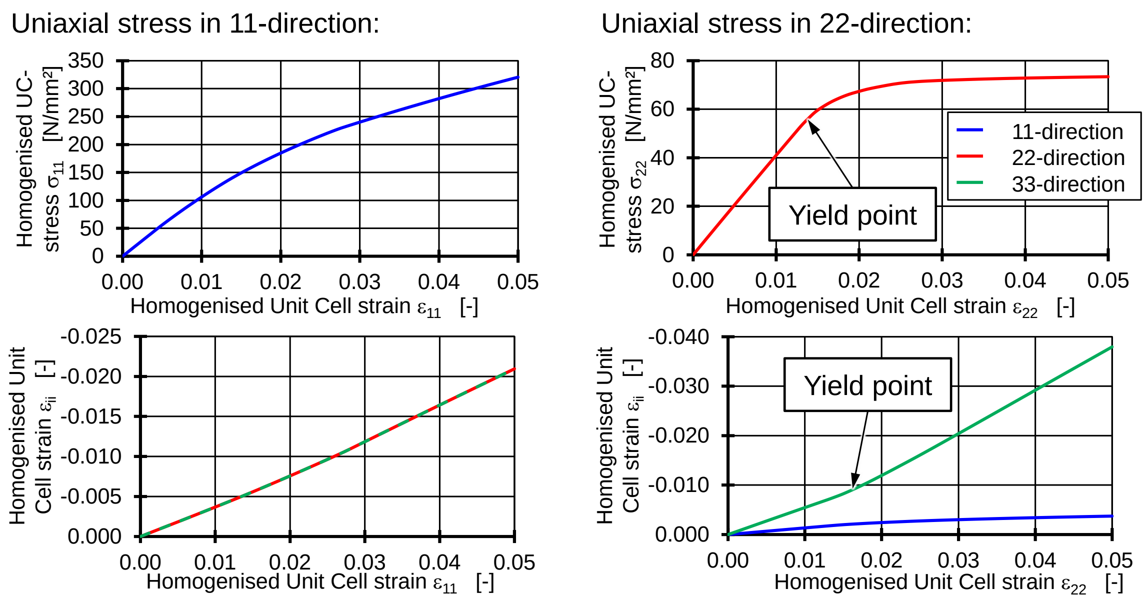

Figure 2.9: Exemplary material response for a uniaxial stress load case on a Unit Cell with elasto-plastic matrix behaviour (normal load cases).

strain response of the Unit Cell in Figure 2.9. The material behaviour is defined by an elastic material response up to a yield point, from which plastic deformations can be observed. In case of the shear loads and the fibre transverse normal load condition (in 22-direction), the yield

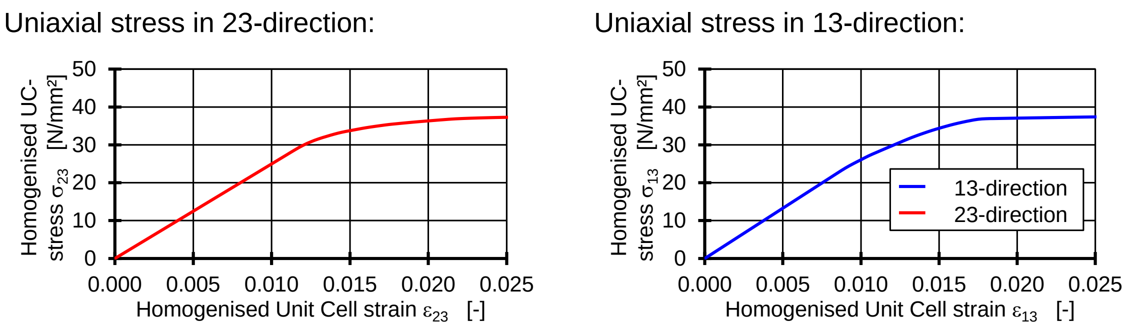

Figure 2.10: Exemplary material response for a uniaxial stress load case on a Unit Cell with elasto-plastic matrix behaviour (shear load cases).

point is more pronounced, whereas for the fibre parallel loading only a relatively small deviation from the linear elastic material behaviour occurs. In case of the normal loading condition, a contraction of the material perpendicular to the load direction is observed. Here, the yield point can be identified as well, with an increased transverse contraction rate. This can be seen especially in the contraction of the 33-direction for the load case in 22-direction in the lower right graph of Figure 2.9. In the following a surrogate model is presented in order to approximate the described material response and obtain the material behaviour for varying loading conditions.

The model consists of a transverse isotropic elastic material model in combination with a transverse isotropic variation of the Hill's yield criterion taken from *Runesson et al.* [50]. With the assumption of the fibre only taking loads in fibre direction, the transverse isotropic can be reduced from 5 to 3 independent parameters in the elastic model and from 4 to 2 independent parameters in the yield criterion. This results in a definition of the elastic stiffness tensor ${}^4\boldsymbol{C}^e$.

$$ {}^4\boldsymbol{C}^e = {}^4\boldsymbol{C}^{e,iso} + (k-1)\left(K + \frac{4G}{3}\right)\boldsymbol{A} \otimes \boldsymbol{A}, \tag{2.18} $$

with ${}^4\boldsymbol{C}^{e,iso}$ representing an isotropic stiffness tensor with independent parameters, defined by the Young's modulus E and Poisson's ratio ν. From those, the parameters K and G can be derived, representing the bulk and shear modulus, respectively. $\boldsymbol{A}$ is a second order structural tensor, representing the fibre orientation in the UC. In this case with the fibre oriented in 1-direction, it is defined as $\boldsymbol{A} = diag(1, 0, 0)$. Factor k in Equation (2.18) introduces the transversal isotropy. In case of $k = 1$, the standard isotropy stiffness tensor is obtained. [50]

The Hill's yield function Φ for the simplified transverse isotropic case, and with the fibre direction in the 1-direction is defined by the following

$$ \begin{aligned} \Phi = \frac{1}{(1-\mathrm{R})\sigma_y^2}&[R[\sigma_{22}-\sigma_{33}]^2 + [\sigma_{11}-\sigma_{22}]^2 + [\sigma_{11}-\sigma_{33}]^2] \\ &+ \frac{2(2R+1)}{(R+1)\sigma_y^2}[[\sigma_{12}]^2 + [\sigma_{23}]^2 + [\sigma_{13}]^2] - \alpha(\varepsilon_{eff}^p), \end{aligned} \tag{2.19} $$

with σ_{ij} representing the current stresses in ij-direction. σ_y defines the yield point for uniaxial stress in the isotropic plane and parameter R relates σ_y to the fibre direction [50]. Finally, α

defines the hardening behaviour of the material model in dependency of an effective plastic strain ε_{eff}^{p}. In previous work [5] an isotropic hardening rule, following a third order polynomial, was chosen for α, which is defined by the relation

$$\alpha\left(\varepsilon_{eff}^{p}\right) = 1 + \kappa_1 \varepsilon_{eff}^{p} + \kappa_2 \left(\varepsilon_{eff}^{p}\right)^2 + \kappa_3 \left(\varepsilon_{eff}^{p}\right)^3, \tag{2.20}$$

with material parameters κ_1, κ_2 and κ_3. The material parameters need to be obtained in the fitting procedure of the surrogate model. This results in 8 independent parameters needed to be fit for the elasto-plastic surrogate model, E, ν and k for the elastic part and σ_y, R, κ_1, κ_2 and κ_3 for the plasticity model. Note that the here presented material model is based on small deformation theory. Hence, if not mentioned accordingly, all presented strains are written as infinitesimal strains.

Obtaining the material response for a given load case with the surrogate model is an iterative process. The method takes the current status of the material as input, represented by the stress, the strain and the effective plastic strain, and the aspired status of the material in the following step. Dependent on the boundary conditions (e.g., uniaxial stress/strain) degrees of freedom need to be disabled. Then a first estimation of the material response is given by assuming a certain strain increment. The corresponding stress is then obtained either directly for the linear elastic domain or by a second iterative process to approximate the yield surface ($\Phi = 0$). The resulting stress state is compared to the boundary conditions and the correct strain response is approximated with a correction term. Figure 2.11 shows a simplified flow chart of the described algorithm.

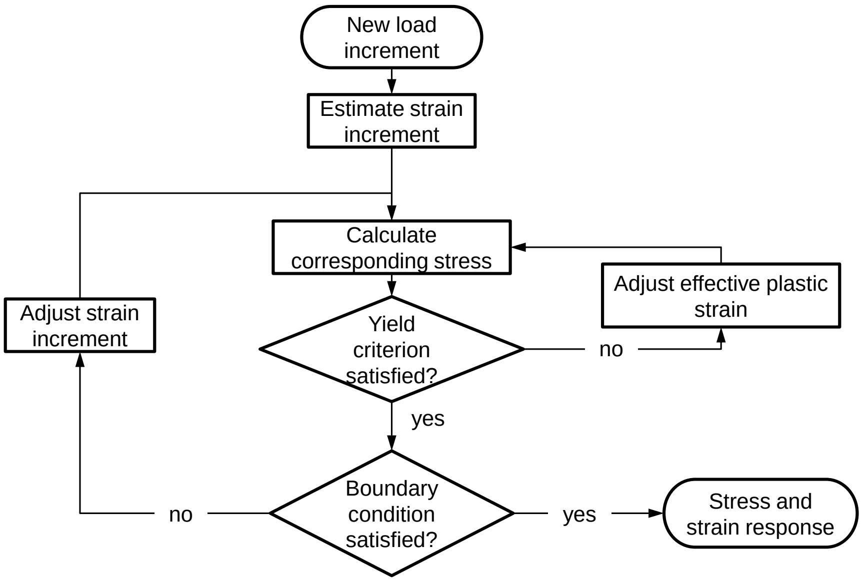

Figure 2.11: Simplified algorithm workflow for the elasto-plastic surrogate material model.

Beneath the stress and strain response, the algorithm also provides an analytical solution to the tangent stiffness tensor ${}^{4}\boldsymbol{C}^{tang}$ which represents the full derivate of the stiffness tensor by the strain tensor. The construction of the tangent stiffness tensor is given by the following equations with $\dot{\boldsymbol{\sigma}}$ and $\dot{\boldsymbol{\varepsilon}}$ as stress and strain increment, respectively:

$$\dot{\boldsymbol{\sigma}} = {}^4\boldsymbol{C}^{tang} : \dot{\boldsymbol{\varepsilon}}, \tag{2.21}$$

$$C_{ijkl}^{tang} = \frac{\partial \sigma_{ij}(t)}{\partial \varepsilon_{kl}(t)}. \tag{2.22}$$

The presented surrogate model was introduced and verified in previous work. For a more detailed explanation of its definition, it is referred to *Mirkhalaf et al.* [36]. The full theory is provided in *Runesson, Steinmann et al.* [50].

2.1.3 Orientation Averaging method

With the tools presented in the previous chapters, one can now proceed with the Orientation Averaging step. The theory behind this method will be discussed in the following chapter, explaining the basic idea and going into further detail by discussing three different interaction assumptions.

To obtain the homogenised material response of the composite, the stresses and strains in the local UC configurations, $\boldsymbol{\sigma}_{UC}$ and $\boldsymbol{\varepsilon}_{UC}$, and the global composite level, $\boldsymbol{\sigma}_C$ and $\boldsymbol{\varepsilon}_C$, are coupled by an averaging scheme.

$$\boldsymbol{\sigma}_C = \oint \psi(\boldsymbol{p}) \boldsymbol{R}^T(\boldsymbol{p}) \cdot \boldsymbol{\sigma}_{UC}(\boldsymbol{p}) \cdot \boldsymbol{R}(\boldsymbol{p})\, d\boldsymbol{p} = \oint \psi(\boldsymbol{p}) \left[\boldsymbol{R}^T(\boldsymbol{p}) \overline{\otimes} \boldsymbol{R}^T(\boldsymbol{p})\right] : \boldsymbol{\sigma}_{UC}\, d\boldsymbol{p}, \tag{2.23}$$

$$\boldsymbol{\varepsilon}_C = \oint \psi(\boldsymbol{p}) \boldsymbol{R}^T(\boldsymbol{p}) \cdot \boldsymbol{\varepsilon}_{UC}(\boldsymbol{p}) \cdot \boldsymbol{R}(\boldsymbol{p})\, d\boldsymbol{p} = \oint \psi(\boldsymbol{p}) \left[\boldsymbol{R}^T(\boldsymbol{p}) \overline{\otimes} \boldsymbol{R}^T(\boldsymbol{p})\right] : \boldsymbol{\varepsilon}_{UC}\, d\boldsymbol{p}. \tag{2.24}$$

In a linear elastic case, *Hooke's* law can be applied to obtain the local homogenised UC-stress from the local stiffness tensor ${}^4\boldsymbol{C}_{UC}$ and the strain.

$$\boldsymbol{\sigma}_{UC} = {}^4\boldsymbol{C}_{UC} : \boldsymbol{\varepsilon}_{UC}. \tag{2.25}$$

Since, in the nonlinear case, the load history influences the material response, the previously mentioned relations need to be adjusted to a time dependent variation of the stresses and strains. Here, as an example, the conversion to the time derivate is conducted for the local stress component, in analogy to Equations (2.24) and (2.25) [36]:

$$\dot{\boldsymbol{\sigma}}_C = \oint \psi(\boldsymbol{p}) \boldsymbol{R}^T(\boldsymbol{p}) \cdot \dot{\boldsymbol{\sigma}}_{UC}(\boldsymbol{p}) \cdot \boldsymbol{R}(\boldsymbol{p})\, d\boldsymbol{p} = \oint \psi(\boldsymbol{p}) \left[\boldsymbol{R}^T(\boldsymbol{p}) \overline{\otimes} \boldsymbol{R}^T(\boldsymbol{p})\right] : \dot{\boldsymbol{\sigma}}_{UC}\, d\boldsymbol{p}, \tag{2.26}$$

$$\dot{\boldsymbol{\sigma}}_{UC} = {}^4\boldsymbol{C}_{UC}^{tang} : \dot{\boldsymbol{\varepsilon}}_{UC}. \tag{2.27}$$

To find a relation between global strains or stresses to the local counterparts in the UC, assumptions must be made. Three different interaction assumptions are presented in the following chapters, namely the Voigt-, Reuss- and self-consistent assumption. [36, 39]

2.1.3.1 Voigt interaction assumption

The Voigt assumption states that every fibre in the composite experiences an equal global strain. The corresponding model can be described as springs representing the unit cells in parallel connection [39]. Hence, the local UC-strain can be written in dependency on the global composite strain as follows:

$$\boldsymbol{\varepsilon}_{UC} = \boldsymbol{R}(\boldsymbol{p}) \cdot \boldsymbol{\varepsilon}_C \cdot \boldsymbol{R}^T(\boldsymbol{p}) = \left[\boldsymbol{R}(\boldsymbol{p}) \overline{\otimes} \boldsymbol{R}(\boldsymbol{p})\right] : \boldsymbol{\varepsilon}_C. \tag{2.28}$$

Inserting that into Equation (2.25) and applying this to Equation (2.23) results in the following relation, after some restructuring:

$$\boldsymbol{\sigma}_C = \left\{\oint \psi(\boldsymbol{p})\left[\boldsymbol{R}^T(\boldsymbol{p}) \overline{\otimes} \boldsymbol{R}^T(\boldsymbol{p})\right] : {}^4\boldsymbol{C}_{UC} : \left[\boldsymbol{R}(\boldsymbol{p}) \overline{\otimes} \boldsymbol{R}(\boldsymbol{p})\right] d\boldsymbol{p}\right\} : \boldsymbol{\varepsilon}_C. \tag{2.29}$$

A comparison of the found relation with *Hooke's* law indicates that the term written in curly brackets equals the global composite stiffness. Therefore, the linear elastic homogenised composite stiffness ${}^4\boldsymbol{C}_C$ assuming Voigt interaction is found with the following relation:

$${}^4\boldsymbol{C}_C^V = \oint \psi(\boldsymbol{p})\left[\boldsymbol{R}^T(\boldsymbol{p}) \overline{\otimes} \boldsymbol{R}^T(\boldsymbol{p})\right] : {}^4\boldsymbol{C}_{UC} : \left[\boldsymbol{R}(\boldsymbol{p}) \overline{\otimes} \boldsymbol{R}(\boldsymbol{p})\right] d\boldsymbol{p}. \tag{2.30}$$

The method can be applied analogously for time derivates of the stress and strain tensors as well as the tangent stiffness tensor. [36, 39]

2.1.3.2 Reuss interaction assumption

In opposition to the Voigt assumption, the Reuss assumption applies a uniform stress state to each UC in the composite. It can be interpreted as UCs connected in series. Consequently, the dependency of the UC stress state on the global composite stress state is defined by the following relation:

$$\boldsymbol{\sigma}_{UC} = \boldsymbol{R}(\boldsymbol{p}) \cdot \boldsymbol{\sigma}_C \cdot \boldsymbol{R}^T(\boldsymbol{p}) = \left[\boldsymbol{R}(\boldsymbol{p}) \overline{\otimes} \boldsymbol{R}(\boldsymbol{p})\right] : \boldsymbol{\sigma}_C. \tag{2.31}$$

This can then be inserted into Equation (2.24) using the inverse *Hooke's* law, with the local UC-compliance tensor ${}^4\boldsymbol{S}_{UC} = {}^4\boldsymbol{C}_{UC}^{-1}$.

$$\boldsymbol{\varepsilon}_{UC} = {}^4\boldsymbol{S}_{UC}^R : \boldsymbol{\sigma}_{UC}, \tag{2.32}$$

$$\boldsymbol{\varepsilon}_C = \left\{\oint \psi(\boldsymbol{p})\left[\boldsymbol{R}^T(\boldsymbol{p}) \overline{\otimes} \boldsymbol{R}^T(\boldsymbol{p})\right] : {}^4\boldsymbol{C}_{UC}^{-1} : \left[\boldsymbol{R}(\boldsymbol{p}) \overline{\otimes} \boldsymbol{R}(\boldsymbol{p})\right] d\boldsymbol{p}\right\} : \boldsymbol{\sigma}_C. \tag{2.33}$$

Analogously to the previous chapter, by comparing the equation with the inverse *Hooke's* law, the homogenised composite compliance tensor can be identified as the term in curly brackets. Therefore, the resulting composite stiffness tensor can be found with the following expression:

$$ {}^{4}\boldsymbol{C}_{C}^{R} = \left\{ \oint \psi(\boldsymbol{p}) \left[\boldsymbol{R}^{T}(\boldsymbol{p}) \,\overline{\otimes}\, \boldsymbol{R}^{T}(\boldsymbol{p}) \right] : \left[{}^{4}\boldsymbol{C}_{UC} \right]^{-1} : \left[\boldsymbol{R}(\boldsymbol{p}) \,\overline{\otimes}\, \boldsymbol{R}(\boldsymbol{p}) \right] d\boldsymbol{p} \right\}^{-1}. \tag{2.34} $$

In analogy to the resulting composite stiffness considering the *Voigt* assumption, the time derivate version can be found accordingly by replacing the stiffness tensors with the corresponding tangent stiffness tensors and the time derivates of the stress and strain tensors. [36, 39]

2.1.3.3 Self-consistent interaction assumption

The Voigt and the Reuss assumption represent the extreme assumptions to be made for the fibre interaction. Their resulting stiffnesses represent the upper or lower limit of the estimated material response, respectively. An intermediate approach is represented by the self-consistent (SC) interaction assumption. Here, the fibre is interpreted as an inclusion inside a homogenous medium with properties of the actual composite. The strain in the Unit Cell can then be represented by the equivalent strain in the composite using a stress concentration tensor ${}^{4}\boldsymbol{A}$.

$$ \boldsymbol{\varepsilon}_{UC} = {}^{4}\boldsymbol{A} : \boldsymbol{\varepsilon}_{\mathrm{C}}, \tag{2.35} $$

$$ {}^{4}\boldsymbol{A} = \left[{}^{4}\boldsymbol{I} + {}^{4}\boldsymbol{E} : \left(\left[{}^{4}\boldsymbol{C}_{C} \right]^{-1} : {}^{4}\boldsymbol{C}_{UC}^{glob} - {}^{4}\boldsymbol{I} \right) \right]^{-1}, \tag{2.36} $$

$$ \begin{aligned} {}^{4}\boldsymbol{C}_{UC}^{glob} &= \boldsymbol{R}^{T}(\boldsymbol{p}) \cdot \boldsymbol{R}^{T}(\boldsymbol{p}) \cdot {}^{4}\boldsymbol{C}_{UC} \cdot \boldsymbol{R}(\boldsymbol{p}) \cdot \boldsymbol{R}(\boldsymbol{p}) \\ &= \left[\boldsymbol{R}^{T}(\boldsymbol{p}) \,\overline{\otimes}\, \boldsymbol{R}^{T}(\boldsymbol{p}) \right] : {}^{4}\boldsymbol{C}_{UC} : \left[\boldsymbol{R}(\boldsymbol{p}) \,\overline{\otimes}\, \boldsymbol{R}(\boldsymbol{p}) \right], \end{aligned} \tag{2.37} $$

with ${}^{4}\boldsymbol{I}$ representing the fourth order identity tensor in respect to a double contraction product (see Appendix 0). ${}^{4}\boldsymbol{E}$ is the fourth order *Eshelby* tensor for anisotropic media which is dependent on the composite stiffness tensor [19]. Inserting Equation (2.35) into the *Hooke's* law for obtaining the composite stress and proceeding as described in the previous two examples results in a description for the composite stiffness.

$$ {}^{4}\boldsymbol{C}_{C}^{SC} = \oint \psi(\boldsymbol{p}) \; {}^{4}\boldsymbol{C}_{UC}^{glob} : \left[{}^{4}\boldsymbol{I} + {}^{4}\boldsymbol{E} : \left(\left[{}^{4}\boldsymbol{C}_{C}^{SC} \right]^{-1} : {}^{4}\boldsymbol{C}_{UC}^{glob} - {}^{4}\boldsymbol{I} \right) \right]^{-1} d\boldsymbol{p}. \tag{2.38} $$

Due to the fact that the resulting composite stiffness ${}^{4}\boldsymbol{C}_{C}^{SC}$ stands on both sides of the equation, an analytical solution for this problem is not feasible. Therefore, a fixed point iteration is used to calculate the composite stiffness with underlying self-consistent assumption. [36, 39]

2.1.4 Global strain increment in the elasto-plastic domain

For the elasto-plastic model, the material response is obtained over several consecutive load increments. This is necessary since, the elasto-plastic material response is dependent on the previous load history. Hence, for the OA-model predictions, a predefined load case must be applied to the material. In this case, a strain controlled uniaxial stress state is considered as load case for the composite, which makes the predictions comparable to general tensile tests on SFRC specimens.

Mirkhalaf et al. present a framework with which the aforementioned load cases can be approximated and the incremental material response estimated [36]. Writing the composite stress $\boldsymbol{\sigma}_C$ and strain $\boldsymbol{\varepsilon}_C$ tensors in *Voigt* notation:

$$\underline{\boldsymbol{\sigma}}_C = (\sigma_{C,11} \quad \sigma_{C,22} \quad \sigma_{C,33} \quad \sigma_{C,23} \quad \sigma_{C,13} \quad \sigma_{C,12})^T, \tag{2.39}$$

$$\underline{\boldsymbol{\varepsilon}}_C = (\varepsilon_{C,11} \quad \varepsilon_{C,22} \quad \varepsilon_{C,33} \quad 2\,\varepsilon_{C,23} \quad 2\,\varepsilon_{C,13} \quad 2\,\varepsilon_{C,12})^T. \tag{2.40}$$

The vectors can each be divided into a known and unknown part. For the strain tensor, only the strain in load direction is given, while the remaining are unknown. The stress tensor, however, is mostly determined, since every other component apart from the load direction is equal to zero. Consequently, by rearranging the vectors, they can each be written as a scalar value marked with the index I and a five-dimensional vector marked with the index II:

$$\underline{\boldsymbol{\sigma}}_C = \begin{bmatrix} \underline{\sigma}_{C,I} \\ \underline{\boldsymbol{\sigma}}_{C,II} \end{bmatrix}, \qquad \underline{\boldsymbol{\varepsilon}}_C = \begin{bmatrix} \underline{\varepsilon}_{C,I} \\ \underline{\boldsymbol{\varepsilon}}_{C,II} \end{bmatrix}. \tag{2.41}$$

Where each constituent can be referred to as:

- $\underline{\varepsilon}_{C,I}$: imposed strain component (known)
- $\underline{\boldsymbol{\varepsilon}}_{C,II}$: unconstrained strain components (unknown)
- $\underline{\sigma}_{C,I}$: uniaxial stress component (unknown)
- $\underline{\boldsymbol{\sigma}}_{C,II}$: zero-stress components (known)

Hooke's law could then be written, using the tangent stiffness tensor in *Voigt* notation $\underline{\boldsymbol{C}}_C^{tang}$ and a small stress and strain increment ($\Delta\underline{\boldsymbol{\sigma}}_C$ and $\Delta\underline{\boldsymbol{\varepsilon}}_C$), as follows:

$$\begin{bmatrix} \Delta\underline{\sigma}_{C,I} \\ \Delta\underline{\boldsymbol{\sigma}}_{C,II} \end{bmatrix} \approx \begin{bmatrix} \underline{C}_{C,(I,I)}^{tang} & \underline{\boldsymbol{C}}_{C,(I,II)}^{tang} \\ \underline{\boldsymbol{C}}_{C,(II,I)}^{tang} & \underline{\boldsymbol{C}}_{C,(II,II)}^{tang} \end{bmatrix} \cdot \begin{bmatrix} \Delta\underline{\varepsilon}_{C,I} \\ \Delta\underline{\boldsymbol{\varepsilon}}_{C,II} \end{bmatrix}. \tag{2.42}$$

Note that the tangent stiffness itself is dependent on the current stress state. Hence, in order to obtain a valid approximation of the composite response, the applied strain increment should be small. Solving the linear equation for the zero-stress components gives the following:

$$\mathbf{0} = \Delta\underline{\boldsymbol{\sigma}}_{C,II} \approx \underline{\boldsymbol{C}}_{C,(II,I)}^{tang} \cdot \Delta\underline{\varepsilon}_{C,I} + \underline{\boldsymbol{C}}_{C,(II,II)}^{tang} \cdot \Delta\underline{\boldsymbol{\varepsilon}}_{C,II}. \tag{2.43}$$

Restructuring of Equation (2.43) results the solution for the unconstrained strain components.

$$\Delta\underline{\boldsymbol{\varepsilon}}_{C,II} \approx -\left[\underline{\boldsymbol{C}}_{C,(II,II)}^{tang}\right]^{-1} \cdot \underline{\boldsymbol{C}}_{C,(II,I)}^{tang} \cdot \Delta\underline{\varepsilon}_{C,I}. \tag{2.44}$$

Finally, the uniaxial stress increment can be obtained by the following equation:

$$\Delta\underline{\sigma}_{C,I} \approx \underline{C}_{C,(I,I)}^{tang} \cdot \Delta\underline{\varepsilon}_{C,I} + \underline{\boldsymbol{C}}_{C,(I,II)}^{tang} \cdot \Delta\underline{\boldsymbol{\varepsilon}}_{C,II}. \tag{2.45}$$

With this, the mechanical state of the composite is fully described.

The described method is used in the current simulations to estimate the following strain and stress increment, by using the composite tangent stiffness from the previous time step. After that, the local UC-strain increments are then calculated for each fibre orientation using the described interaction properties from Chapter 2.1.3. The strain increment is then fed into the surrogate model for the UC-behaviour to obtain the corresponding UC-stress response and the local tangent stiffness. From this, the global composite material response is averaged using Equations (2.23) and (2.24). The global tangent stiffness tensor is then obtained from the local tangent stiffnesses using the aforementioned Orientation Averaging schemes. [36]

With the presented methods, a full toolbox for obtaining the material response of an SFRC for the linear elastic and the elasto plasic domain is given. However, the material model can only represent materials with a single fibre length. In the following chapter, fibre length distributions in SFRCs are studied and the model is extended to allow it to additionally consider fibre length distributions.

2.2 Fibre-matrix interface debonding

For increasing strain levels, composite materials show some softening behaviour which is usually not captured by elasto plastic material models. One possible explanation is the negligence of any damage phenomena in the material model. For those high strains it is expected that some case of material damage will occur in the composite material.

The three main failure mechanisms in fibre reinforced composites are fibre breakage and fibre-matrix interface debonding and martix cracking. The probability of fibre breakage is very low for fibres shorter than a critical fibre length l_{crit} defined by *Bowyer* and *Bader* [8].

$$l_{crit} = \frac{E_F \cdot \varepsilon_{ult} \cdot d_F}{2 \cdot \tau_{II}^{max}}, \tag{2.46}$$

with ε_{ult} being the ultimate fibre strain and τ_{II}^{max}, the interfacial shear strength between the fibre and the matrix. Usually, the fibre lengths in SFRC are much shorter than that critical fibre length. Hence, the predominant failure mechanism within these materials is fibre-matrix debonding. [46]

The loads in the matrix are transferred into the fibre mostly through shear stresses along the fibre cylinder walls. Figure 2.12 depicts the stress curves for the shear stresses in the interface and the resulting normal stresses whithin the fibre. This is shown for three different debonding stages under uniaxial loading conditions along the fibre axis. Stage 1) depicts a fully bonded state, where the interface is still fully intact. In stage 2) the inteface debonding is already initiated and stage 3) shows a fully debonded fibre. From the shear stress curve in stage 1), it is seen that the highest stresses are found at the fibre tips. Once the shear loads on the tips reach the interface strength τ_{II}^{max}, the debonding is initiated. With increasing displacement, the crack propagates along the fibre axis to the middle of the fibre until the interface is fully debonded. In the figure, the debonded parts of the fibre are still underlying interfacial shear stress [11].

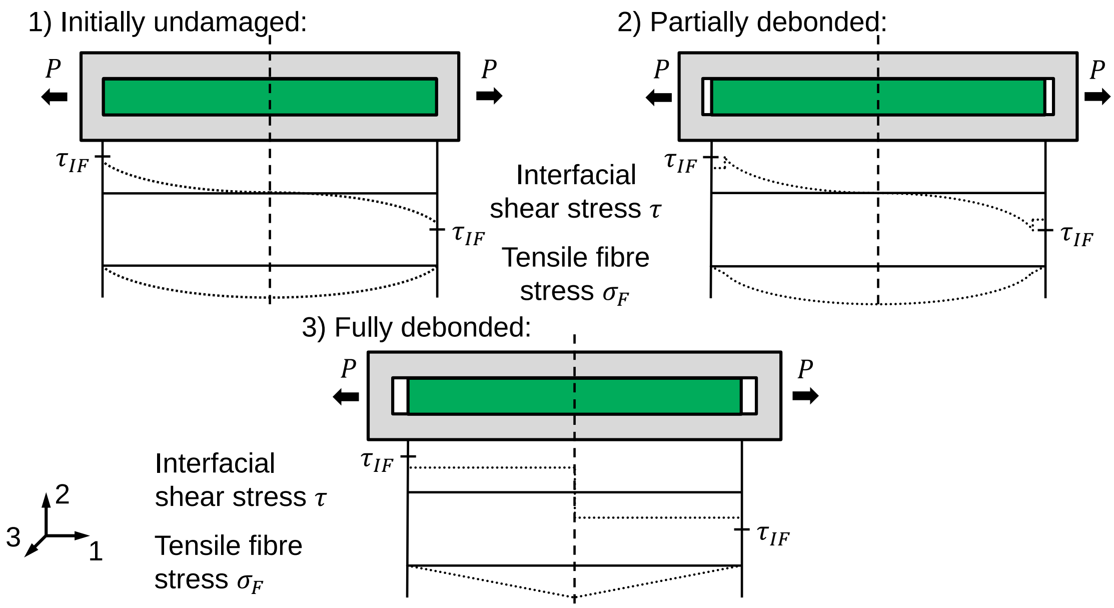

Figure 2.12: Fibre-matrix interface crack propagation and corresponding interface and fibre stresses [11].

This is due to friction between the fibre and the matrix. With less fibre length interacting with the matrix, the material softens. Additionally, the unidirectional homogenised composite stiffness decreases [46].

The debonding behaviour is mainly influenced by the composite constituents' materials and the sizing, which is applied on the fibre. Additionally, the manufacturing process is also influencing the quality of the bond as well as the fibre volume fraction, which makes a generalised definition of the interface properties very challenging [54]. Also, there is no well-established test for obtaining these properties. These uncertainties are the reason for difficulties while finding reliable information on the interface properties on a certain material combination in the literature.

Modelling the debonding processes in numerical simulations is feasible through the application of cohesive zone modelling in the fibre-matrix interface. In the simulation software ABAQUS, there are two basic modelling techniques which can be used for this purpose. First, thin cohesive elements can be placed between the fibre and the matrix. These elements represent the interface layer and enable the user to model thickness variations of the interface. In comparison to that, the second method uses surface interaction properties between the two instances. In this case, the interface is modelled with constant or even zero thickness. In this work the surface interaction method is used. It is, therefore, determined, that a crack propagates solely along the fibre cylinder wall.

The interface fails due to three different loading conditions which describe the different failure modes. Mode I is defined by failure due to tensile stresses normal to the interface surfaces. The other two failure modes (II and III) are due to shear stresses in two perpendicular directions. Combinations of failure modes due to mixed loading conditions can be considered with coupled failure criterions [22]. In the example of fibre parallel loading, the predominant failure mechanism is due to shear loads in the interface. Hence, the interface failure mode II will be investigated further in this chapter.

The behaviour of the interface is defined by the traction-separation-law. A traction τ_{II} is introduced in the interface by a separation δ_{II} of the two opposing surfaces. The interface is expected to behave linear elastically in the initial bonded state, with a defined interface stiffness K_{II}. The traction of the interface is then given by this relation:

$$\tau_{II} = K_{II} \cdot \delta_{II}. \tag{2.47}$$

It should be mentioned that in the zero thickness interaction property of surface interaction model, the interface stiffness K couples stress and displacement. Hence, the unit of this parameter is N/mm³. The interface behaves linear elastic until a certain interfacial shear strength τ_{II}^{max}. From this point. when further seperation is introduced, the interface shows softening behaviour until the interface stress approaches 0 N/mm² and the interface is fully debonded. The softening behaviour can be modelled in several different ways. However, a linear softening is used in the most cases due to its simplicity and low numerical effort [22]. An example for a traction-separation behaviour with linear softening is depicted in Figure 2.13.

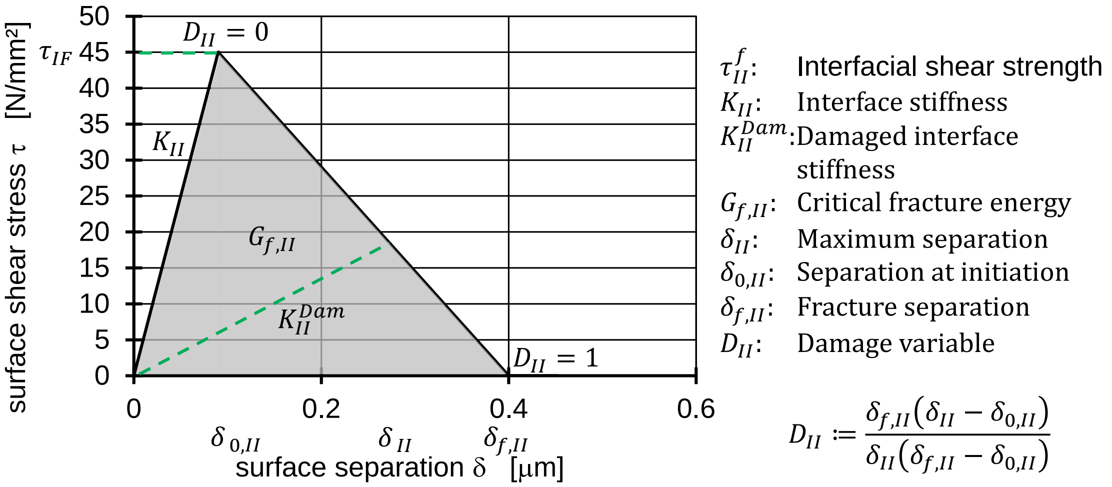

Figure 2.13: Linear traction separation law with linear softening [22].

The softening behaviour is fully defined by the interfacial shear strength τ_{II}^{max} and the absorbed energy $G_{f,II}$ until full separation of the bond. With these parameters, the separation at fracture is defined.

$$\delta_{f,II} = \frac{2G_{f,II}}{\tau_{II}^{max}}. \tag{2.48}$$

Note that the fracture separation is independent from the interface stiffness K_{II}. With this value, the shape of the triangular traction separation behaviour can be defined. Lower stiffnesses lead to a higher separation in the linear elastic domain, but a more brittle softening behaviour. Since this value does not affect the critical fracture energy and, therefore, the final failure point, it can be adjusted to improve the stability of the simulation.

In order to define the damage initiation point for a mixed mode behaviour a criterion needs to be defined. One frequently used method is the quadratic initiation of methods, similar to the von Mises yield criterion [22].

$$1 = \sqrt{\left(\frac{\langle\sigma_I\rangle}{\sigma_I^{max}}\right)^2 + \left(\frac{\tau_{II}}{\tau_{II}^{max}}\right)^2 + \left(\frac{\tau_{III}}{\tau_{III}^{max}}\right)^2}, \tag{2.49}$$

with $\langle * \rangle$ representing the *McCauley* brackets operator. The fracture energy must also be expressed for mixed mode behaviour. A commonly used method is the Power Law, which is given by the following:

$$1 = \left(\frac{G_I}{G_{I,C}}\right)^\alpha + \left(\frac{G_{II}}{G_{II,C}}\right)^\alpha + \left(\frac{G_{III}}{G_{III,C}}\right)^\alpha, \tag{2.50}$$

with α being a material parameter, ranging between 1 and 2. Its value must be derived from expreimental results with mixed mode behaviour.

It is worth mentioning that the presented model is simple. Nevertheless, a wide range of parameters are necessary to fully define the interface fracture behaviour of a fibre-matrix interface. Information on the interface behaviour of different fibre-matrix combination is found in the rarest of cases and when modelling the delamination it is often referred to standard values.

3 Fibre length distributions in SFRCs

For SFRCs with a thermoplastic matrix, the injection moulding process is the standard processing method. During this process, the plastic is molten, mixed, and injected. All of these steps induce large shear stresses into the polymer melt as well as the incorporated fibres [20]. This leads to fibre breakages during the processing, caused by interaction with other filler materials or the tool walls, or fibre kinking. As a result, the fibre length in the injection moulded part is not uniform [21].

The following chapters explain the influence of fibre length on the Unit Cell material properties, the way fibre length distributions can be characterised and how these distributions can be modelled using the two-step Orientation Averaging method.

3.1 Fibre length dependent Unit Cell stiffness

The fibre length, among other important parameters (matrix material behaviour, fibre material behaviour, fibre volume fraction), influences the resulting homogenised material response of a Unit Cell significantly. To show this, numerical Unit Cell simulations with different fibre lengths are conducted.

Figure 3.1 presents the resulting homogenised stiffnesses parallel and perpendicular to the fibre direction for Unit Cells with varying fibre lengths that experience linear elastic material behaviour. The material parameters used for this model are based on standard values for a glass

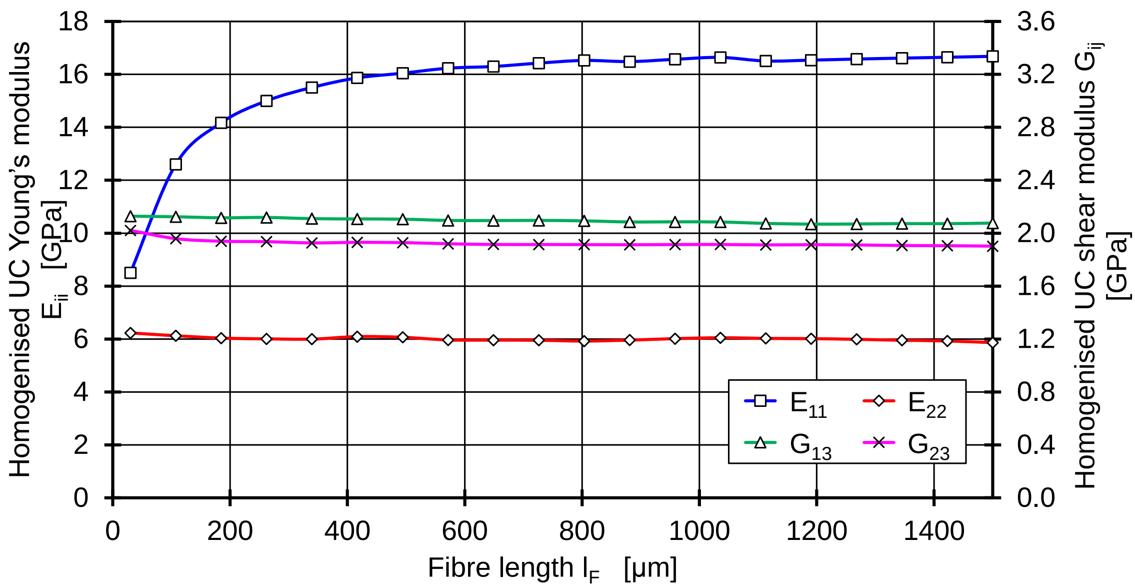

Figure 3.1: Influence of the fibre length on the homogenised, linear elastic properties of a single fibre Unit Cell.

fibre reinforced polymer composite, listed in Table 3.1. In the Figure, it can be seen that there is a nonlinear dependence of the Young's Modulus E_{11} on the fibre length. The dependence is particularly considerable for short fibre lengths up to around 600 µm. The other homogenised stiffness components do not show such a significant dependency on the fibre length.

Table 3.1: Material properties for fibre length dependent UC-simulations.

Property	**Symbol**	**Value**	**Unit**
Matrix Young's modulus	E_M	4,000	N/mm²
Matrix Poisson's ratio	ν_M	0.35	-
Fibre Young's modulus	E_F	76,000	N/mm²
Fibre Poisson's ratio	ν_F	0.22	-
Fibre volume fraction	φ	0.2	-
Fibre diameter	d_f	15	µm

Several micro-mechanical models have been developed to predict the composite stiffness of a unidirectional SFRC with given parameters. They are based on different assumptions for the fibre embedding in the matrix, or they are derived from empirical observations. Three examples for analytical models are given. The *Cox* Shear-Lag model assumes a load transfer from the matrix to the fibre exclusively through shear stresses along the fibre cylinder surface [17]. A second model, developed by *Mori* and *Tanaka*, is based on an *Eshelby* inclusion model, considering interactions between several inclusions [41]. The third model, namely the *Halpin-Tsai* model, represents an empirical approach based on a self-consistent analytical solution, which is simplified to directly calculate engineering constants for a unidirectional SFRC composite [23]. Figure 3.2 shows predictions for the fibre parallel Young's modulus obtained from the three models in comparison to the UC simulations using the same parameters from Table 3.1. All models follow the same qualitative trends. Greater differences in the predictions

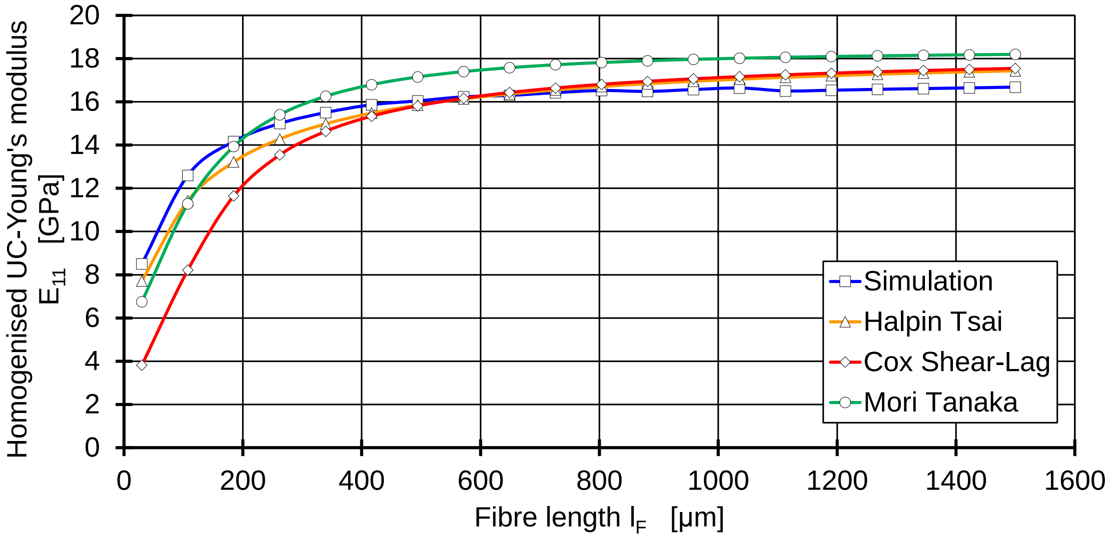

Figure 3.2: Comparison of UC-simulations and analytical models on the resulting homogenised fibre parallel composite stiffness.

occur especially for decreasing fibre lengths. In comparison to the UC-simulations the *Halpin-Tsai* model seems to give the best approximation of the fibre parallel Young's modulus over the full range of fibre lengths.

3.2 Typical fibre length distributions in SFRC

Analysis methods like micro-CT allow for a relatively quick and non-destructive way of measuring distributions in fibre orientation, length and diameter inside a composite [27, 32]. These methods give a deeper insight on how the distributions evolved in the composite. However, Fibre Length Distributions (FLD) can also be analysed under the microscope after separating the fibres from the matrix, for example by burning off the polymer material in a furnace [16].

The resulting fibre length distributions from the analyses generally have an asymmetrical shape with quickly increasing probabilities for shorter fibres and a tail-like slowly decreasing probability for higher fibre lengths [16]. With the composite entering the manufacturing process with an approximately normal FLD and, considering that longer fibres have a higher probability of breaking into smaller pieces, this type of distribution can be explained. After the processing, the mean fibre length can be reduced by up to a tenth of the original fibre length [16]. Furthermore, the concentration of fibres in a composite is found to have a great influence on its FLD. Since higher amounts of fibres in the matrix lead to a higher probability of fibre interaction and consequently breakage, the resulting mean fibre length inside the composite is likely to be smaller for a composite with a high volume fraction of fibres, compared to a composite with a lower fibre volume fraction [27, 33].

The probability density function of these distributions is captured by several analytical functions. *Li, Hwang et al.* mention *Weibull* distributions, logarithmic distributions and Generalised Extreme Value (GEV) distributions as suitable Probability Density Functions (PDF) for representing the fibre length distribution in an injection moulded composite [33]. The authors claim the logarithmic and the GEV-distribution to result in the better fit on the measured FLD. However, in other literature, the *Weibull* distribution function is more commonly used to describe the FLD of an SFRC [34, 44, 45]. Therefore, it is described in more detail.

The *Weibull* PDF $f(l_F)$ can be written as follows:

$$f(l_F) = \frac{s_2}{s_1} \cdot \left(\frac{l_F}{s_1}\right)^{s_2-1} \cdot e^{-\left(\frac{l_F}{s_1}\right)^{s_2}}, \tag{3.1}$$

with the shape parameters s_1 and s_2 adjusted to the measured FLD by solving the following equations:

$$0 = \frac{\sum_{i=1}^{N_F}\left(l_{F,i}\right)^{s_2}\ln\left(l_{F,i}\right)}{\sum_{l_{F,i}}^{N_F}\left(l_{F,i}\right)^{s_2}} - \frac{1}{N}\sum_{i=1}^{N_F}\ln\left(l_{F,i}\right) - \frac{1}{s_2}, \tag{3.2}$$

$$s_1 = \left[\left(\sum_{i=1}^{N_F}\left(l_{F,i}\right)^{s_2}\right) \cdot \frac{1}{N_F}\right]^{1/s_2}, \tag{3.3}$$

where N_F represents the number of fibres measured in the analysis of the FLD. An analytical solution to Equation (3.2) is not easy to find. Therefore, the iterative *Newton-Raphson* method is recommended for finding an approximate solution [45].

From the FLD-function, an averaged value can be obtained by integration over the range of fibre lengths. The resulting averaged fibre length can be obtained from the following equation:

$$l_F^{num} = \frac{\int_0^\infty f(l_F) \cdot l_F \, dl_F}{\int_0^\infty f(l_F) \, dl_F} = \int_0^\infty f(l_F) \cdot l_F \, dl_F. \tag{3.4}$$

In addition to the FLD-function, defined by the number-frequency of a certain fibre length, a volume-weighted FLD can be derived from the number-weighted FLD $f(l_F)$. Assuming a constant fibre diameter, the volume-weighted FLD the volume is solely dependent in the fibre length l_F. Hence, a volume-weighted FLD $w(l_F)$ and the corresponding volume-averaged fibre length l_F^{vol} can be obtained from the following relations, respectively:

$$w(l_F) = \frac{f(l_F) \cdot l_F}{\int_0^\infty f(l_F) \cdot l_F \, dl_F}, \tag{3.5}$$

$$l_F^{vol} = \frac{\int_0^\infty f(l_F) \cdot l_F^2 \, dl_F}{\int_0^\infty f(l_F) \cdot l_F \, dl_F} = \int_0^\infty w(l_F) \cdot l_F \, dl_F. \tag{3.6}$$

Figure 3.3 shows a *Weibull* distribution, created with the described method, compared to a measured fibre length distribution, which is then ranked into fibre length classes with an interval of each 100 µm. The set of measured fibre lengths are provided by *Holmström, Hopperstad et al.* [26, 27]. For this case, the FLD of the 30 %wt. glass fibre reinforced Polyamide is taken.

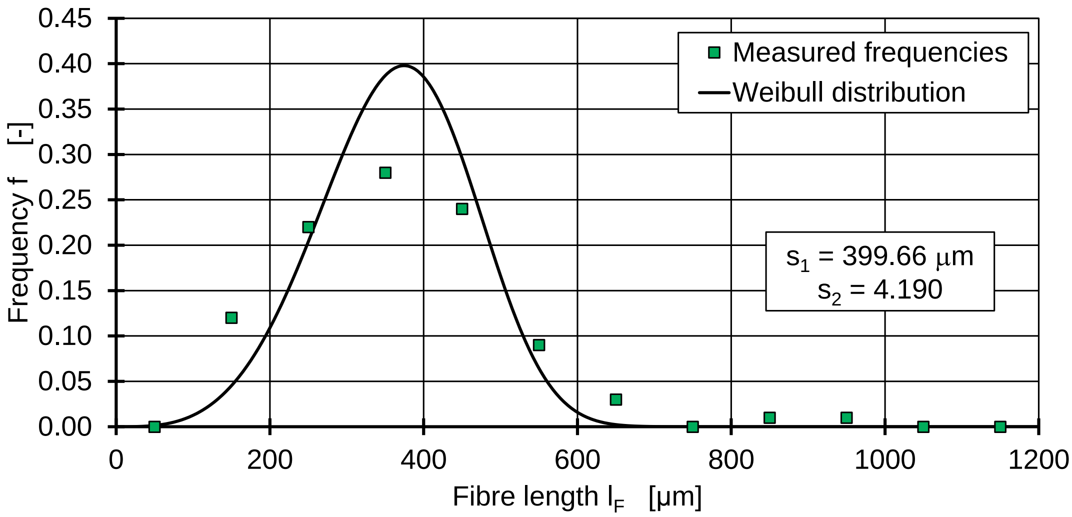

Figure 3.3: Comparison of a measured fibre length distribution and its corresponding Weibull-distribution function.

The resulting shape parameters for the distribution function are given with $s_1 = 399.66$ µm and $s_2 = 4.190$. To scale the *Weibull* PDF to the frequency values of the measured FLD, the PDF is multiplied by the value of the fibre length interval used for the classification of the measured fibre lengths. As it can be seen, the *Weibull* distribution function represents the FLD qualitatively well. However, there some differences as for example the shape of *Weibull* PDF is narrower than the measured frequencies in the graph would suggest. This is related to the size of the fibre length intervals being relatively big. Reducing the interval to a lower value would result in a better approximation of the *Weibull* distribution calculated from the actual measured fibre lengths.

In some cases, however, the measured FLD can not be properly described by an analytical PDF. As for example, in *Breuer* and *Stommel*, the measured FLD of the used meterial, visualised in Figure 3.4, shows a large peak for very low fibre lengths [9]. This can not be captured by an

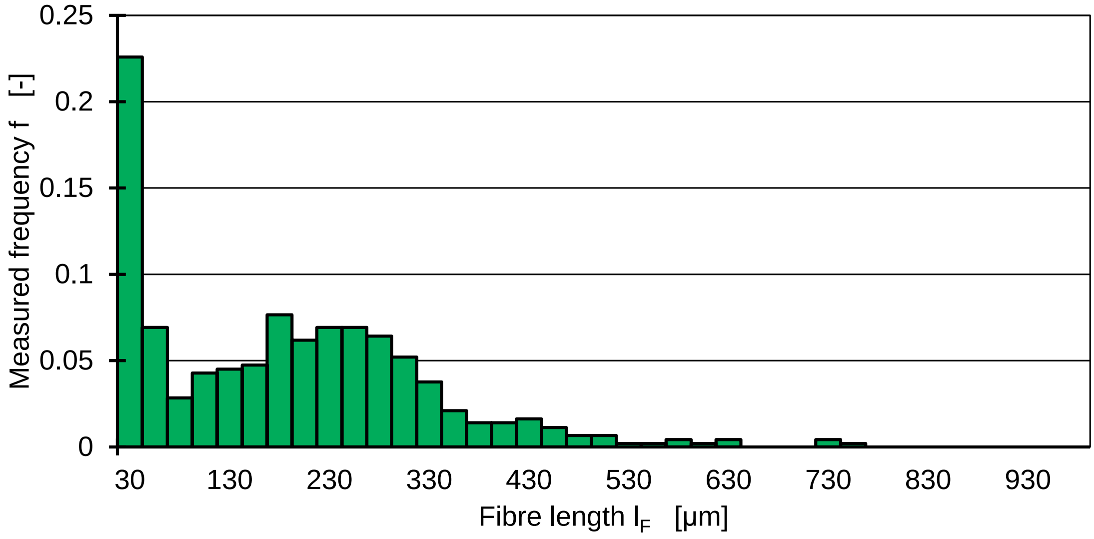

Figure 3.4: Fibre length distribution of a glass fibre reinforces Polybutylene terephthalate with a peak at low fibre lengths [9].

analytical PDF. Additionally, in most literature, the measured FLD is already classified to a certain range of lengths. Hence, deriving an analytical fibre length distribution directly from the measurements is not possible. Therefore, in the following, FLDs are represented by frequencies of fibre length classes of a certain range.

It seems reasonable to the author that the shear flow created during the injection moulding process has a higher effect on the orientation of longer fibres. As a consequence, a fibre length dependent orientation distribution would develop during the manufacturing. This theory is confirmed in *Mortazavian* and *Fatemi* [42]. These autors present different orientation distributions for three consecutive ranges of fibre lengths for a glass fibre reinforced Polyamide 6 composite. From that, it can be seen that greater fibre lengths show an orientation distribution with a higher concentration of fibre orientations towards the injection flow direction [42]. This effect, however, is not represented in most other literature. In those cases an independent FOD has to be assumed.

3.3 Representing fibre length distributions in the Orientation Averaging process

With the fibre length distributions in SFRC described, consequently, this feature needs to be embedded into the Orientation Averaging process. Three different methodologies are identified from a literature research [9, 20, 25, 33, 45]:

- Using UD-RVEs with integrated fibre length distribution for the first step
- Adding a second averaging scheme over the fibre lengths using UC-simulations
- Obtaining a single representative fibre length based on the fibre length distribution.

The aforementioned approaches are presented, analysed, and evaluated in the following chapters.

3.3.1 Unidirectional RVEs with integrated fibre length distributions

The first method uses volumetric homogenisation of a unidirectional Representative Volume Element. The fibres in this volume element have different lengths, representing the fibre length distribution of the composite. The resulting homogenised material response represents the whole fibre length distribution. Consequently, the Orientation Averaging step can be performed as described in Chapter 2.1.3, using the homogenised material response of the simulation. The material response of UD-RVEs including FLDs is used by several authors to describe the impact of fibre length distributions on the composite stiffness, see e.g. [9, 25].

With the described method, the Orientation Averaging process does not have to be adapted to cover the fibre length distributions and consequently would not change the performance of the method itself. However, due to the randomised geometry generation of the RVEs, the homogenised responses scatter. The additional randomised variable (l_F) introduced by the fibre length distributions increases the effect even more [9]. To overcome this, a multiple RVE-geometries would have to be created and simulated to find a statistically representative material response [9, 25]. Another disadvantage of this method would be the disability to represent locally changing fibre length distributions in a coupled multiscale simulation. In that case for each FLD, new simulations would have to be conducted.

3.3.2 Fibre length averaging

As an alternative to the previously described method, the different fibre length distributions can be integrated into the Orientation Averaging process. This is realised by another averaging scheme over the fibre length distribution [45, 51]. With UC-simulations considering the investigated fibre length classes, a fibre length dependent material response is obtained. The global composite response is then described by the local stresses and strains in the UC as follows:

$$\boldsymbol{\sigma}_C = \int_0^\infty w(l_F) \cdot \oint \psi(\boldsymbol{p}, l_F) \left[\boldsymbol{R}^T(\boldsymbol{p}) \overline{\otimes} \boldsymbol{R}^T(\boldsymbol{p})\right] : \boldsymbol{\sigma}_{UC}(l_F)\, d\boldsymbol{p}\ dl_F, \tag{3.7}$$

$$\boldsymbol{\varepsilon}_C = \int_0^\infty w(l_F) \cdot \oint \psi(\boldsymbol{p}, l_F) \left[\boldsymbol{R}^T(\boldsymbol{p}) \overline{\otimes} \boldsymbol{R}^T(\boldsymbol{p})\right] : \boldsymbol{\varepsilon}_{UC}(l_F)\, d\boldsymbol{p}\ dl_F, \tag{3.8}$$

with $w(l_F)$ representing the volume-weighted fibre length distribution function, presented in Equation (3.5). As a larger fibre represents a larger volume in the heterogeneous composite, its material response has a higher impact on the homogenised response compared to a lower volume fibre.

The resulting homogenised composite stiffnesses can then be derived by applying the mentioned interaction assumptions described in Chapter 2.1.3. This results in the following relations for the Voigt, Reuss and self-consistent assumptions, respectively:

$$\begin{aligned} {}^4\boldsymbol{C}_C^V = \int_0^\infty w(l_F) \oint \psi(\boldsymbol{p}, l_F) \left[\boldsymbol{R}^T(\boldsymbol{p}) \overline{\otimes} \boldsymbol{R}^T(\boldsymbol{p})\right] : {}^4\boldsymbol{C}_{UC}(l_F) \\ : \left[\boldsymbol{R}(\boldsymbol{p}) \overline{\otimes} \boldsymbol{R}(\boldsymbol{p})\right] d\boldsymbol{p}\ dl_F, \end{aligned} \tag{3.9}$$

$$\begin{aligned} {}^4\boldsymbol{C}_C^R = \left\{\int_0^\infty w(l_F) \oint \psi(\boldsymbol{p}, l_F) \left[\boldsymbol{R}^T(\boldsymbol{p}) \overline{\otimes} \boldsymbol{R}^T(\boldsymbol{p})\right] : \left[{}^4\boldsymbol{C}_{UC}(l_F)\right]^{-1} \right. \\ \left. : \left[\boldsymbol{R}(\boldsymbol{p}) \overline{\otimes} \boldsymbol{R}(\boldsymbol{p})\right] d\boldsymbol{p}\, dl_F \right\}^{-1}, \end{aligned} \tag{3.10}$$

$$\begin{aligned} {}^4\boldsymbol{C}_C^{SC} = \int_0^\infty w(l_F) \oint \psi(\boldsymbol{p}, l_F)\ {}^4\boldsymbol{C}_{UC}^{glob}(\boldsymbol{p}, l_F) \\ : \left[{}^4\boldsymbol{I} + {}^4\boldsymbol{E} : \left(\left[{}^4\boldsymbol{C}_C^{SC}\right]^{-1} : {}^4\boldsymbol{C}_{UC}^{glob}(\boldsymbol{p}, l_F) - {}^4\boldsymbol{I}\right)\right]^{-1} d\boldsymbol{p}\ dl_F. \end{aligned} \tag{3.11}$$

with ${}^4\boldsymbol{C}_{UC}^{glob}(\boldsymbol{p}, l_F)$, in Equation (3.11), representing the fibre length dependent UC-stiffness transformed into the global composite coordinate system.

$${}^4\boldsymbol{C}_{UC}^{glob}(\boldsymbol{p}, l_F) = \left[\boldsymbol{R}^T(\boldsymbol{p}) \overline{\otimes} \boldsymbol{R}^T(\boldsymbol{p})\right] : {}^4\boldsymbol{C}_{UC}(l_F) : \left[\boldsymbol{R}(\boldsymbol{p}) \overline{\otimes} \boldsymbol{R}(\boldsymbol{p})\right]. \tag{3.12}$$

Note that the fibre orientation distribution function $\psi(\boldsymbol{p}, l_F)$ is marked as dependent on the fibre length. However, as described earlier, in most cases, a fibre length independent FOD can be assumed. Considering this, Equations (3.9) and (3.10) can be rearranged to isolate the integral over the fibre lengths from the independent constituents.

$$\begin{aligned} {}^4\boldsymbol{C}_C^V = \oint \psi(\boldsymbol{p}) \left[\boldsymbol{R}^T(\boldsymbol{p}) \overline{\otimes} \boldsymbol{R}^T(\boldsymbol{p})\right] : \left\{\int_0^\infty w(l_F)\ {}^4\boldsymbol{C}_{UC}(l_F) dl_F\right\} \\ : \left[\boldsymbol{R}(\boldsymbol{p}) \overline{\otimes} \boldsymbol{R}(\boldsymbol{p})\right] d\boldsymbol{p}, \end{aligned} \tag{3.13}$$

$$\begin{aligned} {}^4\boldsymbol{C}_C^R = \left\{\oint \psi(\boldsymbol{p}) \left[\boldsymbol{R}^T(\boldsymbol{p}) \overline{\otimes} \boldsymbol{R}^T(\boldsymbol{p})\right] : \left\{\int_0^\infty w(l_F) \left[{}^4\boldsymbol{C}_{UC}(l_F)\right]^{-1} dl_F\right\} \right. \\ \left. : \left[\boldsymbol{R}(\boldsymbol{p}) \overline{\otimes} \boldsymbol{R}(\boldsymbol{p})\right] d\boldsymbol{p}\right\}^{-1} d\boldsymbol{p}\, dl_F. \end{aligned} \tag{3.14}$$

It is not clear if an analogue rearrangement can be conducted for Equation (3.11). However, tests have shown that the following rearrangement leads to equivalent results for the presented relations:

$$ {}^4\boldsymbol{C}_C^{SC} = \oint \psi(\boldsymbol{p}) \; {}^4\boldsymbol{C}_{FLD}^{glob}(\boldsymbol{p}) : \left[{}^4\boldsymbol{I} + {}^4\boldsymbol{E} : \left(\left[{}^4\boldsymbol{C}_C^{SC} \right]^{-1} : \; {}^4\boldsymbol{C}_{FLD}^{glob}(\boldsymbol{p}) - {}^4\boldsymbol{I} \right) \right]^{-1} d\boldsymbol{p}, \tag{3.15} $$

$$ {}^4\boldsymbol{C}_{FLD}^{glob}(\boldsymbol{p}) = \left[\boldsymbol{R}^T(\boldsymbol{p}) \,\overline{\otimes}\, \boldsymbol{R}^T(\boldsymbol{p}) \right] : \; {}^4\boldsymbol{C}_{FLD}^{loc} : \left[\boldsymbol{R}(\boldsymbol{p}) \,\overline{\otimes}\, \boldsymbol{R}(\boldsymbol{p}) \right], \tag{3.16} $$

$$ \begin{aligned} {}^4\boldsymbol{C}_{FLD}^{loc} = \int_0^\infty & w(l_F) \; {}^4C_{UC}(l_F) \\ & : \left[{}^4\boldsymbol{I} + {}^4\boldsymbol{E} : \left(\left[{}^4\boldsymbol{C}_C^{SC} \right]^{-1} : \; {}^4\boldsymbol{C}_{UC}(l_F) - {}^4\boldsymbol{I} \right) \right]^{-1} dl_F. \end{aligned} \tag{3.17} $$

With the Equations (3.13), (3.14) and (3.17), a representation of a unidirectional composite stiffness, representing the fibre length distribution can be found for each interaction assumption. This can subsequently be used further to apply the Orientation Averaging step. This method reduces the number of iterations in the numerical model and therefore results in a better performance than the first presented method. Note, however, that this simplification is only applicable in the linear elastic case. With the load history dependency in the elasto-plastic model, the local UC tangent stiffness is dependent on the load direction and, therefore, on the fibre direction $\boldsymbol{p}$. In this case, Equations (3.9) – (3.11) must be used.

The presented method displays some major benefits compared to the method using unidirectional RVEs. First, the method creates fully reproducible results since it does not contain any randomised values. Therefore, only one full simulation is necessary to obtain a reliable model prediction. Additionally, several fibre length distributions can be evaluated if other parameters, such as the fibre volume fraction, stay constant. Finally, fibre length dependent orientation distributions can be handled with this model. However, in many cases, this is not feasible due to the lack of information about the relation between the FOD and the fibre length. Nevertheless, one disadvantage cannot be denied. The computational costs are relatively high. This applies most for the elasto-plastic model, where the above-mentioned simplification is not applicable. Due to the number of variables and iterations in the OA-simulations which is increased severely by the additional integration over the fibre lengths, the computational time increases significantly.

3.3.3 Single representative fibre length

The simplest solution of representing FLDs is by replacing them with a single representative fibre length. It could be argued that a single fibre length cannot represent the local stress state of a certain fibre length. This may lead to errors when it comes to representing elasto-pastic matrix behaviour or material damage. However, in the linear elastic case, assuming a fibre length independent FOD, the fibre length average stiffness tensor presented in Equations (3.13), (3.14), and (3.17) can be calculated. Assuming the UC stiffness tensor being independent from the fibre length, apart from the fibre parallel component ($C_{1111}(l_F)$), a single, representative fibre length l_F^{rep} can be found, which equals the fibre length averaged stiffness tensor. The resulting fibre parallel composite stiffness is defined in case of the Voigt interaction assumption as:

$$C_{1111}^{UC}\left(l_F^{rep}\right) = \int_0^\infty f(l_F) \cdot l_F \cdot C_{1111}^{UC}(l_F) dl_F. \tag{3.18}$$

The use of a single representative fibre length for obtaining the composite material properties is quite common. In fact, most literature is presenting micro-mechanical model predictions for an SFRC, uses a representative fibre length to represent the FLD in form of a number-average of the fibre length [9, 40]. In *Hine, Lusti et al.*, it is stated that the linear elastic material response of an SFRC which FLD can be described by a *Weibull* distribution, can also be represented by the number-averaged fibre length of that FLD in the linear elastic mechanical simulations [25]. In that work, the authors investigate different averaging methods for obtaining the representative fibre length, such as the number- and the volume-averaged fibre lengths presented in Equations (3.4) and (3.6), respectively.

With the resulting representative fibre length, only one single UC must be generated and simulated, and one set of material parameters has to be obtained. Also, the Orientation Averaging process, described in Chapter 2.1.3, can be used for obtaining the homogenised composite response for this method. However, for changing FLDs, additional simulations have to be conducted each time. Also, the method is not able to represent fibre length dependent FODs. Another great disadvantage of the method, if using the number-average, is given by the fact that the averaging scheme for the fibre length does not take into account the nonlinear relation between fibre length and composite stiffness, which is shown in Chapter 3.1.

Again, it should be mentioned that the results from *Hine, Lusti et al.* are based on composites with a FLD following a *Weibull* PDF very strictly. Hence, other composites with FLDs deviating from that particular distribution function can lead to other results in evaluating the fit of the representative fibre length. This can be seen in *Breuer* and *Stommel*, where the FLD deviated strongly from the *Weibull* PDF (see Figure 3.4) [9]. The authors compare the homogenised composite stiffnesses of unidirectional RVEs using an equal representative fibre length, obtained by the number-average, and the measured FLD of the composite. The results show a major difference in the predicted composite properties. As the method using the number-averaged fibre length results in an average fibre parallel composite Young's modulus of around E_{11}^{num} = 6,500 MPa, the corresponding value for the simulations using FLDs results in E_{11}^{FLD} = 7,600 MPa [9].

3.3.4 Comparison of the presented methods

In the previous chapters, three different methods are presented on how to represent fibre length distributions in the Orientation Averaging procedure. In the following chapter the advantages and disadvantages of the solutions are discussed.

Using a unidirectional RVE, with integrated fibre length distribution for obtaining the unidirectional homogenised composite stiffness instead of a Unit Cell geometry is convincing at first sight. Not only could the pre-existing OA-model be continued to be used without any adaptions needed, but the capability of displaying some fibre interactions between the unidirectional fibres in the RVE is also a great advantage of this method. However, the numerous simulations needed for obtaining an average material response and the generally increased size of the numerical models increase the computational effort of the first homogenisation step of the two-step Orientation Averaging method significantly. Additionally, with this method, it is not possible to obtain predictions for composites with varying FLDs, without performing further RVE-simulations.

The second method, which is adding another averaging scheme on the second Orientation Averaging step, is the only one requiring an adaption of the pre-existing Orientation Averaging scheme. However, this method is the most flexible solution when it comes to representing varying fibre length distributions or fibre length dependent FODs. The additional averaging scheme in this model, however, increases the computational time of the Orientation Averaging step linearly with increasing number of considered fibre lengths. This is especially recognisable for the elasto-plastic version of the model.

Finally, replacing the FLD with a representative averaged fibre length is the fastest method of the three presented solutions. Only a singular UC-simulation must be conducted in the first step and in the second step, the pre-existing Orientation Averaging scheme can be applied. However, this method requires several numerical simulations in case of changing shapes of the FLD. Another problem of this method is the error that is produced by the nonlinear relation between fibre length and homogenised composite stiffness. A new method of obtaining a representative fibre length, which is capable of handling this effect, is presented in the following chapter.

To conclude this chapter, in Table 3.2, the evaluation of the three different models considering various aspects is summarised.

Table 3.2: Comparison of advantages and disadvantages of methods to represent FLDs in the Orientation Averaging method.

Aspect for the evaluation	**UD-RVE with FLD**	**Adapted OA-method**	**Representative fibre length**
Computational time in the volumetric homogenisation step (Step 1)	-	0	+
Computational time in the Orientation Averaging step (Step 2)	+	-	+
Representation of the full FLD	+	+	0
Adaptivity to varying FLDs	-	+	0
Number of model parameters	+	-	+
Fibre length dependent FOD	-	+	-

Positive evaluations of the aspects considering the specific method are marked with a "+", negative with a "-" and intermediate with a "0". According to this, the method using UD-RVEs with integrated fibre length distributions is considered as the least promising method. Also, it has been investigated thoroughly by several other authors. Therefore, it will not be considered in further investigations. The other two methods show potential in either adaptivity to varying parameters for the extended Orientation Averaging process, or time efficiency for the representative fibre length method. Both models will be considered and compared in further investigations.

3.4 The stiffness-averaged representative fibre length

In this chapter, a novel method for obtaining a representative fibre length from an arbitrary FLD is presented. Looking at the Orientation Averaging scheme for the linear elastic case, with integrated fibre length averaging using the Voigt assumption as presented in Equation (3.13), the fibre length average composite stiffness ${}^4\boldsymbol{C}_{FLD}^{Voigt}$ can be extracted as:

$$ {}^4\boldsymbol{C}_{FLD}^{Voigt} = \int_0^\infty w(l_F)\ {}^4\boldsymbol{C}_{UC}(l_F)\, dl_F. \tag{3.19} $$

Searching for a representative fibre length l_F^{rep} which stiffness tensor is equal to the fibre length average composite stiffness, the resulting UC-stiffness tensor can be expressed by the following relation:

$$ {}^4\boldsymbol{C}_{UC}\left(l_F^{rep}\right) = {}^4\boldsymbol{C}_{FLD}^{Voigt} = \int_0^\infty w(l_F)\ {}^4\boldsymbol{C}_{UC}(l_F)\, dl_F = \frac{\int_0^\infty f(l_F)\, l_F\ {}^4\boldsymbol{C}_{UC}(l_F)\, dl_F}{\int_0^\infty f(l_F)\, l_F\, dl_F}. \tag{3.20} $$

Considering this, a similar relation could be found for the homogenised Young's moduli $E_{ii}(l_F)$.

$$ E_{ii}^{UC}\left(l_F^{rep}\right) = \int_0^\infty w(l_F)\, E_{ii}^{UC}(l_F)\, dl_F = \frac{\int_0^\infty f(l_F)\, l_F\, E_{ii}^{UC}(l_F)\, dl_F}{\int_0^\infty f(l_F)\, l_F\, dl_F}. \tag{3.21} $$

Previous observations show that it is mainly the fibre parallel Young's modulus $E_{11}(l_F)$ that is significantly depending on the fibre length. From that, the new averaged fibre length can be found by replacing the variable l_F in the integral expression of the denominator of Equation (3.21) with the fibre parallel Young's modulus $E_{11}(l_F)$. This transforms the resulting value from the average Young's modulus to an average value representing a length unit. The resulting expression can be interpreted as stiffness-averaged fibre length l_F^{stiff}, which is given by

$$ l_F^{rep} = \frac{\int_0^\infty f(l_F)\, l_F\, E_{11}^{UC}(l_F)\, dl_F}{\int_0^\infty f(l_F)\, E_{11}^{UC}(l_F)\, dl_F}. \tag{3.22} $$

Obtaining the fibre parallel UC-Young's modulus in dependency of the fibre length from numerical simulations, would counteract the main benefit of the method using a single representative fibre length. This is reducing the number of numerical simulations needed. Hence, analytical models should be utilised to obtain this value. Figure 3.2 shows that the *Halpin-Tsai* model gives the closest prediction of the fibre parallel UC-Young's modulus in comparison to the UC-simulations with the given parameter set. Also, it is represented by a relatively simple relation for the required value [2, 23]:

$$E_{11}^{UC,HT}(l_F) = \frac{1 + 2(l_F/d_F) \cdot \eta \cdot \varphi}{1 - \eta \cdot \varphi} E_M, \tag{3.23}$$

$$\eta = \frac{E_F/E_M - 1}{E_F/E_M + 2 \cdot (l_F/d_F)}. \tag{3.24}$$

Notice that the representative fibre length l_F^{stiff} is now not only dependent on the length distributions itself, but also on material parameters defining the composite constitution, which are namely the Young's moduli E_F and E_M, the fibre volume fraction φ and the fibre diameter d_F. Other analytical models could as well be applied to obtain the fibre length dependent Young's modulus.

In analogy to the volume-weighted fibre length distribution, a stiffness-weighted FLD $e(l_F)$ can be obtained from the general FLD as:

$$e_F^{rep}(l_F) = \frac{f(l_F)\, E_{11}^{UC}(l_F)}{\int_0^\infty f(l_F)\, E_{11}^{UC}(l_F)\, dl_F}. \tag{3.25}$$

For a better comparison with the other averaging methods, presented in Chapter 3.3.3, the normalised weighting factor F_i is introduced. The respective weighting factors are normalised with their integral over the fibre length range. The normalised weighting factor is described for the stiffness-averaged weighting factor with

$$F_{stiff} = \frac{E_{11}^{UC}(l_F)}{\int_0^\infty E_{11}^{UC}(l_F)\, dl_F}. \tag{3.26}$$

For the comparison between the three averaging methods, the corresponding weighting factors are plotted qualitatively in a graph in Figure 3.5. In case of the number-averaged fibre length, this factor is constant for all fibre lengths. The weighting factor of the volume-average is proportional to the fibre length l_F and, therefore, varies as a linear function. Consequently, the weighting for the stiffness-average is proportional to the fibre parallel Young's modulus $E_{11}^{UC}(l_F)$. It is observed that, in comparison to the other methods, the number-averaged weighting factor has the highest influence on shorter fibres while long fibres are taken into account with a relatively low weight. This shifts the averaged fibre length towards a lower value. In analogy to this, the weighting factor for the volume-averaged fibre length displays the complete opposite. Accordingly, the correspoding averaged fibre length is estimated with a

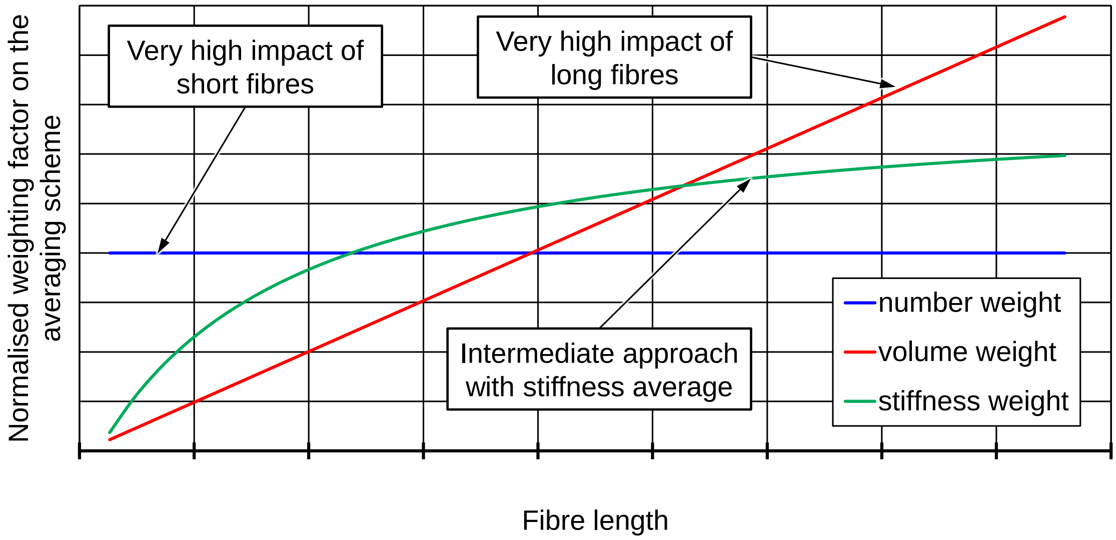

Figure 3.5 Weighting factor of different averaging methods for the corresponding averaged fibre lengths.

higher value. The stiffness weighting factor, however, seems to produce an intermediate averaged fibre length with the weighting factor in-between the two aforementioned approaches for extreme values of fibre length. Note that for higher fibre lengths, the composite stiffness converges to a constant value approaching the stiffness value of a continuous fibre reinforced composite. Hence, the weighting of higher averaged fibre lengths with the UC-stiffness approximates the number-average.

The described order of the presented fibre length averages can be confirmed by Figure 3.6.

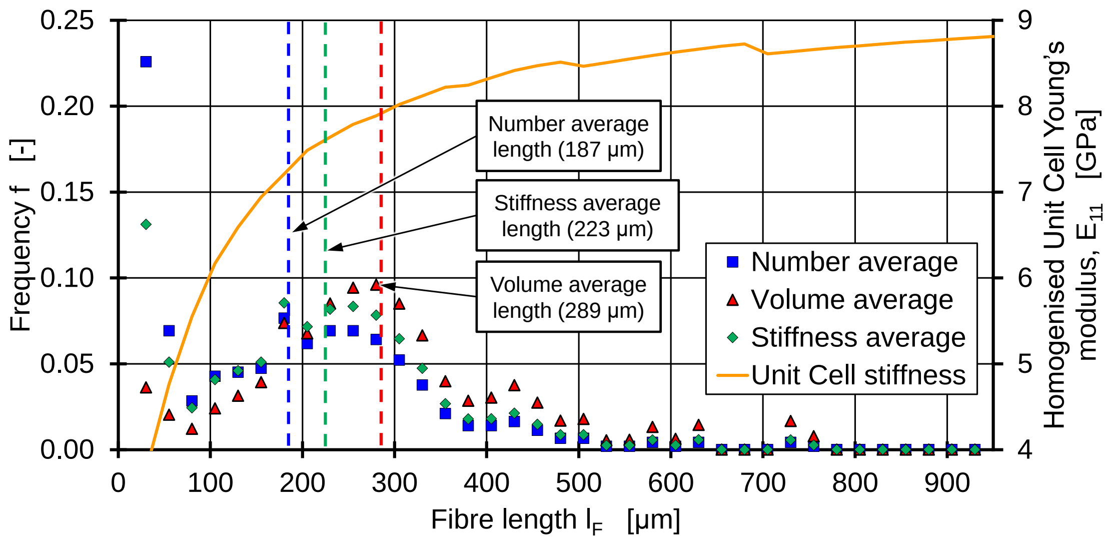

Figure 3.6: Comparison of the three weighted length averages on FLD from Breuer, Stommel et al. [9].

Here, the three averaging techniques are applied on the FLD taken from *Breuer, Stommel et al.* that is already used in Chapter 3.2 [9]. The dots in the graph represent the fibre length distributions, weighted with the corresponding weighting method. Hence, the blue squares mark the number-weighted FLD, the red triangles the volume-weighted FLD in analogy to $w(l_F)$ and the green diamonds could be considered as the stiffness-weighted FLD ($e(l_F)$). The impact of the weighting can be clearly observed, especially for the lowest fibre length class. Comparing the stiffness-weighted distribution with the other two weighting methods, the stiffness-weighted frequency takes on an intermediate value. With increasing fibre lengths, in the range of 135 – 230 µm, the weighting methods produce similar frequencies. For higher fibre lengths, the volume-weighted FLD produces significantly higher frequencies than the other two methods, approach each other to similar values. The resulting averaged fibre lengths are marked by the dashed lines in the respective color to the averaging technique. Their values are in the expected order, as the number-averaged fibre length represents the minimum, with l_F^{num} = 187 µm, the volume-averaged fibre length equals l_F^{vol} = 289µm and the stiffness-averaged fibre length gives an intermediate result with l_F^{stiff} = 223 µm, obtained using the *Halpin-Tsai* model.

In Figure 3.6, the resulting homogenised UC Young's modulus dependent on the fibre length is represented by the solid line corresponding to the secondary vertical axis on the right side of the graph. Tracing the corresponding UC-stiffness from the three different averaged fibre lengths to the scale shows significant differences in the resulting homogenised stiffnesses. Conducting UC-simulations with the respective fibre lengths resulted in homogenised UC-stiffnesses in 1-direction of $E_{11}^{UC}(l_F^{num})$ = 7,293 MPa for the number-averaged fibre length, $E_{11}^{UC}\left(l_F^{vol}\right)$ = 7,938 MPa for the volume-averaged fibre length and $E_{11}^{UC}\left(l_F^{stiff}\right)$ = 7,591 MPa for the stiffness-averaged fibre length.

In comparison to this, in Figure 3.7 the same graph is presented using the measured frequencies of the other FLD presented in Chapter 3.2, the 30 %wt. glass fibre reinforced Polyamide composite taken from *Holmström, Hopperstad et al.* [27]. The graph shows the number-

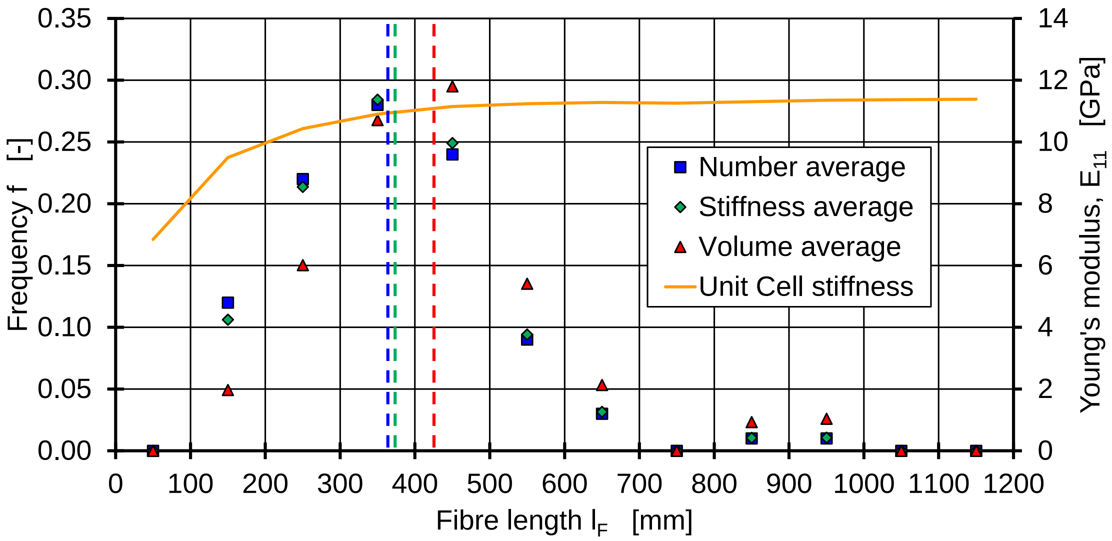

Figure 3.7: Comparison of the three weighted length averages on the FLD from Holmström, Hopperstad et al. [27].

averaged and the stiffness-averaged representative fibre length being very close to each other with l_F^{num} = 366 µm and l_F^{stiff} = 373 µm. Hence, the resulting homogenised UC-stiffnesses in fibre direction from both numerical simulations result in relatively similar stiffnesses with either $E_{11}^{UC}(l_F^{num})$ = 10,974 MPa for the number-averaged fibre length, or $E_{11}^{UC}\left(l_F^{stiff}\right)$ = 11,000 MPa for the stiffness-averaged fibre length. For the volume-averaged fibre length, with l_F^{vol} = 425 µm the resulting fibre parallel UC-stiffness is slightly higher with

$E_{11}^{UC}\left(l_F^{vol}\right)$ = 11,129 MPa. However, the difference compared to the other representative fibre lengths is not very significant and is well within the range of a experimental scattering.

This shows that the stiffness-averaged fibre length is a reasonable addition to the methods of obtaining representative fibre lengths to describe a FLD. The incorporation of the nonlinear relation between composite stiffness and fibre length promises a more accurate prediction of the homogenised UD-composite behaviour. The benefit of using this method compared to the alternative methods of using representative fibre lengths and also the fibre length averaging aproach is investigated in the results and discussion chapter of this work (Chapter 5).

3.5 Modeling fibre length distributions in the elasto-plastic case

In this chapter, the applicability of the presented methods is discussed in respect to the elasto-plastic modelling. The method using UD-RVEs with integrated fibre lengths is directly transferable from the linear elastic case to the elasto-plastic case. A single surrogate model would have to be fit to the average material response of the numerous RVE-simulations. The model parameters could then be directly fed into the pre-existing Orientation Averaging process for elasto-plastic material behaviour.

The second presented method, which adds another averaging scheme to the Orientation averaging process, could also be applied as first described. However, the simplification of using a fibre length average composite stiffness tensor, which is then rotated into different orientations is not applicable for the elasto-plastic case. Due to the history dependent tangent stiffness of the UC, the material response is dependent on the load direction and equivalently on the fibre direction $\boldsymbol{p}$. Hence, the OA-process must be performed with the computationally more expensive method. Another disadvantage of this model occurs when calibrating the surrogate model parameters from an optimisation method. Because several UC-simulations with different fibre lengths are required for this method, each demanding an independent set of parameters, the calibration procedure is a very time-consuming task. However, this method has to be conducted only once and the parameters found are then valid, also for changing FLDs.

Finally, the method using a single representative fibre length is investigated. In Figure 3.8, the evolution of the fibre length dependent stress-strain gradient $\Delta\sigma_{11}(l_F, t)/\Delta\varepsilon_{11}(t)$ for increasing strain in 11-direction is presented for the case of a uniaxial stress state. It can be seen that the evolution is quite different for varying fibre lengths. For example, for shorter fibre lengths, the decrease in the tangent stiffness is significantly higher for the first 2 % of strain. For higher strains it approaches a constant value. On the contrary, for higher fibre lengths, the loss of tangent stiffness in the first 2 % strain is lower than in the previous example. For increasing strains up to 5 % the reduction of the tangent stiffness also decreases, however, it does not converge to a constant value. Based on these observations, it is questionable, if a single fibre length is capable of replicating that effect instead of a full FLD.

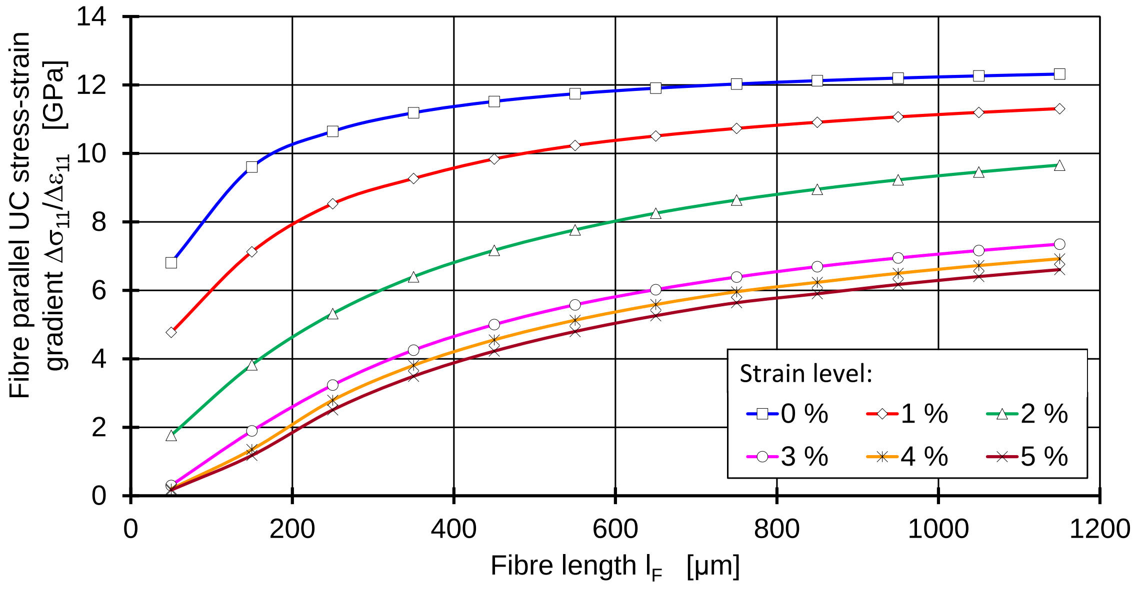

Figure 3.8: Length dependent fibre parallel stress-strain-gradient at certain levels of strain for the uniaxial stress load case.

From Figure 3.8 it can also be expected that a stiffness-averaged fibre length based on the stress-strain gradient in 11-direction would change with increasing strains. Hence, in Figure 3.9, this value is plotted in against increasing strain. It can be observed that the stiffness-averaged fibre length drifts towards higher values with increasing UC strain. This indicates that the homogenised elasto-plastic composite response with integrated FLDs can not be replaced by a single representative fibre length. This is also further investigated in the following chapters of this work.

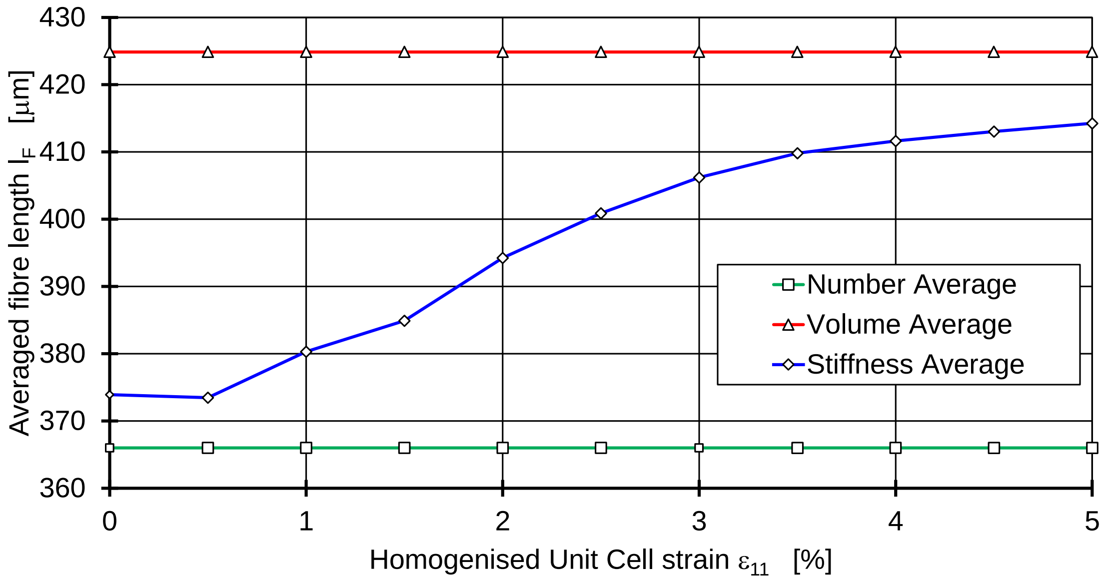

Figure 3.9: Evolution of the averaged representative fibre lengths based on the tangent UC-stiffness.

4 IMPLEMENTATION AND METHODS

In the previous chapter, different modelling approaches to represent FLDs in a short fibre reinforced composite have been presented. Their feasibility and predictive accuracy are evaluated in this work. To do so, some necessary procedures need to be implemented. These procedures are described in the following chapter.

In order to represent the fibre orientation distribution function on a discretised unit sphere, the icosphere shape is used based on the method presented in *Breuer, Stommel et al.* [10]. The procedures for this are explained in more detail in Subsection 4.1. In Subsection 4.2, the realisation of the linear elastic two-step Orientation Averaging procedure is described. Then, in Subsection 4.3, the determination of the model parameters for the elasto-plastic surrogate model is described, before the elasto-plastic Orientation Averaging procedure is explained in Subsection 4.4.

In general, all procedures are implemented in Python using basic libraries such as Numpy [24], Scipy [57] and Pandas [35]. The code is based on the previous models developed in MATLAB in several different steps [5, 18, 36, 39].

To improve the performance of the code most basic functions were optimised using the Numba inline compiler [31]. It is particularly effective on math operations-heavy computations and programs containing several nested loops. Many Numpy functions can also be optimised with this tool. The compiler is applied as a decorator on special functions, which show potential for optimisation. With this, the performance of the presented applications is improved to substantially lower computation times, which increases the feasibility of excessive testing on the presented methods. Not every function showing potential for optimisation is treated with the Numba compiler wrapping, since its application needs some adjustments in the script. For example, it is not completely clear to which extent the Orientation Averaging methods can be optimised with this. However, there is still potential for further optimisation using this compiler. This should be considered in further investigations of the Python model.

4.1 Orientation distribution functions represented by the icosphere

As described earlier, in order to conduct the Orientation Averaging, it is necessary to represent the fibre orientation distribution function or tensor with a finite set of fibre orientations. Two different methods are possible for this purpose. For the first option, a set of randomly sampled fibre orientations, based on the fibre orientation distribution function is created. In the Orientation Averaging step each fibre orientation is then applied separately with equal weighting. This approach was used in earlier methods for the Orientation Averaging procedures [39]. However, to represent the FOD properly, large numbers of fibre orientations must be generated. Also, the randomised orientation sampling can introduce scattering of the Orientation Averaging results.

In this work, another method is used, which is based on a discretised unit sphere structure. For this, the unit sphere, which represents the set of all possible fibre orientations in three dimensions, is divided into equally sized sub-shapes, which then get assigned a probability value based on the particular FOD. The benefits of this method are the reproducibility and the necessity of a smaller number of orientations for an appropriate representation of the FODF.

The equal size of the discretisation shapes is important, to ensure the probability value of the respective shape being independent on the area represented by the shapes. *Breuer, Stommel et al.,* proposed a method for discretising the unit sphere, using the icosphere geometry [10]. The icosphere shape consists of triangles of the same size approximating the unit sphere. The starting shape is a regular icosahedron. It consists of 20 equilateral triangles with their vertices positioned on the unit sphere. Each triangle is subdivided into four smaller triangles in every refinement step and the new produced vertices are then projected on the unit sphere surface. A visualisation of an icosphere with different refinements is given in Figure 4.1. [10]

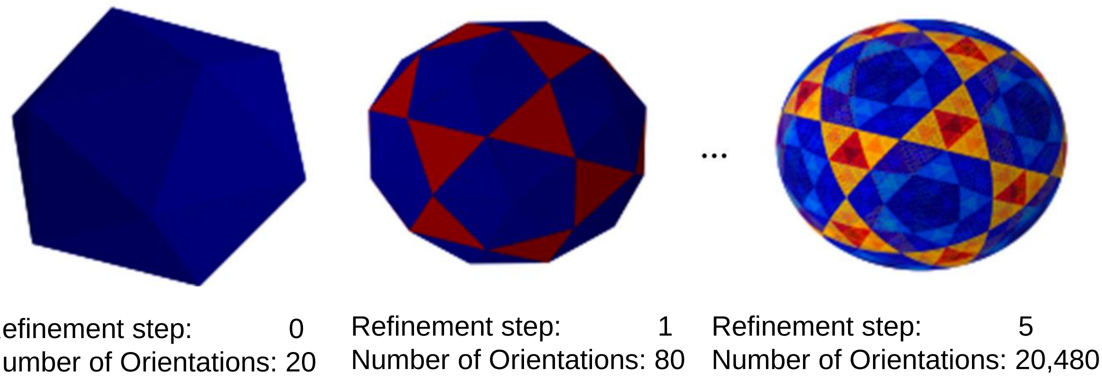

Figure 4.1: Discretisation of the unit sphere using the icosphere geometry with different levels of refinement [10].

The number of triangle elements in an icosphere increases exponentially with every refinement step. So that with just 5 refinements, 20,480 elements are used to approximate the sphere. The equation for obtaining the number of fibre orientations n_{ori} based on the number of refinements n_{ref} is given as follows:

$$n_{ori} = 20 \cdot 4^{n_{ref}}. \tag{4.1}$$

The refinement of the icosphere shape is programmed recursively. With a refinement step, each triangle shape produces its four sub-triangles, which then can produce their own sub-triangles in the following refinement step. A visualisation of the creation process of the icosphere can be found in Figure 4.2.

To obtain the probability value for a triangle section, the FODF is evaluated at the mass centre of the shape. In case of a requested fibre orientation distribution, the probability values are evaluated for the lowest layer of triangle shapes, again as a recursive process. As a result, each triangle's central vector as well as the corresponding probability value are returned. The probability values are normalised to the sum of each individual probabilities to ensure a summation to 1. This can then be processed in the Orientation Averaging process, but also for determining the FODT. Another benefit of the presented method is the ability for a more systematic representation of the orientation distribution on the unit sphere as it is shown in Figure 4.3. The corresponding FODT to the presented FODF is a diagonal tensor with the eigenvalues λ_1 = 0.711, λ_2 = 0.244 and λ_3 = 0.045 taken from *Breuer, Stommel et al.* [9].

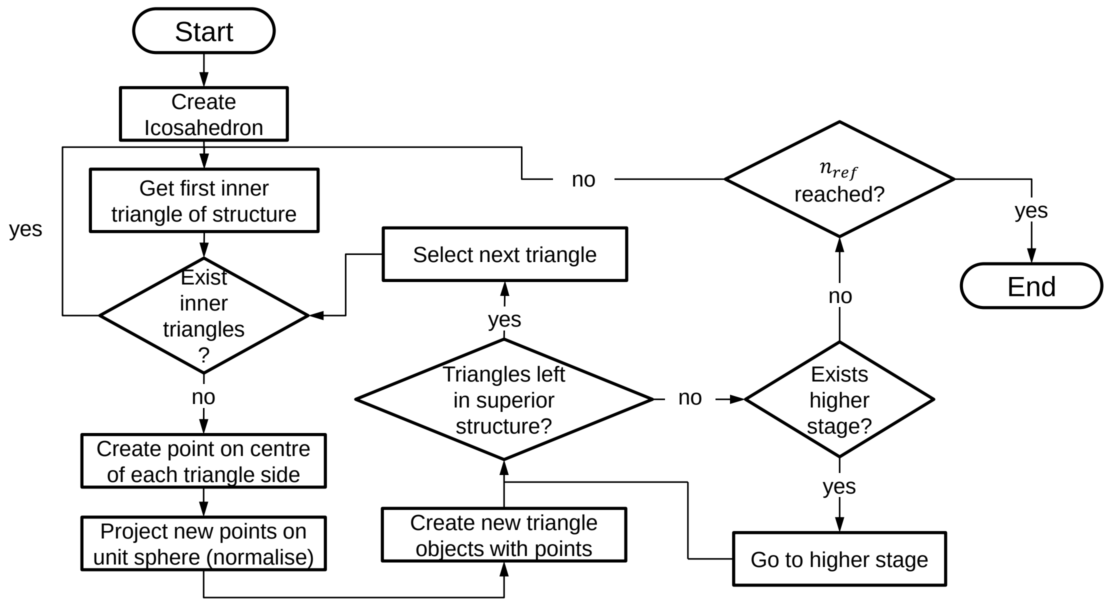

Figure 4.2: Algorithm workflow of creating the icosphere geometry with n_{ref} refinement steps in a recursive progress.

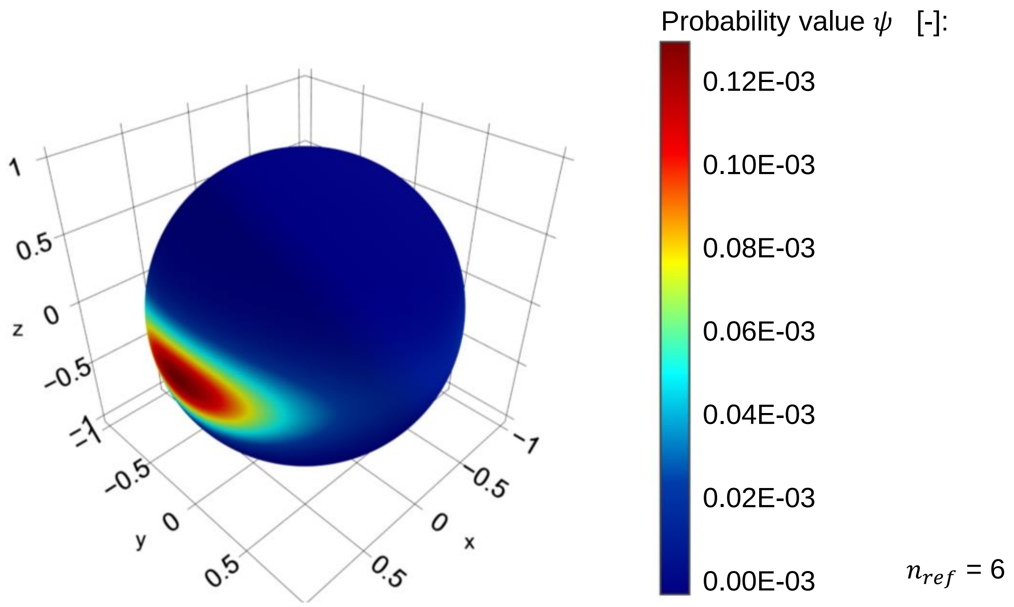

Figure 4.3: Exemplary fibre orientation distribution plotted on the unit sphere created with the icosphere discretisation algorithm.

It can be observed that for this specific FOD, a large area with very low probabilities evolve. These areas are marked by the dark blue colouring in the figure. From the evaluation of the impact of Bingham parameters on the PDF, it can be observed that these low probabilities can deviate from the average probability by more than four orders of magnitude. The average probability of a unit sphere approximated by an icosphere is equal to the inverse of the number of triangle shapes $1/n_{ori}$. This is based on the facts that for a 3D-random FOD each triangle shape has an probability and the sum over all probabilities equals unity. It is obvious that such low probabilities do not have an influence on the average material parameters in the Orientation Averaging process. Therefore, for improvements in the performance of the model, very low probabilities compared to the average probability can be neglected in the Orientation Averaging procedure.

In a previous work by *Castricum*, the *Bažant* integration scheme was introduced as an efficient method for the integration over a unit sphere [4, 13, 14]. This was realised in the context of an implementation of the elasto-plastic Orientation Averaging method in a macroscopic finite element code. The method was used to represent a 3D-random FOD. However, it is also possible to represent different distributions with this scheme by using the local values of the FODF. Due to the lower number of integration points used with the *Bažant* integration scheme, the computational efficiency is considered much higher than with the presented icosphere method. Nevertheless, the method used here is considered more suitable for representing FODs varying from the 3D-random case, due to its higher resolution. The efficiency of the here presented method could be, furthermore, increased with a locally adjustable resolution.

With obtaining the finite set of fibre orientations in combination with the corresponding probabilities, all necessary information about the FOD is gathered. Accordingly, it can be continued with the Orientation Averaging process.

4.2 Linear elastic Orientation Averaging with fibre length distributions

In the following chapter, the process of obtaining the linear elastic homogenised composite stiffness tensor with the two-step Orientation Averaging method with included fibre length averaging is presented. First, the fibre length distribution must be obtained from the material data and converted to a discretised form. With the FLD usually given as frequencies of certain length intervals, this can be taken directly from the data source. However, too small intervals should be avoided for the presented method, for performance reasons not only in the Orientation Averaging procedure but more importantly for the numerical simulation. In the case of too high resolution of the FLD, multiple neighboured fibre length classes could be combined to a larger class. Each fibre length class is represented by a single fibre length, defined by the centre of the range of fibre lengths. In the next step, the material response of the UCs with fibre lengths according to the fibre length classes is obtained by numerical simulations according to the method described in Chapter 2.1.2.1. Subsequently, the FOD can be obtained and converted to a discretised FODF according to Chapter 4.1. With this, all information is present to start the Orientation Averaging process.

The analytical model for the Orientation Averaging is given in Equations (3.9) – (3.11) with the respective fibre interaction assumption. The relations must be adopted for the discretised version of the implemented model. For that, the integrals are replaced by sums over the number of fibre length classes n_{len} and fibre orientations n_{ori}. The equations for the Voigt, Reuss and self-consistent assumptions follow in order:

$$
\begin{aligned}
{}^4\boldsymbol{C}_C^V = \sum_{i=1}^{n_{len}} w_i(l_{F,i}) \sum_{j=1}^{n_{ori}} \psi_j(\boldsymbol{p}_j, l_{F,i}) \left[\boldsymbol{R}^T(\boldsymbol{p}_j) \overline{\otimes} \boldsymbol{R}^T(\boldsymbol{p}_j)\right] : \ {}^4\boldsymbol{C}_{UC}(l_{F,i}) \\
: \left[\boldsymbol{R}(\boldsymbol{p}_j) \overline{\otimes} \boldsymbol{R}(\boldsymbol{p}_j)\right],
\end{aligned}
\qquad (4.2)
$$

$$
{}^4\boldsymbol{C}_C^R = \left\{ \sum_{i=1}^{n_{len}} w_i(l_{F,i}) \sum_{j=1}^{n_{ori}} \psi_j(\boldsymbol{p}_j, l_{F,i}) [\boldsymbol{R}^T(\boldsymbol{p}_j) \otimes \boldsymbol{R}^T(\boldsymbol{p}_j)] : \left[{}^4\boldsymbol{C}_{UC}(l_{F,i}) \right]^{-1} : [\boldsymbol{R}(\boldsymbol{p}_j) \overline{\otimes} \boldsymbol{R}(\boldsymbol{p}_j)] \right\}^{-1}, \tag{4.3}
$$

$$
{}^4\boldsymbol{C}_C^{SC} = \sum_{i=1}^{n_{len}} w_i(l_{F,i}) \sum_{j=1}^{n_{ori}} \psi_j(\boldsymbol{p}_j, l_{F,i})\ {}^4\boldsymbol{C}_{UC}^{glob}(\boldsymbol{p}_j, l_{F,i}) : \left[{}^4\boldsymbol{I} + {}^4\boldsymbol{E} : \left(\left[{}^4\tilde{\boldsymbol{C}}_C^{SC} \right]^{-1} : {}^4\boldsymbol{C}_{UC}^{glob}(\boldsymbol{p}_j, l_{F,i}) - {}^4\boldsymbol{I} \right) \right]^{-1}, \tag{4.4}
$$

$$
{}^4\boldsymbol{C}_{UC}^{glob}(\boldsymbol{p}_j, l_{F,i}) = [\boldsymbol{R}^T(\boldsymbol{p}_j) \overline{\otimes} \boldsymbol{R}^T(\boldsymbol{p}_j)] : {}^4\boldsymbol{C}_{UC}(l_{F,i}) : [\boldsymbol{R}(\boldsymbol{p}_j) \overline{\otimes} \boldsymbol{R}(\boldsymbol{p}_j)]. \tag{4.5}
$$

Note that the discretised FLD w_i and FOD ψ_j need to be normalised in such a way that the sum over all probabilities equals one:

$$
\sum_{i=1}^{n_{len}} w_i(l_i) = \sum_{j=1}^{n_{ori}} \psi_j(\boldsymbol{p}_j, l_{F,i}) = 1. \tag{4.6}
$$

Figure 4.4 shows the realisation of the mentioned relation for an underlying Voigt assumption in relation to the complete two-step Orientation Averaging process. The two iterations, which

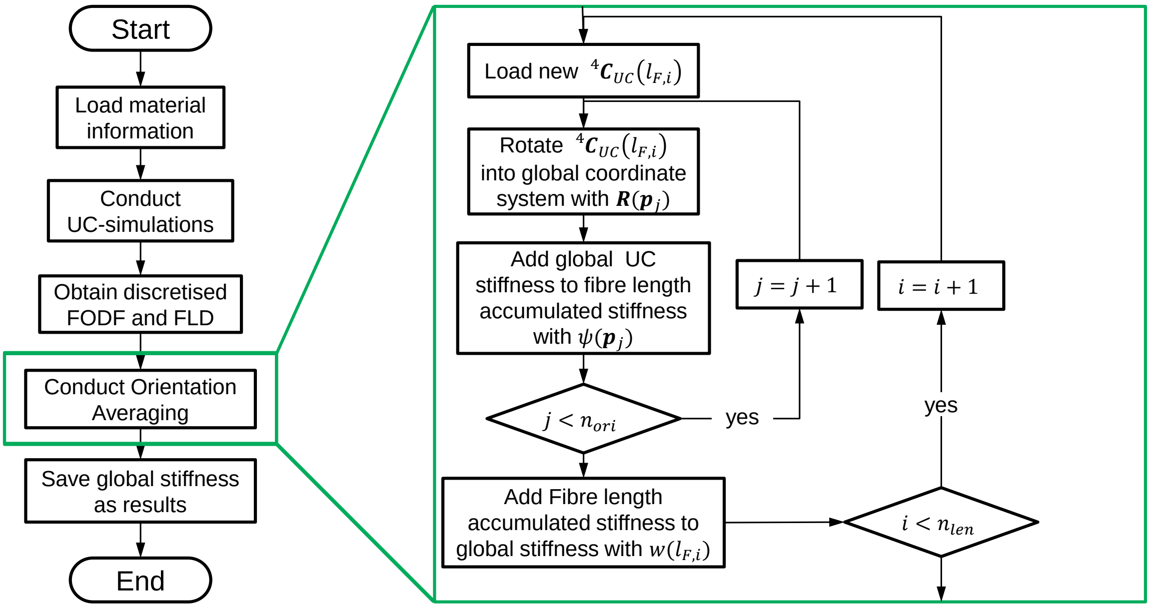

Figure 4.4: Algorithm workflow of the Orientation Averaging process for the linear elastic case using the Voigt interaction assumption.

can be found in the process represent the summations in Equation (4.2). This general procedure can be found for all three interaction assumptions.

The self-consistent assumption, however, requires a third iterative process, to approximate the resulting composite stiffness. For that a fixed-point iteration is used (for details, see [38]). At the beginning, an initial composite stiffness ${}^{4}\tilde{\boldsymbol{C}}_{C}^{SC}$ is assumed. An Orientation Averaging prediction using one of the other interaction assumptions is an appropriate solution for that. In this case, the Voigt assumption is chosen. With this, an estimation of the composite stiffness is computed using Equation (4.4). The resulting stiffness is then compared to the previous estimate and an error value is computed by:

$$\epsilon_{it} = max\left(\left|\frac{C_{C,ij}^{SC} - \tilde{C}_{C,ij}^{SC}}{\tilde{C}_{C,ij}^{SC}}\right|\right). \tag{4.7}$$

Finally, the initial composite stiffness is replaced by the recently calculated composite stiffness and the process is repeated until ϵ_{it} reaches a predefined tolerance. With this, the Orientation Averaging procedure for the linear elastic case is fully described.

4.3 Parameter fitting for the elasto-plastic surrogate model

For the elasto-plastic Orientation Averaging routine, the local Unit Cell response is described by the surrogate material model described in Chapter 2.1.2.2. To obtain the necessary material parameters, the model is calibrated to the UC-simulations in an optimisation process. In this chapter, the principals of the numerical UC-model are described and later, the optimisation process for obtaining the material parameters is explained.

The simulations are carried out in ABAQUS from Dassault Systémes, Véllzy-Villacoublay, France. This provides the opportunity to run the simulations fully automated on the C3SE cluster resources at Chalmers University of Technology. ABAQUS Scripting is used for pre- and post-processing and periodic boundary conditions are applied using an open source method supplied by *Overvelde* [48]. The Unit Cell geometry is created according to the method explained in Chapter 2.1.2. Fibre and matrix are connected via tie constraints on the corresponding surfaces. For the fibre component a linear elastic material model with isotropic properties is chosen. The matrix is also modelled with isotropic behaviour, but elasto-plastic behaviour is applied. For the plastic behaviour, a von Mises yield criterion is used with linear hardening. In order to stay in the range of small strains, the maximum displacement applied on the UC-surfaces is restricted to a maximum strain of 5 % in all four tested directions. The displacement is applied linearly increasing over the step time. With the developed script it is possible to create the complete FE-model, conduct the simulations and extract the stress-strain response from the results-file fully automatically.

With the material behaviour obtained by the numerical model, the next step is to find a fitting set of parameters which represent the material behaviour of the numerical model. The fitting of the surrogate model is realised, by a stepwise comparison of the FE-simulation results with the corresponding surrogate model predictions. Both stress and strain response need to be considered in the fitting procedure, since strain controlled uniaxial stress load cases are applied in the simulations. Therefore, the objective function ϵ for the optimisation problem results in:

$$\epsilon_{fit} = \sum_{n=1}^{4} \left(\frac{\int \left\| \boldsymbol{\sigma}_n^{sim}(t) - \boldsymbol{\sigma}_n^{model}(t) \right\|^2 dt}{\int \left\| \boldsymbol{\sigma}_n^{sim}(t) \right\|^2 dt} + \frac{\int \left\| \boldsymbol{\varepsilon}_n^{sim}(t) - \boldsymbol{\varepsilon}_n^{model}(t) \right\|^2 dt}{\int \left\| \boldsymbol{\varepsilon}_n^{sim}(t) \right\|^2 dt} \right), \tag{4.8}$$

with n representing each load case simulated with the numerical model. In theory, other load cases could be applied in addition to the ones presented. But in this case, it is assumed that the four load cases, with each fibre parallel and transverse, normal and shear loads, define the full material behaviour adequately. For the optimisation process, the Scipy 'optimize.minimize'-function is used. The function provides a variety of different optimisation algorithms. In this case, the Sequential Least Squares Programming (SLSQP) algorithm is used for all optimisation routines.

Eight independent surrogate model parameters need to be calibrated to the numerical simulations. Applying a single optimisation for obtaining all parameters results in an instable optimisation process, which outcome is largely dependent on the initial set of parameters. Therefore, the model fitting is split up in several parts, optimising smaller sets of parameters at a time. First, the elastic model parameters are obtained, defined by the three independent parameters E, ν and k. The optimisation is conducted for the elastic part of the numerical model, fixed by a value for the maximum strain of 0.3 %. The residual model parameters are excluded from the optimisation process and the occurrence of plastic deformation is prohibited by defining an exceedingly high yield stress σ_y with 1000 MPa.

Secondly, the yield stress parameter σ_y is obtained. This parameter defines the yield stress in the transverse direction. Since no well-defined yield point can be found in the numerical simulation, the stress at 0.2 % plastic strain is used. This method is a standard for obtaining the yield stress in the mechanical testing of metal materials [28]. Figure 4.5 visualises the construction of this value in the stress strain curve for the transverse, normal loading condition.

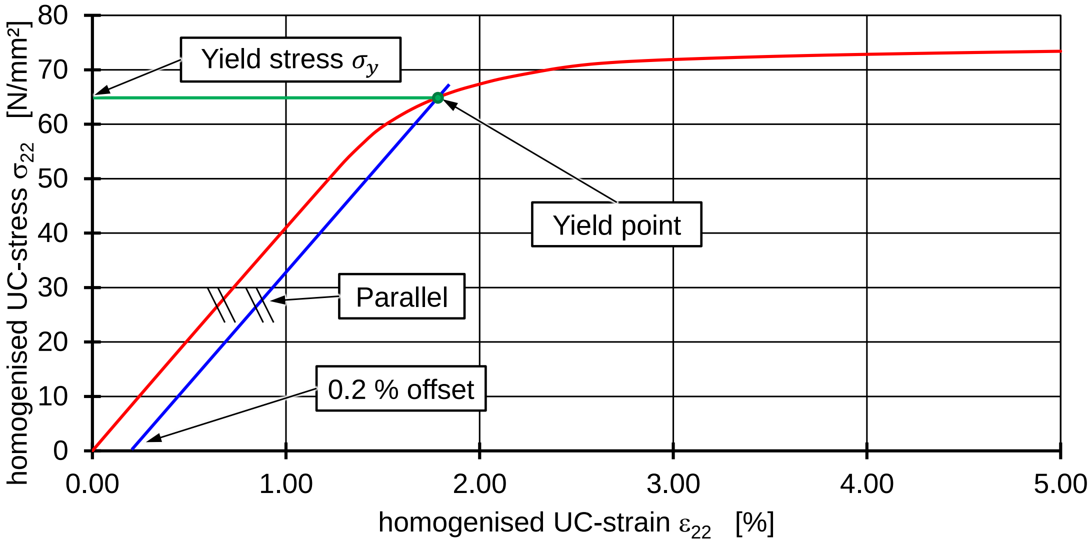

Figure 4.5: Construction of the fibre transverse yield point using the 0.2 % offset rule.

The obtained behaviour is compared to the initial linear elastic behaviour of the material with a 0.2 % offset. This is done by comparing the stresses of these functions for every time increment in the numerical simulation. The comparison is stopped, when the linear elastic stress $\sigma_{22}^{el}(\varepsilon_{22}(t) - 0.002)$ exceeds the stress in the numerical simulation $\sigma_{22}^{sim}(\varepsilon_{22}(t))$. Subsequently, the exact yield stress is approximated with linear interpolation between the last and the current timestep with

$$\Delta\sigma_i \coloneqq \sigma_{22}^{sim}\big(\varepsilon_{22}(t_i)\big) - E_{22} \cdot (\varepsilon_{22}(t_i) - 0.002) = \sigma_{22}^{sim}(t_i) - \sigma_{22}^{el}(t_i), \tag{4.9}$$

$$\sigma_y = \sigma_{22}^{sim}(t_{i-1}) - \Delta\sigma_{i-1} \cdot \frac{\sigma_{22}^{sim}(t_i) - \sigma_{22}^{sim}(t_{i-1})}{\Delta\sigma_i - \Delta\sigma_{i-1}}. \tag{4.10}$$

With the yield stress obtained, in the third step, the remaining plasticity parameters (R, κ_1, κ_2, κ_3) can be evaluated. This is done with two consecutive optimisation processes. In the first process, only the stress responses are considered in the objective function. For this, Equation (4.8) is adjusted to only consist of the part referring to the stress response. In the second step, the full objective function is taken into account. This method proves to produce more stable results in the optimisation process of the surrogate model, than directly using the full objective function in a single optimisation step.

With this, the full material model is obtained. In Figures 4.6 and 4.7 an example material model fit is compared to the corresponding UC-simulations. The presented material response

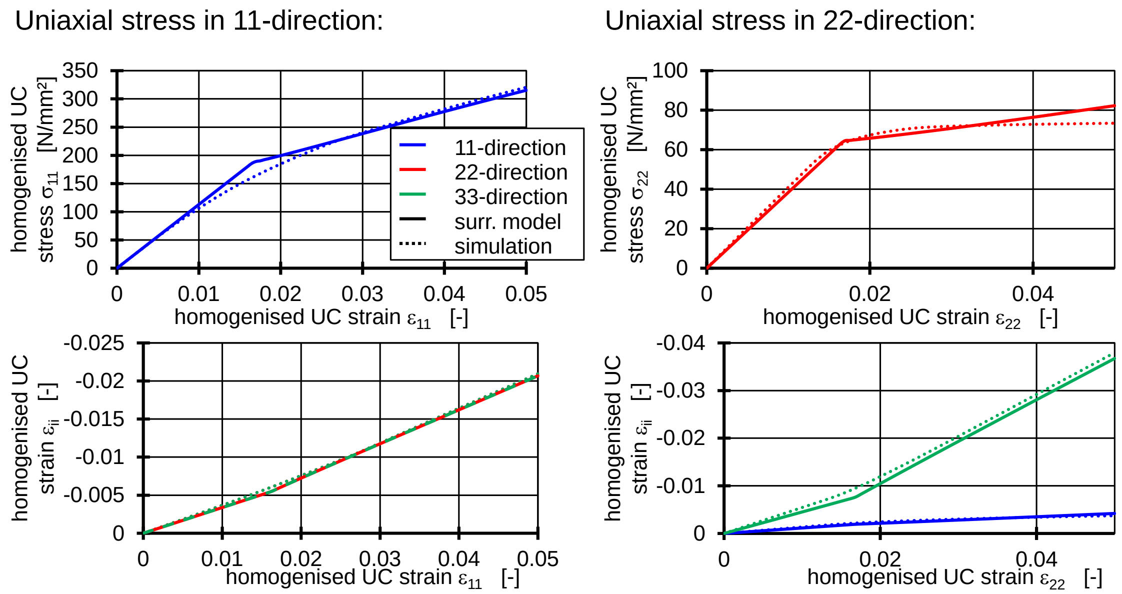

Figure 4.6: Exemplary comparison of elasto-plastic surrogate model predictions with UC-simulation results (normal load cases).

corresponds to a 30 %wt. glass fibre reinforced Polyamide composite presented *in Holmström et al.* with a stiffness averaged fibre length of 372 µm [27]. Further details on the material properties are discussed in Chapter 5. It can be seen that a good model fit for the elastic as well as the elasto-plastic domain could be found. However, in some parts, for example for higher strains in the transverse stress case, it becomes apparent that the material behaviour can not be perfectly described. The corresponding objective function value for the elastic domain equals $\epsilon_{fit}^{el} = 2.255 \cdot 10^{-2}$. The objective function for the full elasto-plastic model results to

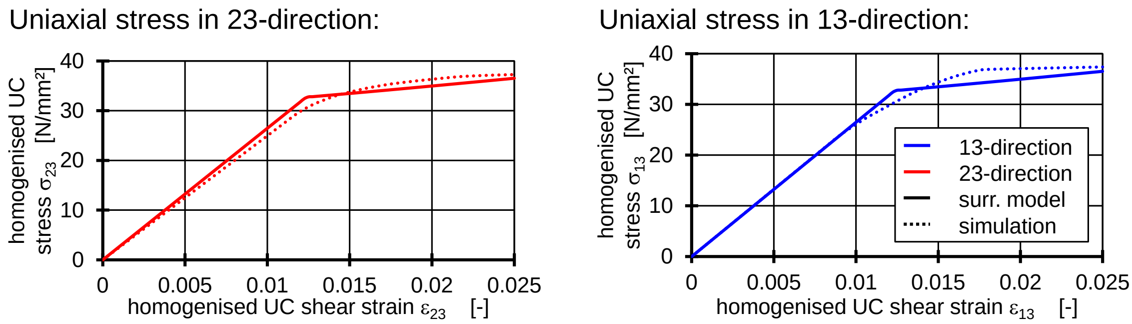

Figure 4.7: Exemplary comparison of elasto-plastic surrogate model predictions with UC-simulation results (normal load cases).

$\epsilon_{fit}^{pl} = 8.010 \cdot 10^{-3}$. With this, the surrogate model can be considered as a good fit to the Unit Cell behaviour. The resulting parameters from that model calibration can be found in Table 4.1.

Table 4.1: Model calibration results with the obtained parameters and objective functions.

Description	**Symbol**	**Value**
Objective function elastic domain [-]	ϵ_{fit}^{el}	$2.255 \cdot 10^{-2}$
Objective function elasto-plastic domain [-]	ϵ_{fit}^{pl}	$8.010 \cdot 10^{-3}$
Isotropic Young's modulus [MPa]	E	$3.542 \cdot 10^{3}$
Isotropic Poisson's ratio [-]	ν	$3.376 \cdot 10^{-2}$
Transversal isotropy elastic factor [-]	k	$2.434 \cdot 10^{0}$
Transverse yield stress [N/mm²]	σ_y	$6.461 \cdot 10^{1}$
Transversal isotropy yield ratio [-]	R	$1.626 \cdot 10^{1}$
Polynomial hardening parameters [-]	κ_1	$3.783 \cdot 10^{1}$
	κ_2	$1.470 \cdot 10^{3}$
	κ_3	$2.832 \cdot 10^{1}$

4.4 Elasto-plastic Orientation Averaging with fibre length distributions

With the surrogate material model calibrated on the UC simulations, the Orientation Averaging process for the elasto-plastic material behaviour can be started. The process is adapted to be applied on a uniaxial stress case. A global strain increment in load direction is applied stepwise up to a certain maximum global strain. For each strain increment, the following procedure is applied:

First, the full global strain increment $\Delta\boldsymbol{\varepsilon}$ is estimated using the method described in Chapter 2.1.4. For that, the composite tangent stiffness is needed. It is derived from the homogenised tangent stiffness, computed in the previous strain step. Considering the first time-step, the initial linear elastic composite stiffness is used for the prediction. It should be mentioned that for an appropriate model accuracy, only small strain steps should be applied. With the global composite strain increment, the local UC strain increment $\Delta\boldsymbol{\varepsilon}_{UC}$ can be obtained using the corresponding interaction assumption. The definitions of the local UC strain increment based on the Voigt, Reuss and self-consistent assumptions are given in the following equations:

$$\Delta\boldsymbol{\varepsilon}_{UC}^{V}(l_F, \boldsymbol{p}) = \boldsymbol{R}(\boldsymbol{p}) \cdot \boldsymbol{\varepsilon}_C \cdot \boldsymbol{R}^T(\boldsymbol{p}) = \left[\boldsymbol{R}(\boldsymbol{p}) \overline{\otimes} \boldsymbol{R}(\boldsymbol{p})\right] : \boldsymbol{\varepsilon}_C, \tag{4.11}$$

$$\Delta\boldsymbol{\varepsilon}_{UC}^{R}(l_F, \boldsymbol{p}) = \left[\,{}^4\boldsymbol{C}_{UC}^{tang}(l_F, \boldsymbol{p})\right]^{-1} : \left[\left[\boldsymbol{R}(\boldsymbol{p}) \overline{\otimes} \boldsymbol{R}(\boldsymbol{p})\right] : \left({}^4\boldsymbol{C}_C^{R,tang} : \Delta\boldsymbol{\varepsilon}_C\right)\right], \tag{4.12}$$

$$\Delta\boldsymbol{\varepsilon}_{UC}^{SC}(l_F, \boldsymbol{p}) = {}^4\boldsymbol{A}^{tang} : \Delta\boldsymbol{\varepsilon}_{\mathrm{C}}, \tag{4.13}$$

$${}^4\boldsymbol{A}^{tang} = \left[\,{}^4\boldsymbol{I} + {}^4\boldsymbol{E} : \left(\left[\,{}^4\boldsymbol{C}_C^{tang}\right]^{-1} : {}^4\boldsymbol{C}_{UC}^{glob,tang}(l_F, \boldsymbol{p}) - {}^4\boldsymbol{I}\right)\right]^{-1}. \tag{4.14}$$

With the local strain increment, and the previous stress and strain state, the surrogate model is used to obtain the corresponding local UC stress state. The local strains and stresses of all orientations and fibre lengths are then averaged with the following relations to obtain the global composite constitution:

$$\boldsymbol{\varepsilon}_C = \sum_{\boldsymbol{i}}^{n_{\boldsymbol{len}}} w_i(l_F) \sum_{\boldsymbol{j}}^{n_{\boldsymbol{ori}}} \psi_j(\boldsymbol{p}_j, l_F)\, \boldsymbol{R}^T(\boldsymbol{p}_j) \cdot \boldsymbol{\varepsilon}_{UC}(l_{F,i}, \boldsymbol{p}_j) \cdot \boldsymbol{R}(\boldsymbol{p}_j), \tag{4.15}$$

$$\boldsymbol{\sigma}_C = \sum_{\boldsymbol{i}}^{n_{\boldsymbol{len}}} w_i(l_F) \sum_{\boldsymbol{j}}^{n_{\boldsymbol{ori}}} \psi_j(\boldsymbol{p}_j, l_F)\, \boldsymbol{R}^T(\boldsymbol{p}_j) \cdot \boldsymbol{\sigma}_{UC}(l_{F,i}, \boldsymbol{p}_j) \cdot \boldsymbol{R}(\boldsymbol{p}_j). \tag{4.16}$$

Besides the local stress and strain tensor, the method of the surrogate model also computes the local UC tangent stiffness tensors for the current state. These are used in the following step, to obtain the composite stiffness in analogy to the linear elastic Orientation Averaging method, presented in Chapter 4.2. In case of the Voigt and Reuss assumptions, this process can be incorporated into the iteration through the fibre lengths and orientations. For the self-consistent assumption, however, due to its additional iterative process, a separate Orientation Averaging process is implemented for obtaining the global tangent stiffness tensor. Figure 4.8 shows a simplified visualisation of the Orientation Averaging process for elasto-plastic material behaviour for the Voigt and Reuss assumption.

The nested structure of the presented material model indicates the high computational effort needed for the calculations. To ensure an efficient computation, many factors have to be considered in the realisation of the methods. With the presented methods, many state variables need to be stored. The local stresses and strains as well as the effective plastic strain from the previous step for all inclusions are needed for the prediction of the next strain increment. In case of the Reuss assumption the tangent stiffnesses of all inclusions are necessary to obtain the local strain increment. For the self-consistent interaction assumption even the stiffness tensor in the global coordinate system must be stored. This information is needed for all fibre lengths and all orientations considered in the Orientation Averaging process, resulting in a data point number of each $n_{len} \cdot n_{ori}$. Besides that, for each time increment, the resulting global stress and

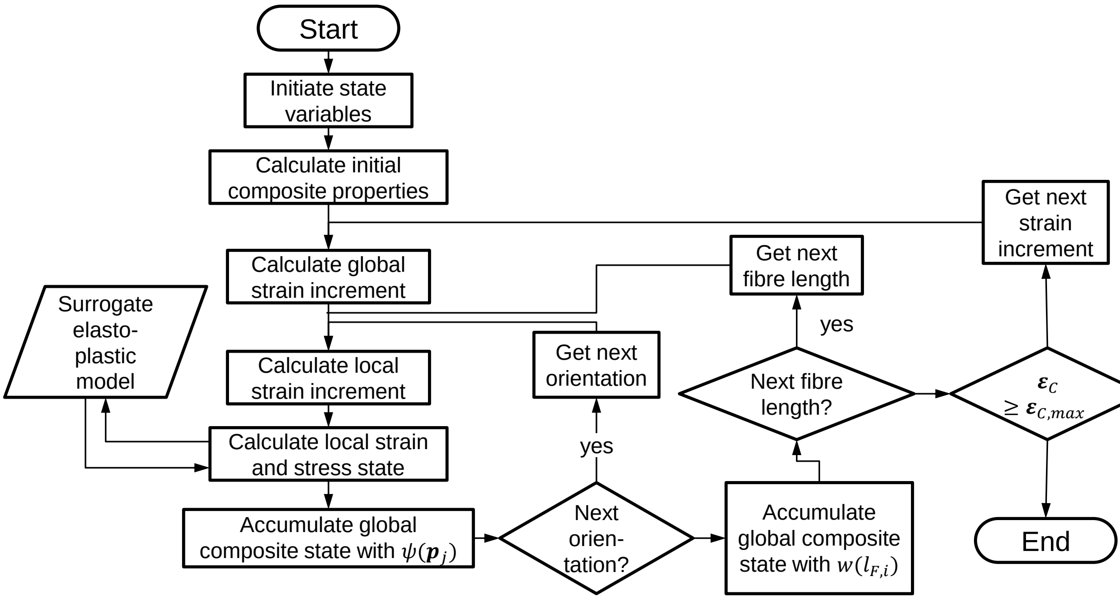

Figure 4.8: Principal algorithm workflow for the elasto-plastic two-step Orientation Averaging algorithm.

strain tensor and the global homogenised tangent stiffness tensor is saved. The large amount of data stored can slow down the Orientation Averaging process in addition to the considerable number of loops and iterations in the procedure.

The computational time for an Orientation Averaging process with a single representative fibre length and a 3D-random FOD, represented by an icosphere with 4 refinement steps, using the Voigt assumption is measured with 21 minutes. In comparison, the counterpart, considering 12 fibre length classes, takes 174 minutes. 200 strain increments are computed for each method going up to a maximum global strain of 0.05 in load direction. The UC finite element simulations and material model fitting are not included in these measurements. The computations are performed on a personal laptop with an Intel Core i7-3632QM Quad-Core processor and 16 GB of random access memory. This shows that a reduction of the FLD to a single representative fibre length would lead to a major improvement of the computational performance of the model.

5 MODEL PREDICTIONS AND COMPARISON TO LITERATURE RESULTS

In the following chapters, the presented models are applied on examples taken from the literature. It is investigated to which extent the models can represent the material behaviour in the linear elastic and elasto-plastic domain. For both methods, it is investigated if the representation of a FLD with a single representative fibre length is applicable and produces reasonable results and which averaging method is suited best for representing the FLD in the two-step Orientation Averaging method.

First, the linear elastic model is tested in the following chapter. After that, the elasto-plastic model is investigated. Subsequently, fibre matrix debonding is included into the elasto-plastic UC-simulations and the surrogate material model is calibrated on the obtained behaviour. With this at hand, the capability of representing the debonding with the present model is investigated.

5.1 Linear elastic model

In this chapter, the linear elastic material behaviour is investigated. For that, two dissimilar materials are considered, taken from the literature. The model predictions including the FLD-averaging are compared to the literature results. After that, it is investigated if the FLD can be replaced by a single representative fibre length.

5.1.1 Glass fibre reinforced Polybutylene Terephthalate composite

As a first example, a glass fibre reinforced Polybutylene Terephthalate (PBT) composite (Celanex 2300 GV1/20 by Celanese Corporation [15]) with a fibre mass content of 20 %wt. is taken from *Breuer, Stommel et al.* [9]. Note that the fibre length distribution of this composite is already mentioned in Chapter 3.2 as an example for a fibre length distribution, which is not representable with an analytical *Weibull* distribution function.

Breuer, Stommel et al. investigate the effect of including fibre length and fibre orientation distributions into the micro-mechanical modelling by performing numerical simulations on different RVE-structures. The statistical inaccuracies from the RVE modelling are counteracted by performing Monte-Carlo simulations for each model. The simulation results are used here as a reference for the prediction accuracy of the two-step Orientation Averaging process including fibre length distributions. First, the FLD-averaging method is tested, by comparing the model predictions of a unidirectional composite to the volumetric homogenisation results of a UD-RVE. The predictions are then compared to the UC-simulations with the averaged fibre lengths to evaluate the prediction accuracies of the method using a single representative fibre length. In a second step, the FOD is introduced, to investigate the impact of the orientation distribution on the resulting homogenised properties. [9]

In the paper, by *Breuer, Stommel et al.*, isotropic material properties are presented for the fibre and matrix, which are displayed in Table 5.1. Note that the matrix Poisson's ratio is not mentioned in the paper. For that reason, a standard value for the PBT matrix of ν_M = 0.4 is assumed. The value is marked with an asterisk in the table. In the paper, the authors also present three different temperature dependent matrix stiffnesses. However, the results for the model predictions are not documented as well as for the mentioned set of parameters. Hence, only this set of parameters is investigated in this work.

Table 5.1: Material properties of the constituents in the glass fibre reinforced PBT composite [9].

Property	**Symbol**	**Value**	**Unit**
Matrix Young's modulus	E_M	2,000	MPa
Matrix Poisson's ratio	ν_M	0.4*	-
Fibre Young's modulus	E_F	70,000	MPa
Fibre Poisson's ratio	ν_F	0.22	-
Mean fibre diameter	d_F	11.4	µm
Fibre volume fraction	φ	11.6	%
Fibre orientation distribution	a_{11}	0.711	–
	a_{22}	0.244	–
	a_{33}	0.045	–

A diagonal FODT with eigenvalues $\lambda_1 = 0.711$, $\lambda_2 = 0.244$ and $\lambda_3 = 0.045$ is considered. The resulting FODF, using a Bingham distribution function, is visualised in Figure 5.1, together with the fîbre length distribution.

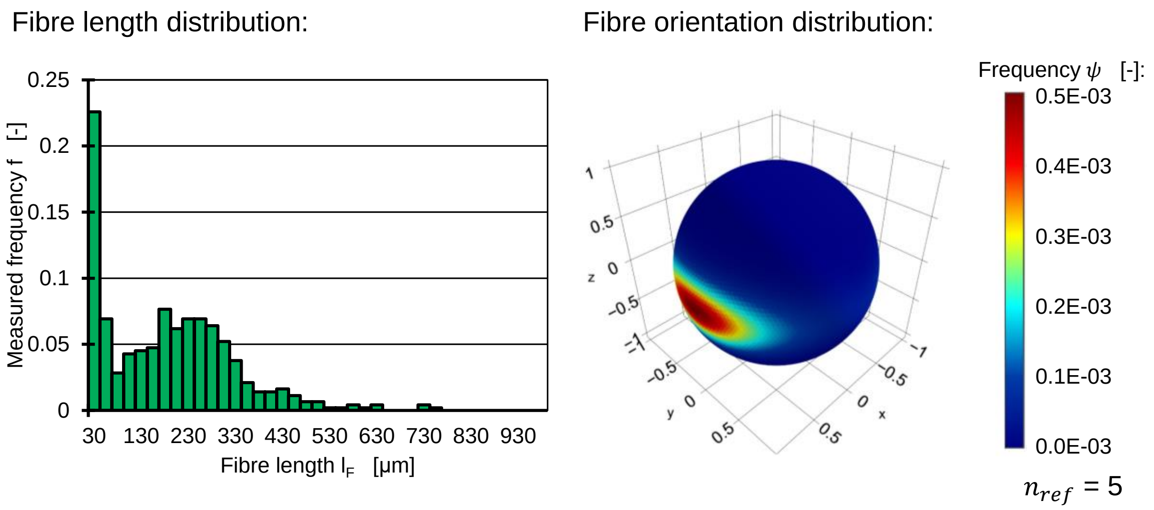

Figure 5.1Fibre length distribution and fibre orientation distribution of glass fibre reinforced PBT from Breuer and Stommel [9].

First, the unidirectional RVE simulations are used to investigate the prediction capability of the fibre length averaging model in an isolated environment, without considering FODs. According to this, the Orientation Averaging is conducted for a single fibre orientation in 1-direction. In addition to the simulation results from the paper, three equivalent UD-RVE simulations are conducted, in order to obtain the transverse composite behaviour, which is not metioned in the paper. All three interaction assumptions are used for this example.

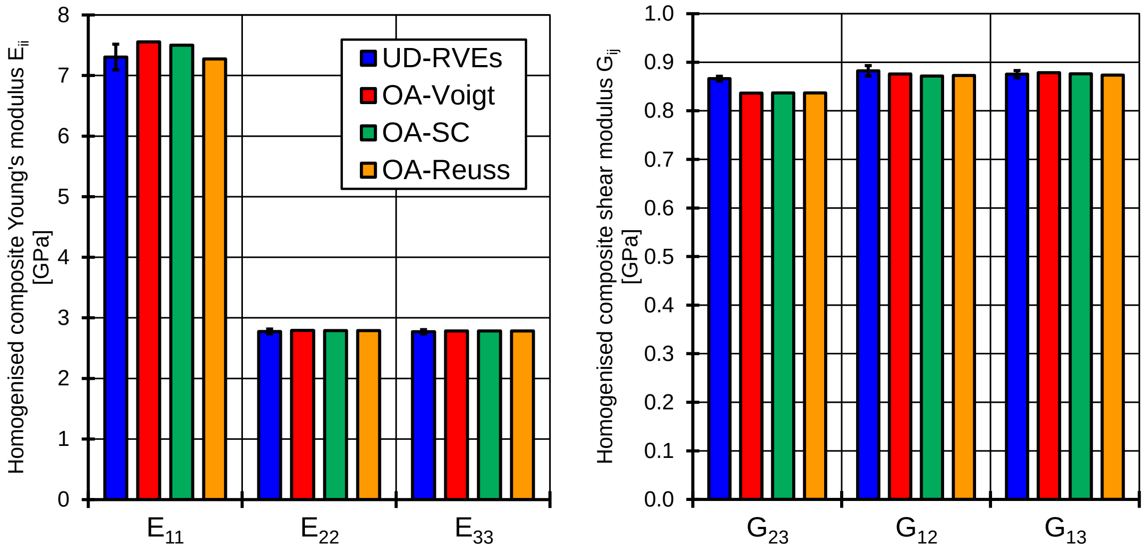

Figure 5.2: OA-model predictions for a unidirectional composite with FLD in comparison to UD-RVE simulations.

Figure 5.2 shows a comparison between the obtained Young's and shear moduli, obtained from the OA-prediction in comparison to the results from the UD-RVE simulations. The obtained homogenised composite Young's moduli in 11-direction show a good agreement with the values obtained from UD-RVE-simulations from the literature being 7,600 MPa [9]. Comparing the resulting Young's and shear moduli from the OA-process with the UD-RVE simulations, they are very closely matched. In comparison to the average UD-RVE-properties the maximum relative error is obtained for the Young's modulus in 11-direction with 3.4 %. The other larger deviation from the UD-RVE predictions can be found in the shear modulus G_{23}. Here, all OA-predictions result in a lower value with a deviation from the average UD-RVE prediction of -3.4 %. However, this can still be considered as a very good fit between the presented models. The obtained stiffness values are lised in Table 5.2. The percentages in brackets behind the OA-predictions represent the relative error of the respective value in comparison to the UD-RVE prediction.

Table 5.2: Comparison of Orientation Averaging predictions including FLD and RVE prediction on a unidirectional composite [9].

Model	**Literature [9]**	**UD-RVE**	**OA-Voigt**	**OA-SC**	**OA-Reuss**
E_{11} $[MPa]$	7,600	7,306	7,591 (3.4 %)	7,500 (2.7 %)	7,273 (-0.4 %)
E_{22} $[MPa]$	-	2,760	2,792 (0.6 %)	2,790 (0.5%)	2,790 (0.5 %)
E_{33} $[MPa]$	-	2,770	2,785 (0.5 %)	2,783 (0.5 %)	2,783 (0.5 %)
G_{23} $[MPa]$	-	866	837 (-3.4 %)	837 (-3.4 %)	837 (-3.4 %)
G_{12} $[MPa]$	-	882	876 (-0.7 %)	872 (-1.2 %)	873 (-1.1 %)
G_{13} $[MPa]$	-	876	879 (0.3 %)	877 (0.1 %)	874 (-0.2 %)

It can be observed additionally that for the unidirectional case presented here, the different interaction assumptions for the Orientation Averaging process with fibre length averaging produce very similar values. However, in terms of the composite stiffness in 11-direction, the Voigt and self-consistent assumptions result in higher values. In comparison to the UD-RVE simulation results form *Breuer, Stommel et al.*, those are the best predictions in the uniaxial case.

Figure 5.3 presents the homogenised stiffnesses from the UD-RVE simulations compared to those from Unit Cell simulations with the three differently obtained representative fibre lengths. The three lengths are given with the number-averaged fibre length l_F^{num} = 187 µm, the volume-averaged fibre length l_F^{vol} = 289 µm and the stiffness-averaged fibre length l_F^{stiff} = 223 µm.

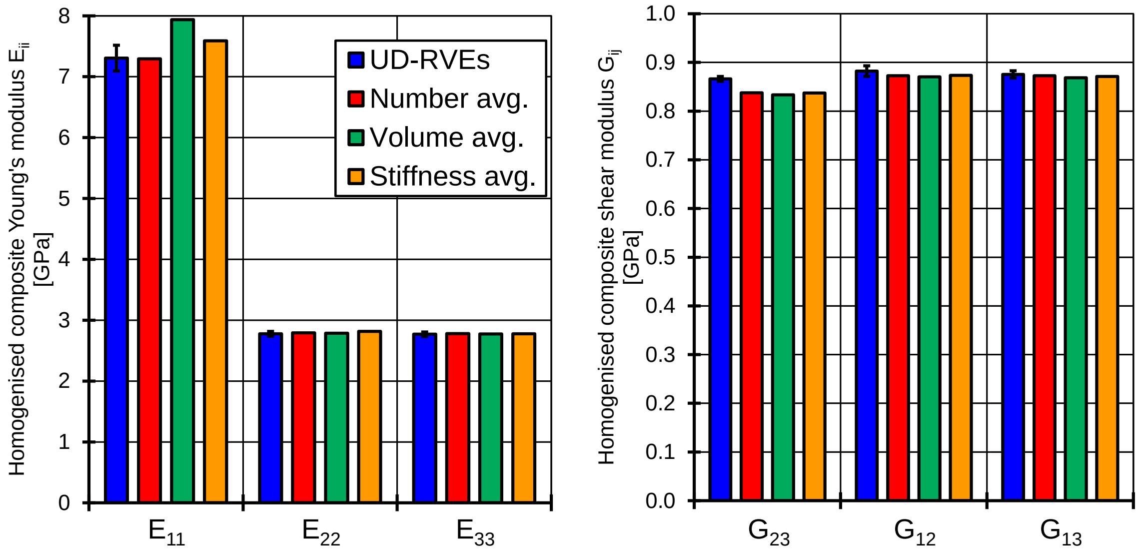

Figure 5.3: UC-simulations with single representative fibre lengths in comparison to UD-RVE simulations with included FLD.

The UC-simulations produce very similar results, especially for the transverse Young's and the shear moduli. This is expected from the observations made, on the length dependent material behaviour in Chapter 3.1. The homogenised Young's moduli in fibre direction show small differences, with the number-averaged fibre length producing the closest result to the average UD-RVE prediction with 7,293 MPa. With a slightly higher homogenised stiffness of 7,590 MPa, the stiffness-averaged fibre length takes on an intermediate value between the number-averaged fibre length and the volume-averaged fibre length, with 7,938 MPa. The latter exceeds the prediction made from the UD-RVE predictions as well as the Orientation Averaging predictions from Table 5.2. In comparison to the OA-predictions with fibre length averaging, the UC-simulations with number- and the stiffness-averaged fibre lengths produce nearly exactly the same homogenised Young's moduli than the OA-method using Reuss and Voigt assumptions, respectively. The derivation of the stiffness-averaged fibre length is derived from the fibre length average unidirectional composite stiffness. This explains why these two predictions are so close to each other.

In the next step, the FOD is introduced to the simulations. As mentioned before, a diagonal FODT $\mathbf{a} = diag(0.711, 0.244, 0.045)$ is proposed by *Breuer, Stommel et al.* [9]. However, the predicted composite stiffness of E_{11} = 6,450 MPa does not comply with this FODT, as such a FOD is expected to result in a much lower homogenised composite stiffness. A RVE simulation is conducted in the here presented study using equivalent paramters.The resulting homogenised composite stiffness of 4,975 MPa is significantly lower, than this, obtained by *Breuer, Stommel et al. [9]*. It should be noted that due to high computational costs and difficulties in creating the geometry of the RVE-structure, only one appropriate simulation could be conducted in this case. Additionally, the OA-simulations show similar results to the conducted RVE-simulation. Therefore, it is decided to compare the OA-results with FLD and with representative fibre lengths to the conducted RVE-simulation. With the additional randomised factor coming from the FOD, the resulting homogenised stiffnesses are likely to be spread more widely than the results from the UD-RVE-simulations. Hence, the OA-simualtion results can only be evaluated qualitatively in comparison to this single simulation.

Figure 5.4 shows the corresponding homogenised Young's and shear moduli obtained from the RVE-simulation in comparison to the OA-simulation results considering the FLD. The resulting

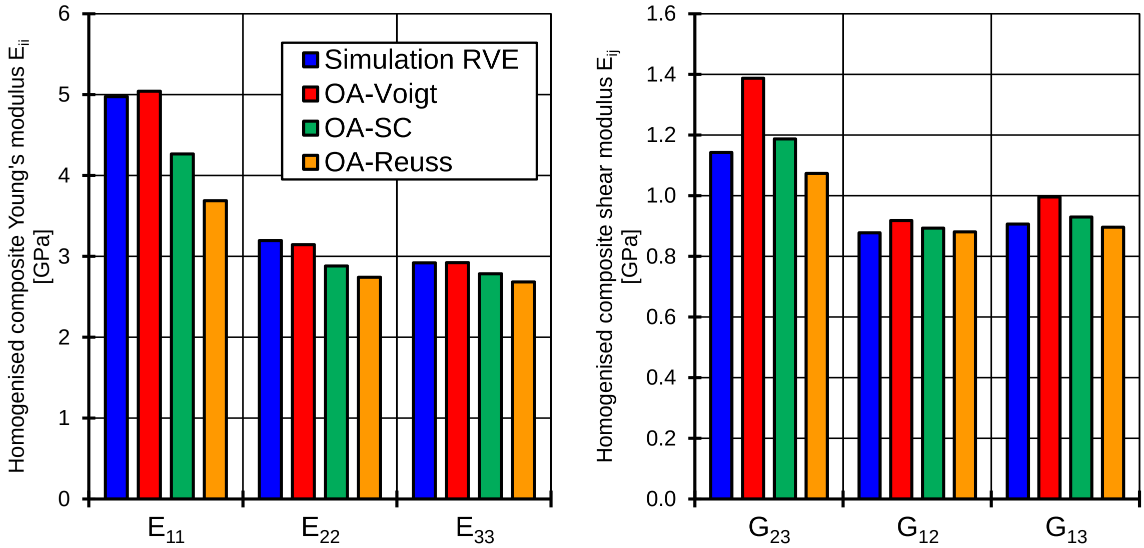

Figure 5.4: OA-model predictions considering the FOD and FLD in comparison to RVE simulations with FOD and FLD.

values are in a similar range compared to each other. In 1-direction, the OA-approach using Voigt assumption gives the highest prediction for the homogenised Young's modulus with 4,984 MPa. It matches very closely with the homogenised Young's modulus from the RVE simulation. The Reuss assumption produces the lowest estimate for the Young's modulus in all directions. The intermediate self-consistent approach produces predictions in between the other two OA-predictions. Also for the shear moduli, the OA-method using FLD gives a good approximation of the homogenised composite properties in comparison to the RVE-simulation. All homogenised moduli are summarised in Table 5.3.

The agreement of the OA-predictions with the RVE-simulations, both in the unidirectional case and the case considering the orientation distribution, shows that the extended two-step Orientation Averaging method considering fibre length distributions gives good predictions of the homogenised composite material behaviour. Based on this, in the following step, the OA-predictions with FLD are now quantitatively compared with the OA-predictions using the representative fibre lengths.

Table 5.3: Comparison of Orientation Averaging predictions including FLD and RVE prediction considering the fibre orientation distribution [9].

Model	**Literature [9]**	**UD-RVE**	**OA-Voigt**	**OA-SC**	**OA-Reuss**
E_{11} $[MPa]$	6,450	4,975.0	5,042.8	4,266.2	3,689.7
E_{22} $[MPa]$	-	3,194.4	3,145.2	2,882.0	2,741.8
E_{33} $[MPa]$	-	2,919.5	2,922.5	2,784.2	2,684.7
G_{23} $[MPa]$	-	1,142.5	1,387.1	1,187.5	1,073.7
G_{12} $[MPa]$	-	877.9	918.4	893.2	881.2
G_{13} $[MPa]$	-	906.3	995.8	929.9	895.9

Figure 5.5 presents the resulting Young's moduli predictions for different representative fibre lengths and different interaction assumptions. The predictions are normalised to the OA-result

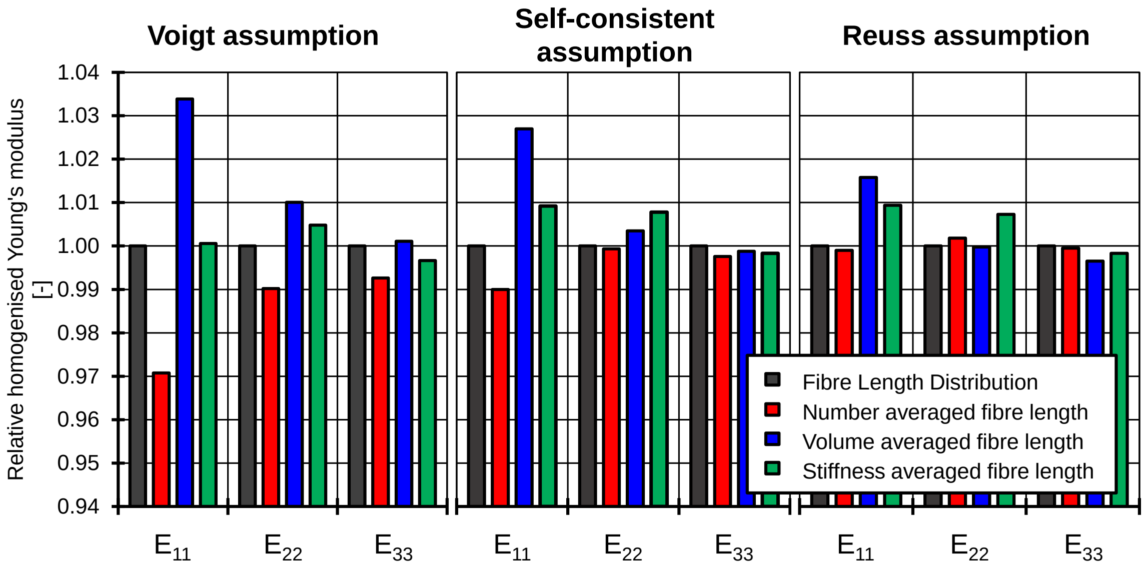

Figure 5.5: Young's moduli of OA-predictions with single fibre lengths normalised to the corresponding OA- prediction with fibre length averaging.

considering the FLD with the respective interaction assumption. With that, it can be observed that the representative fibre lengths give very good predictions in comparison to the method using the FLD. Especially in the transverse directions 2 and 3, all Orientation Averaging methods show very similar results, varying with a maximum error of less then 1 % for all interaction assumptions. The predictions in 1-direction deviate much more from the reference. In case of the Voigt assumption, the stiffness-averaged fibre length gives the best prediction compared to the reference with an error of 0.05 %. The number- and the volume-averaged fibre lengths each over- or underestimate the reference with 3.0 % and 3.3 % error, respectively. In case of the self-consistent interaction assumption, a similar picture occurs for the relative stiffness in 1-direction. Here, the number- and stiffness-averaged fibre length predictions are equally close to the reference prediction, with the number-averaged fibre length undepredicting and the stiffness-averaged fibre length overpredicting the FLD-prediction with 1 % error. The volume-averaged fibre length prediction exceeds the reference by 2.7 %. In case of the Reuss assumption in 1-direction, the number-averaged fibre length prediction is closest to the reference with an error of 0.1 %. The error values for the stiffness-averaged and volume-averaged fibre lengths result in 0.9 % and 1.5 %, respectively. The absolute values for predicted homogenised Young's moduli are presented in Table 5.4.

Table 5.4: Comparison of Orientation Averaging predictions with representative fibre lengths and considering the FLD.

Model	**OA-Voigt**			**OA-SC**			**OA-Reuss**		
Direction	E_{11}	E_{22}	E_{33}	E_{11}	E_{22}	E_{33}	E_{11}	E_{22}	E_{33}
Unit	[MPa]			[MPa]			[MPa]		
Fibre Length Distribution	5,043	3,145	2,923	4,266	2,882	2,784	3,690	2,742	2,685
Number-averaged length	4,895	3,114	2,901	4,223	2,880	2,778	3,686	2,747	2,683
Volume-averaged length	5,214	3,177	2,926	4,381	2,892	2,781	3,748	2,741	2,675
Stiffness-averaged length	5,046	3,160	2,913	4,305	2,904	2,780	3,724	2,762	2,680

To summarise the presented results in this subsection, a good agreement between Orientation Averaging and unidirectional RVEs is found. The UC-simulations with representative fibre lengths show good results in comparison with the UD-RVE as well. However, the volume-averaged fibre length is found to overpredict the homogenised composite stiffness in most cases, especially in fibre direction. This is also seen, when fibre orientation distributions are introduced. In the main orientation direction (here the 1-direction), The volume-averaged fibre length exceeds the reference prectictions in all cases. However, the number- and the stiffness-averaged fibre length show very good predictions for all interaction assumptions.

5.1.2 Glass fibre reinforced Polyamide 6

In this chapter the Orientation Averaging predictions are compared to experimental results. The experiments are taken from the literature. *Holmström, Hopperstad et al.* present experimental results for an E-glass fibre reinforced Polyamide composite [27]. In order to make the results accessible and enable further investigation based on their experimental results, the authors published all experimental data in a Mendeley data set [26]. However, the commercial material names are not mentioned in the paper.

Two different materials are investigated with differing fibre weight fractions of 15 %wt and 30 %wt. The different materials are therefore mentionend as PA-GF15 and PA-GF30, respectively. Due to the difference in fibre mass fractions in the two materials, two different FLDs and FODs are obtained from micro-CT scans. The authors present a height dependent FOD in the through thickness direction of the injection moulded plate. It is observed that layers with different FODs develop in the center and the outer parts of the injection moulded part, due to the different flow conditions in these areas. However, this layered structure is neglected in this study and an average FOD is assumed for both composites. This is done by averaging over the thickness dependent FODT given in [26]. For the averaging procedure, the FODT $\boldsymbol{a}_k$ is weighted by the layer thickness t_k of the measurement and the thickness dependent fibre volume fraction φ_k for a corresponding layer k. This results in a definition of an averaged FODT component $\overline{a}_{ij}$ as

$$\overline{a}_{ij} = \frac{\sum_k t_k \cdot \varphi_k \cdot a_{ij,k}}{\sum_k t_k \cdot \varphi_k}. \tag{5.1}$$

PA-GF15 shows an approximately 2D-random fibre orientation distribution with a diagonal FODT resulting in $\overline{\mathbf{a}} = diag(0.503, 0.476, 0.021)$. The higher mass fraction material, PA-GF30, has a resulting FODT of $\overline{\mathbf{a}} = diag(0.588, 0.370, 0.042)$. It shows a slightly higher probability of fibres oriented in the 1-direction, compared to the PA-GF15-material. The fibre length distributions are also different, with the PA-GF15 having a higher averaged fibre length compared to the PA-GF30-material.

In Figure 5.6 and 5.7, the FLDs and FODs of the two materials are presented, respectively. Note

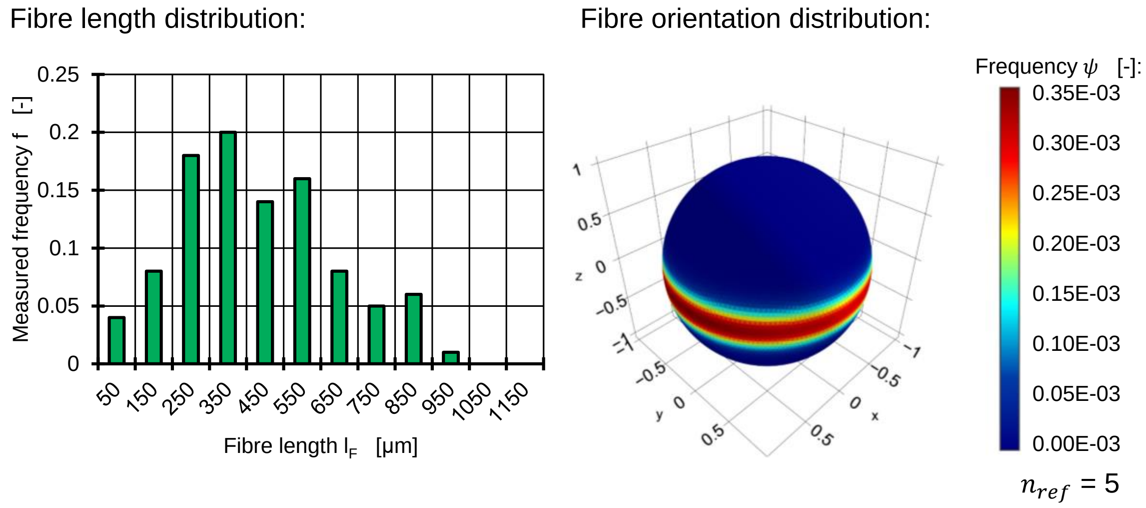

Figure 5.6: Fibre length distribution and fibre orientation distribution of the PA-GF15 composite from Holmström, Hopperstad et al. [27].

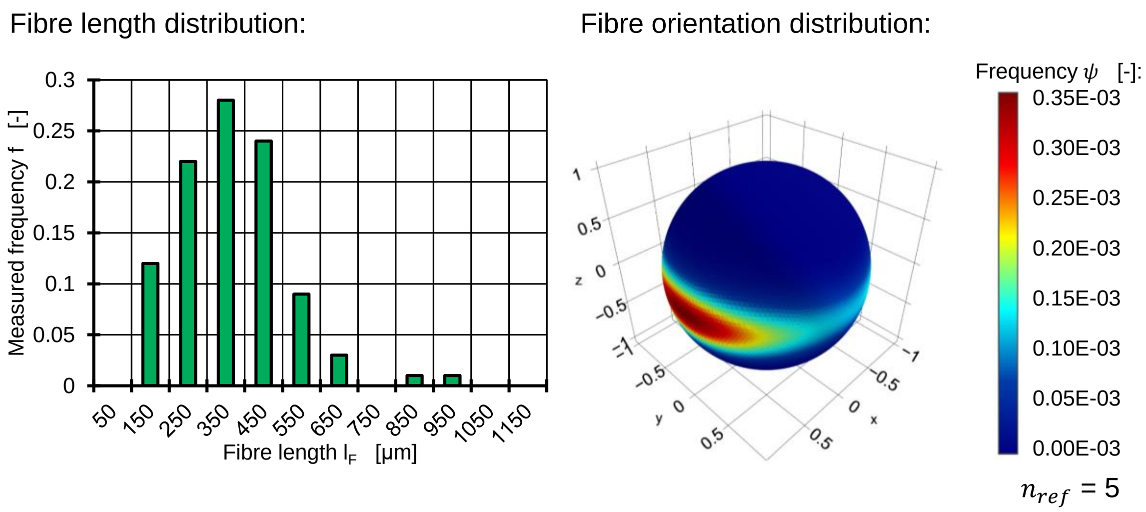

Figure 5.7: Fibre length distribution and fibre orientation distribution of the PA-GF30 composite from Holmström, Hopperstad et al. [27].

that both FLDs can be represented by a *Weibull* distribution, as shown for the PA-GF30 composite in Figure 3.3. From the micro-CT-Scans, additionally, an average fibre diameter is obtained as 13.5 μm for the PA-GF15 and 12.6 μm for the PA-GF30. The remaining material parameters are given in the summary in Table 5.5. Note that the mechanical properties of the glass fibres are not presented in the paper. Therefore, standard values for E-glass fibres are assumed and the values are marked by an asterisk in the table.

Table 5.5: Material properties of the constituents in PA-GF15 and PA-GF30 composites [26] (estimated parameters marked with asterisk).

Property	**Symbol**	**Value**		**Unit**
		PA-GF15	**PA-GF30**	
Matrix Young's modulus	E_M	2,800		MPa
Matrix Poisson's ratio	ν_M	0.4		-
Fibre Young's modulus	E_F	70,000*		MPa
Fibre Poisson's ratio	ν_F	0.2*		-
Mean fibre diameter	d_F	13.5	12.6	μm
Fibre volume fraction	φ	0.064	0.152	%
Fibre orientation distribution	a_{11}	0.503	0.588	–
	a_{22}	0.476	0.370	–
	a_{33}	0.021	0.042	–

The authors present anisotropic material properties for the composite materials. However, the presented Young's modulus in 3-direction is obtained as the average of the two values in the 1 and 2-direction. This is, considering the FOD, not a realistic value and thus the value is not investigated in this work. OA-predictions are first obtained considering the FLD and the agreement with the experimental results is discussed. The results are then compared with the representative fibre length predictions in respect to the correspong interaction assumption.In Figure 5.8, the OA-predictions using the FLD averaging are presented for both weight fractions in terms of the homogenised Young's moduli in directions 1 and 2. It is found that for all interaction assumptions, the Orientation Averaging predictions underestimate the Young's modulus in 1-direction slightly. The prediction in 2-direction, however capture the measured material behaviour very well. The trend of a higher fibre weight fraction and a higher degree of fibre orientation for the PA-GF30 is captured well by the material model. Also, the order of the interaction assumptions is clearly visible, with the self-consistent interaction assumption giving an intermediate approach to the two extreme approaches with the Voigt assumption giving an upper boundary and the Reuss assumption representing a lower boundary. All in all, despite the slight deviation of the prediction in the 1-direction, the OA-predictions using FLD can be considered as a good fit to the testing results.

In the next step, OA-predictions from the representative fibre lengths are compared against the OA-predictions using fibre length distributions. For this, both materials are investigated seperately. The representative fibre lengths for the PA-GF15 are given with the number-averaged fibre length l_F^{num} = 430 μm, the volume-averaged fibre length l_F^{vol} = 532 μm and the

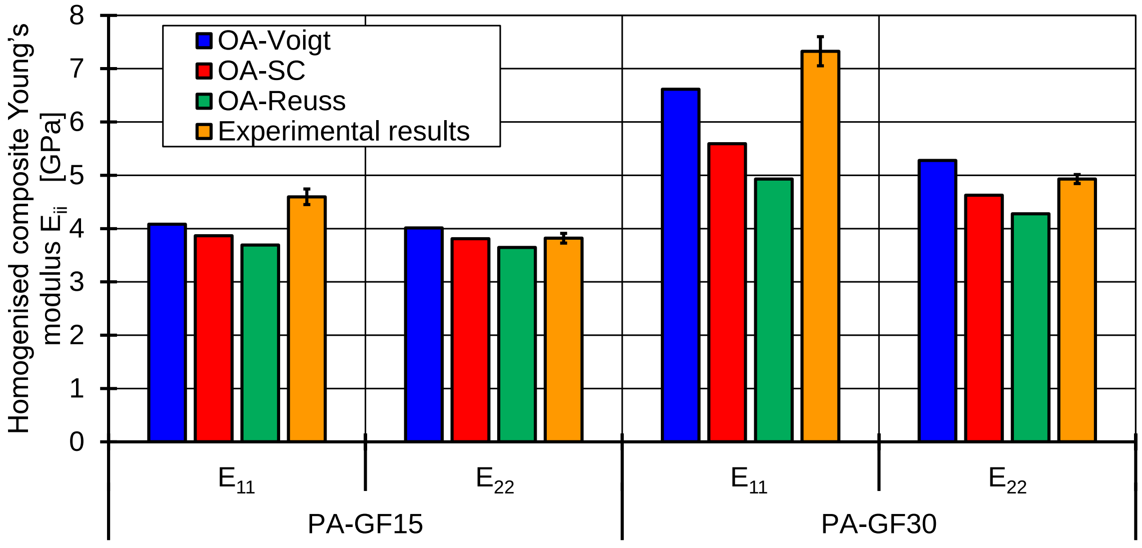

Figure 5.8: Comparison of the OA-prediction using fibre length averaging and experimental results for PA-GF15 and PA-GF30 [27].

stiffness-averaged fibre length l_F^{stiff} = 443 µm. With the averaged fibre lengths being so closely matched, the resulting homogenised fibre parallel UC Young's moduli are very similar as well with 6,116 MPa for the number-averaged fibre length, 6,133 MPa for the stiffness-averaged fibre length and 6,158 MPa for the volume-averaged fibre length.

Figure 5.9 shows the comparison of the OA-predictions of all represetative fibre lengths with the different interaction assumption. In analogy to the comparison in the previous chapter, the

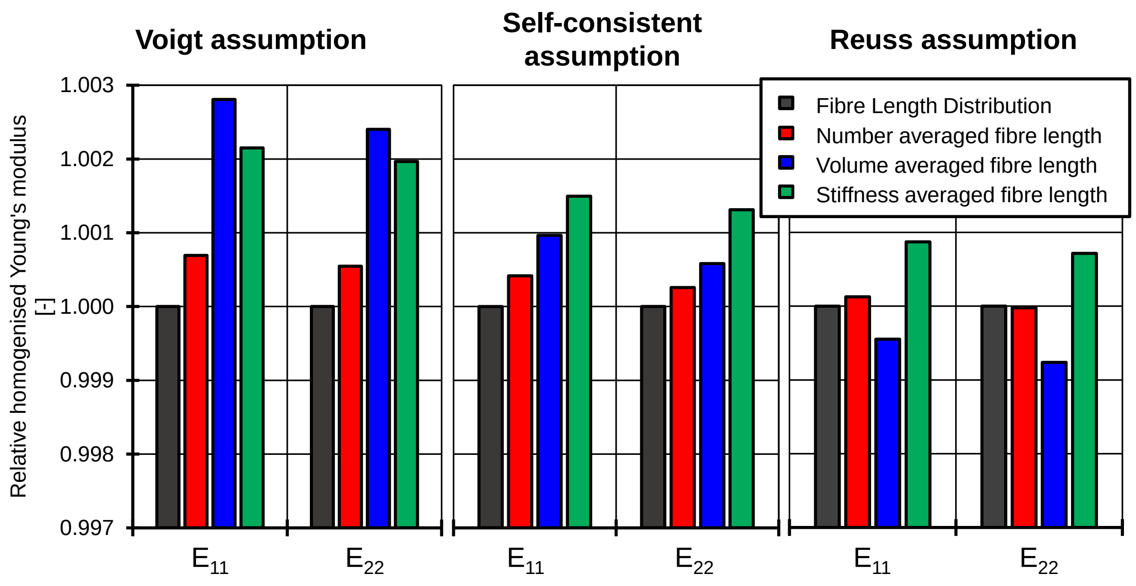

Figure 5.9: Young's moduli of OA-predictions with representative fibre lengths normalised to the corresponding OA-prediction using fibre length averaging for PA-GF15.

predicted Young's moduli are normalised with their respective counterpart from the OA-process cosidering FLDs. It can be observed that the predictions with representative fibre length match the FLD considering predictions very good. The maximum overall error is smaller than 0.25 % compared to the corresponding OA-prediction considering the FLD. The highest deviations from the reference prediction occur for the Voigt assumption, where all representative fibre lengths overpredict the OA-prediction with FLD. Here, the number-averaged fibre length gives the closest prediction to the reference for all interaction assumptions. However, due to the little overall error, all three representative fibre lengths are considered as very good fits to the FLD. The resulting Young's moduli for the three representative fibre lengths and the OA-procedure considering the FLD are summarised in Table 5.6.

Table 5.6: Comparison of Orientation Averaging predictions with representative fibre lengths and considering the FLD for the PA-GF15 composite.

Model	**OA-Voigt**		**OA-SC**		**OA-Reuss**	
Direction	E_{11}	E_{22}	E_{11}	E_{22}	E_{11}	E_{22}
Unit	[MPa]		[MPa]		[MPa]	
Fibre Length Distribution	4,080	4,013	3,864	3,808	3,690	3,644
Number-averaged fibre length	4,082	4,015	3,866	3,809	3,691	3,644
Volume-averaged fibre length	4,091	4,023	3,869	3,810	3,689	3,641
Stiffness-averaged fibre length	4,088	4,021	3,871	3,813	3,694	3,647

In Figure 5.10, the analogue graphs are shown for the PA-GF30 composite. The representative fibre lengths in this case are shorter than for the lower fibre weight fraction material, due to a greater chance of fibre breakage during the processing. The number-averaged fibre length results in l_F^{num} = 366 µm, the volume-averaged fibre length l_F^{vol} = 425 µm and the stiffness-averaged fibre length l_F^{stiff} = 373 µm. These fibre lengths are very closely matched already, which results in the fibre parallel, homogenised UC Young's moduli of 10,974 MPa for the number-averaged fibre length, 11,000 MPa for the stiffness-averaged fibre length and 11,129 MPa for the volume-averaged fibre length.

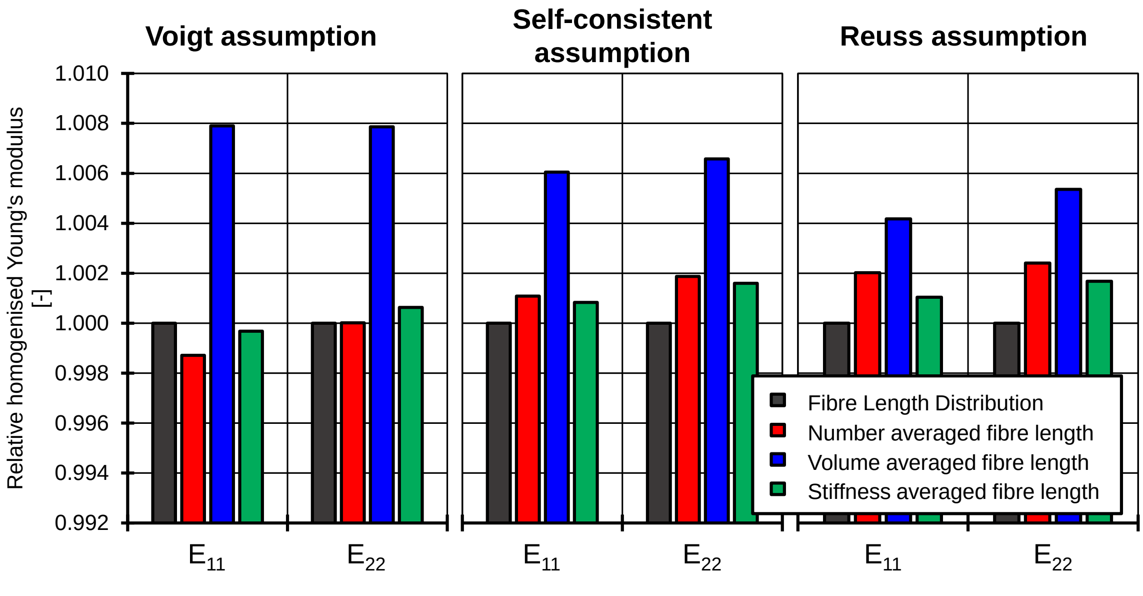

Figure 5.10: Young's moduli of OA-predictions with representative fibre lengths normalised to the corresponding OA-prediction using fibre length averaging for PA-GF30.

As a result, the OA-predictions for the representative fibre lengths are also very close to each other. However, in comparison to the OA-predictions using the FLD, the volume-averaged single fibre length predictions seem to overestimate the homogenised composite stiffness, especially for the Voigt assumption. The predictions made with the number- and stiffness-averaged fibre length give much closer approximations of the reference, with relative errors in the range of 0.25 %. In most cases, the closest prediction is given by the volume-averaged fibre length. However the difference between the two fibre lengths is not large. The fit of the OA-predictions using single representative fibre lengths, to the OA-predictions taking into account the FLD can be considered as good. However, the larger deviations for the volume-averaged fibre length indicate that this averaging method is likely to overpredict the homogenised composite stiffness. Table 5.7 sumarises all presented data with the corresponding Young's moduli for the PA-GF30 material.

Table 5.7: Comparison of Orientation Averaging predictions with representative fibre lengths and considering the FLD for the PA-GF30 composite.

Model	**OA-Voigt**		**OA-SC**		**OA-Reuss**	
Direction	E_{11}	E_{22}	E_{11}	E_{22}	E_{11}	E_{22}
Unit	[MPa]		[MPa]		[MPa]	
Fibre Length Distribution	6,516	5,226	5,547	4,607	4,910	4,268
Number-averaged fibre length	6,508	5,226	5,553	4,615	4,920	4,279
Volume-averaged fibre length	6,568	5,267	5,580	4,637	4,931	4,291
Stiffness-averaged fibre length	6,514	5,230	5,551	4,614	4,915	4,276

In conclusion, for this chapter, it can be said that the OA-method using FLDs produces reasonable results compared to literature data. In comparison to this, the model using representative fibre lengths also produces comparable results. In terms of prediction accuracy, no particular fibre length average could be found which represents the FLD with the most accurate prediction. However, the volume-averaged fibre length usually overpredicts the composite stiffness in comparison to the reference estimations. This leads to the conclusion, that the other two representative fibre lengths, namely the number and the stiffness averaged fibre length, are preferred. Comparing the two investigated methods of representing the FLD, the difference in the composite stiffness predictions is not significant. Hence, considering the computational benefit of using a single representative fibre length for the OA-process, this method is superior, compared to the FLD-averaging method.

5.2 Elasto-plastic matrix behaviour

With the linear elastic model discussed in the previous chapter, in this part, the elasto-plastic behaviour of some SFRCs is modelled. For this, first, the homogenised, unidirectional elasto-plastic material behaviour is obtained and quantified for the UC-simulations. Subsequently the fitting of the surrogate elasto-plastic material model is carried out. And finally, the resulting

OA-predictions are compared to experimental results for both the model using the FLD information and the models using representative fibre lengths.

5.2.1 Glass fibre reinforced Polyamide-6

First, the same material as presented in Chapter 5.1.2 is investigated. *Holmström, Hopperstad et al.* present stress strain curves for both considered materials [27].

5.2.1.1 Material parameters and model calibration

To investigate the pure matrix behaviour, the authors also conducted experiments on pure PA 6 specimens. The resulting stress-strain curves for these tests and are combined in a running average curve in Figure 5.11. Note that the presented stresses and strains in this particular graph

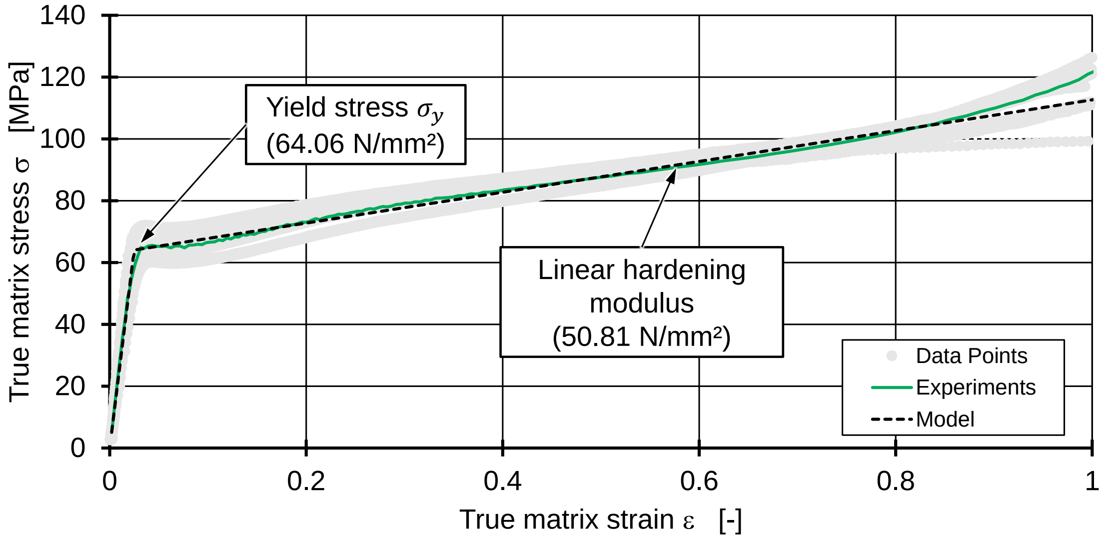

Figure 5.11: Stress-strain response of a PA-6 matrix in comparison to elasto-plastic model with linear hardening [27].

are true values based on finite strain theory. An elasto-plastic model with linear hardening is calibrated on the observed behaviour. It is marked in the figure with the dashed line. Comparing the calibrated model to the running average behaviour, a very good fit is found up to a logarithmic strain value of 0.8. The identified elasto-plastic parameters are given with the Yield stress σ_y = 64.06 N/mm² and the linear hardening modulus H = 50.81 N/mm². It should be emphasised again that the presented OA-model is defined for small strain theory. Therefore, only significantly smaller global strain levels will be investigated. It is, however, necessary to define the matrix' mechanical behaviour for higher strain levels, since in the numerical simulations much higher local strains could occur. Especially in singularities around the cylinder edge, those high strains are likely.

With the linear elastic material properties given in Table 5.5, all necessary information for conducting the UC-simulations is obtained. Subsequently to the simulations, the surrogate model is calibrated on the stress-strain-response of the UC-simulations. The resulting objective function values for the surrogate model calibration for the fibre length classes for the elastic and the elasto-plastic fitting routine are represented in Table 5.8.

Table 5.8: Fitting results of the surrogate material model to the homogenised UC-simulation results for the fibre length classes.

Material	**PA-GF15**		**PA-GF30**	
Fibre length	elastic objective function	elasto-plastic objective function	elastic objective function	elasto-plastic objective function
[μm]	[-]		[-]	
50	$3.264 \cdot 10^{-2}$	$3.845 \cdot 10^{-2}$	$9.161 \cdot 10^{-3}$	$6.879 \cdot 10^{-3}$
150	$3.748 \cdot 10^{-2}$	$2.735 \cdot 10^{-2}$	$4.807 \cdot 10^{-3}$	$6.603 \cdot 10^{-3}$
250	$2.420 \cdot 10^{-2}$	$1.834 \cdot 10^{-2}$	$3.306 \cdot 10^{-3}$	$6.891 \cdot 10^{-3}$
350	$1.657 \cdot 10^{-2}$	$9.410 \cdot 10^{-3}$	$2.541 \cdot 10^{-3}$	$7.606 \cdot 10^{-3}$
450	$1.186 \cdot 10^{-2}$	$6.227 \cdot 10^{-3}$	$2.198 \cdot 10^{-3}$	$8.152 \cdot 10^{-3}$
550	$8.787 \cdot 10^{-3}$	$5.382 \cdot 10^{-3}$	$2.238 \cdot 10^{-3}$	$8.867 \cdot 10^{-3}$
650	$6.659 \cdot 10^{-3}$	$5.123 \cdot 10^{-3}$	$2.423 \cdot 10^{-3}$	$9.199 \cdot 10^{-3}$
750	$5.078 \cdot 10^{-3}$	$5.052 \cdot 10^{-3}$	$2.682 \cdot 10^{-3}$	$9.514 \cdot 10^{-3}$
850	$3.922 \cdot 10^{-3}$	$5.012 \cdot 10^{-3}$	$2.975 \cdot 10^{-3}$	$9.887 \cdot 10^{-3}$
950	$3.055 \cdot 10^{-3}$	$5.026 \cdot 10^{-3}$	$3.278 \cdot 10^{-3}$	$1.008 \cdot 10^{-2}$
1,050	$2.367 \cdot 10^{-3}$	$5.087 \cdot 10^{-3}$	$3.598 \cdot 10^{-3}$	$1.033 \cdot 10^{-2}$
1,150	$1.901 \cdot 10^{-3}$	$5.132 \cdot 10^{-3}$	$3.891 \cdot 10^{-3}$	$1.049 \cdot 10^{-2}$

For a better understanding of the values of the objective function, the surrogate model predictions of the 50 μm fibre and the 1,150 μm fibre in the PA-GF15 composite are presented in the Figures 5.12, 5.13, 5.14 and 5.15, for each material in the uniaxial normal and shear load case in fibre parallel and transverse direction. For the shorter, 50 μm fibre, the objective functions are relatively high with $\epsilon_{fit}^{el} = 3.264 \cdot 10^{-2}$ and $\epsilon_{fit}^{pl} = 3.845 \cdot 10^{-2}$.

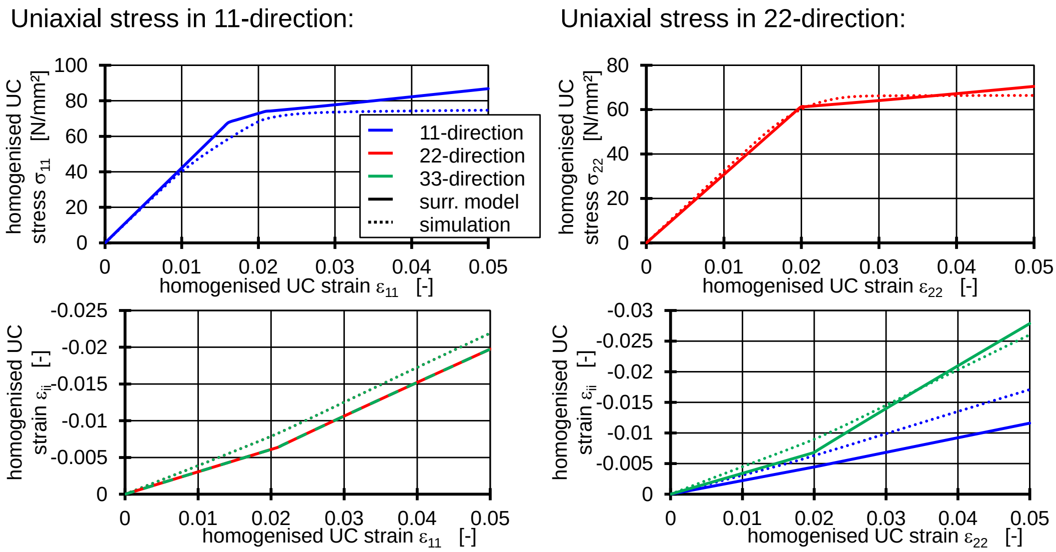

Figure 5.12: Elasto-plastic surrogate model fit on UC-simulation results for the PA-GF15 composite with 50 μm fibre length (normal stress case).

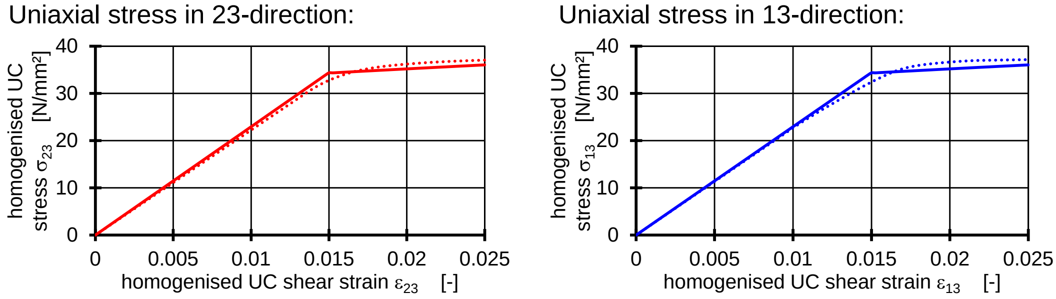

Figure 5.13: Elasto-plastic surrogate model fit on UC-simulation results for the PA-GF15 composite with 50 μm fibre length (shear stress case).

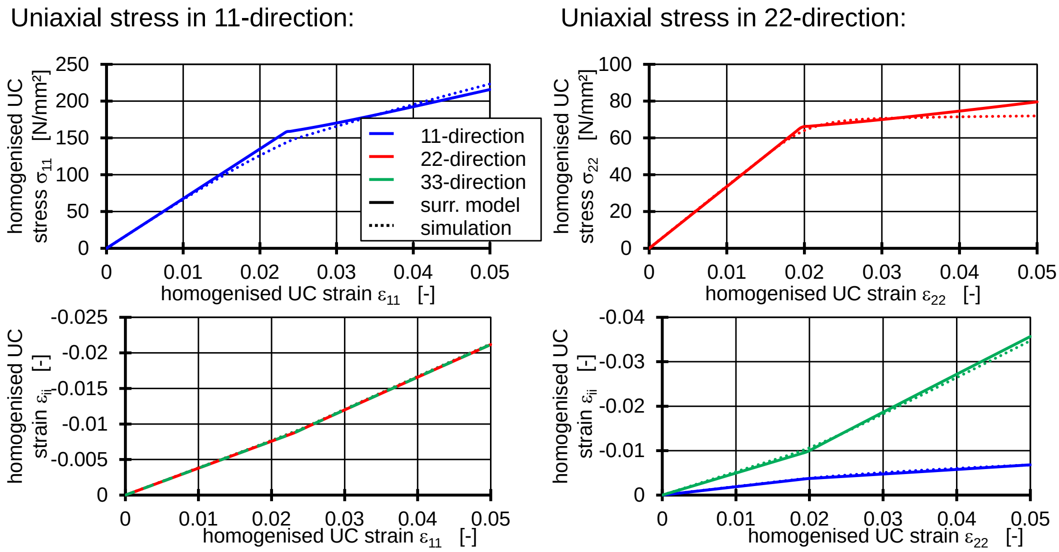

Figure 5.14: Elasto-plastic surrogate model fit on UC-simulation results for the PA-GF15 composite with 1050 μm fibre length (normal stress case).

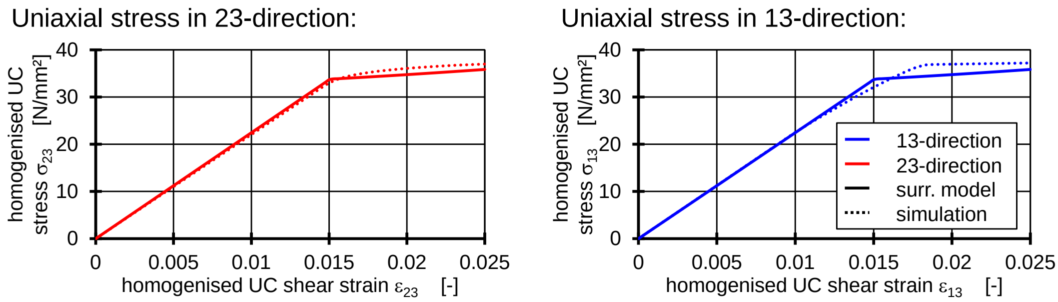

Figure 5.15: Elasto-plastic surrogate model fit on UC-simulation results for the PA-GF15 composite with 1050 μm fibre length (shear stress case).

In Figures 5.12 and 5.13, the largest deviation from the simulation results can be found in the transverse contraction of the UC during the normal uniaxial stress load. Also, a slight deviation fom the stress-strain behaviour in 11-direction can be found. However, there are no major deviations from the UC-simulation responses and therefore, the fit can still be found valid. Looking at the other example with a fibre length of 1,150 μm, the values of the objective functions are much smaller with $\epsilon_{fit}^{el} = 1.901 \cdot 10^{-3}$ and $\epsilon_{fit}^{pl} = 5.132 \cdot 10^{-3}$.

This can also be observed in Figures 5.14 and 5.15, where the surrogate model represents a particularly good fit, compared to the UC-simulations. The parameters for the two examples are listed in Table 5.9. Looking at the model calibration results for the PA-GF30 composite, the trend of the objective function in the elasto-plastic domain is inverted compared to the other material and a much better fit is found for the shorter fibres with a minimum value of the elasto-plastic objective function of $\epsilon_{fit}^{pl} = 6.879 \cdot 10^{-3}$ at a fibre length of 50 µm. For both the PA-GF15 and the PA-GF30 material, the parameter fits show very good results. Hence, it can be progressed with the Orientation averaging with integrated FLD. For the full set of calibrated material parameters, it is referred to Appendix B.

Table 5.9: Surrogate model parameters of the two example fits.

l_F	E	ν	k	σ_y	R	κ_1	κ_2	κ_3
[µm]	[MPa]	[-]	[-]	[N/mm²]	[-]	[-]	[-]	[-]
50	2,993	0.3046	1.300	61.33	1.463	20.38	0.000	0.000
1,150	3,094	0.3788	1.636	66.21	10.58	22.40	1,254	392.5

5.2.1.2 Orientation Averaging predictions

First, the prediction results for the PA-GF15 composite are investigated. Figure 5.16 shows the stress response of the composite for a uniaxial load case in 1-direction. The three interaction

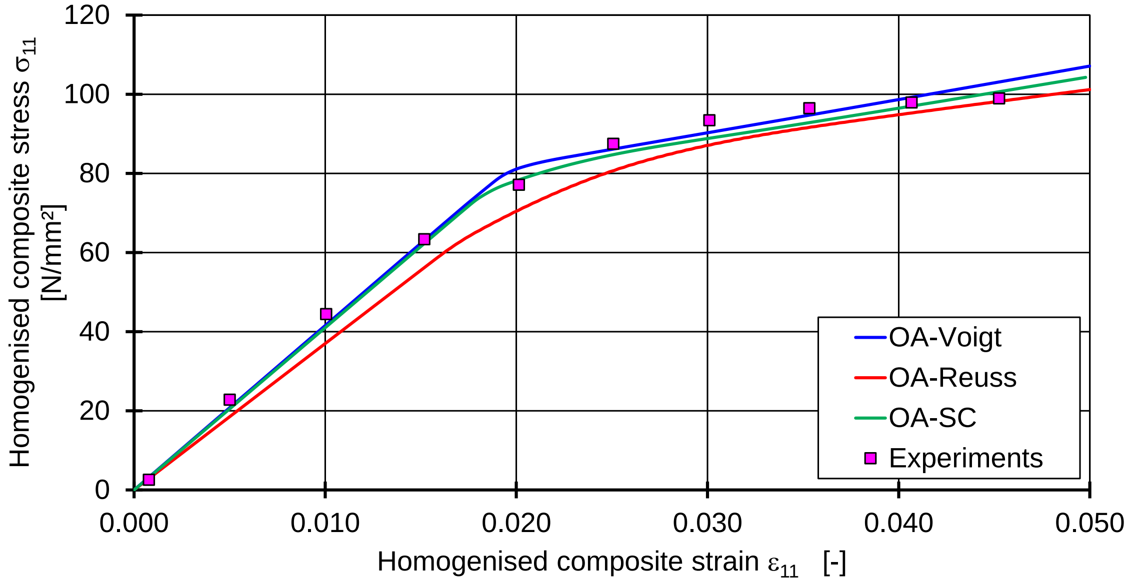

Figure 5.16: Elasto-plastic OA-predictino on the PA-GF15 composite for uniaxial stress in 1-direction in comparison to experimental results [27].

assumptions show relatively good agreements with the experimental results. For the initial linear elastic part, the Voigt and the self-consitent assumtpion predict very similar behaviour, whereas the Reuss assumption predicts a lower initial stiffness. In comparison to the experimental results, the OA-predictions underestimate the initial material behaviour. All this is in agreement with the linear elastic Young’s moduli presented in Chapter 5.1.2.

The plastic deformation starts at different homogenised stresses for each interaction assumption. The Reuss assumption predicts the lowest yield stress with approximately 60 MPa. After that, the self-consistent assumption predicts the intermediate point for the deviation from the linear elastic behaviour at a stress level of around 75 MPa. The Voigt assumption predicts the yield stress with about 80 MPa. It is noticed that in comparison to the experiments, the material model predictions have a much more pronounced Yield point, followed by a close to linear hardening behaviour, especially for the Voigt and self-consistent assumtion. However, the OA-predictions show a very good fit compared to the experimental results.

In the nex step, the OA-predictions using FLD are compared to the OA-prediction using single representative fibre lengths, for each interaction assumption seperately. As an example, the three averaged fibre lengths are compared directly to the OA-prediction using FLD for the Voigt assumption in Figure 5.17.

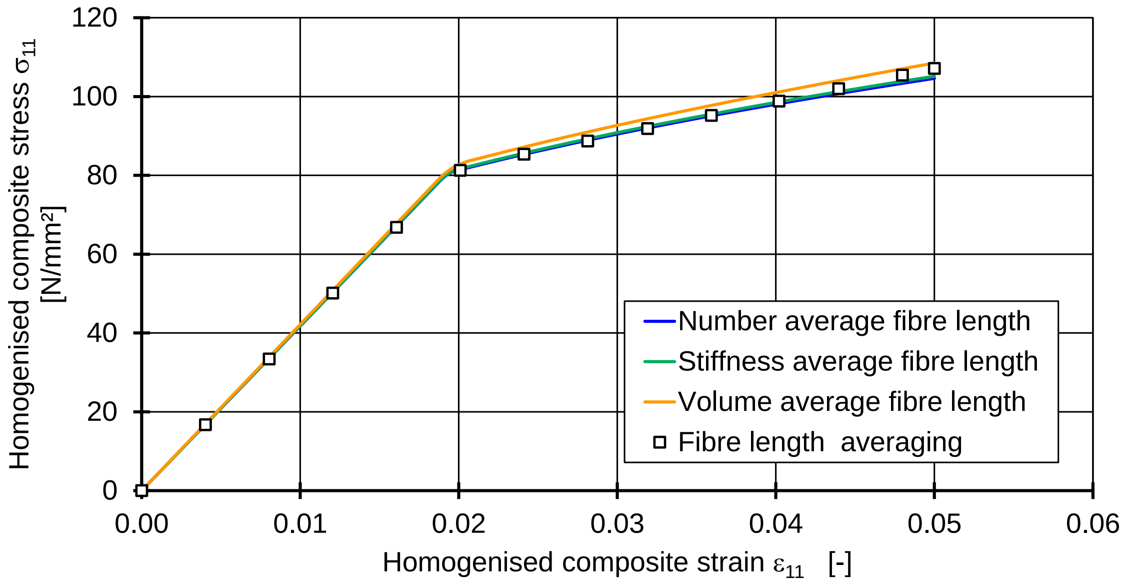

Figure 5.17: Direct comarison of the elasto-plastic OA-predictions with representative fibre lengths and using fibre length averaging on the PA-GF15 composite.

A very good fit is observed for all three averaged fibre lengths, whith the three curves showing almost no differences in the direct comparison. Hence, to obtain a better impression of the differences in the representative fibre lengths predictions, the relative error compared to the OA-prediction using FLD is plotted in Figure 5.18 for the Voigt interaction assumption.

It is observed that the volume-averaged fibre length overpredicts the homogenised composite stress, whereas the number- and the stiffness-averaged fibre length underpredict the stresses. In the initial linear elastic phase, the three representative fibre lengths have a constant error of 1.5 % for the volume-averaged fibre length , 0.5 % for the number-averaged and 0.6 % for the stiffness-averaged fibre length. At the yield point, all curves show a small peak up to higher values before descending and then peaking again. For increasing strain the error values seem to increase before the values reach a maximum and then decrease again. Both number- and stiffness-averaged fibre length cut the 0% error line, before they decrease to higher absolute errors. For a better understanding of the overall fit of the single fibre length predictions to the fibre length averaging method, the average of the absolute errors for all strain increments is considered. For the volume-averaged fibre length. a value of 1.98 % is found. The number-averaged fibre length gives the lowest value with 0.59 % and the stiffness-averaged fibre length prediction reaches a value of 0.62 %.

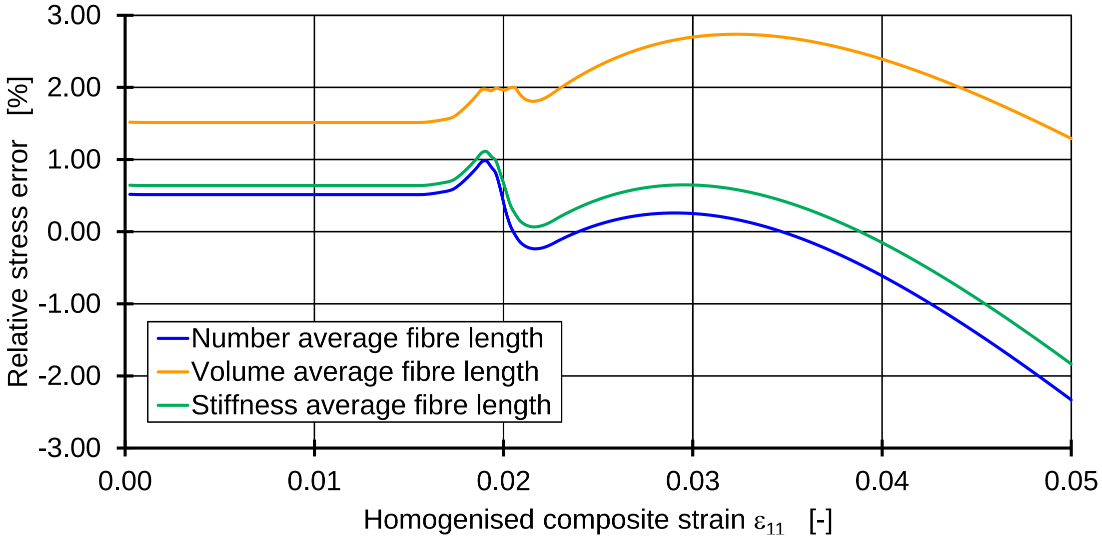

Figure 5.18: Relative error for the OA-predictions with representative fibre lengths to the OA predictions using fibre length averaging with the Voigt assumption.

In analogy to that, the relative error values for the Reuss and self-consistent interaction assumption are presented in Figures 5.19 and 5.20. For the three interaction assumptions, very different behaviour in the evolution of the relative error is observed. The differences are especially visible in the elasto-plastic domain of the strain load. For the Reuss assumption even an oscillating behaviour is obtained.

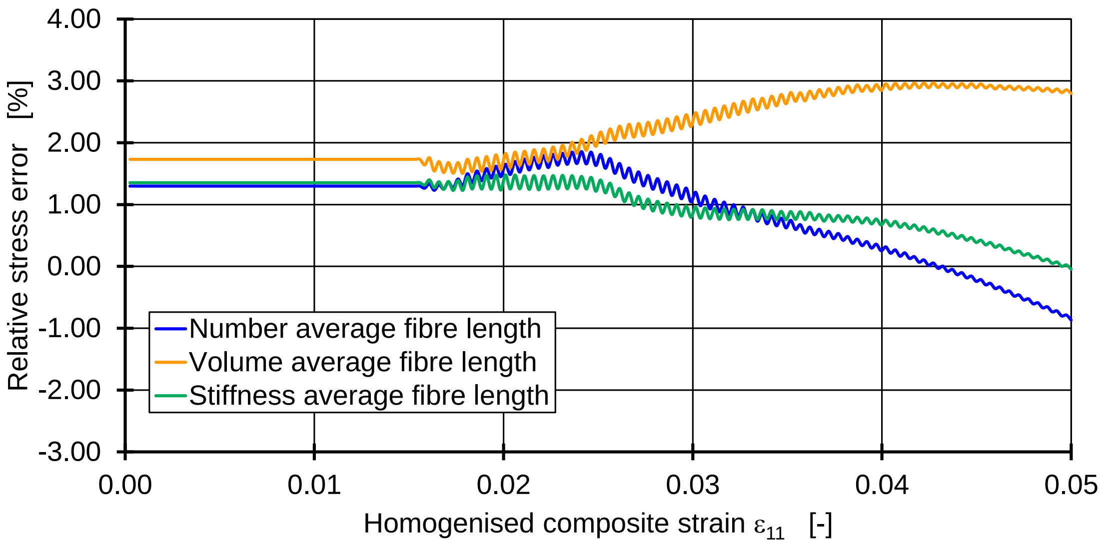

Figure 5.19: Relative error for the OA-predictions with representative fibre lengths to the OA predictions using fibre length averaging with the Reuss assumption.

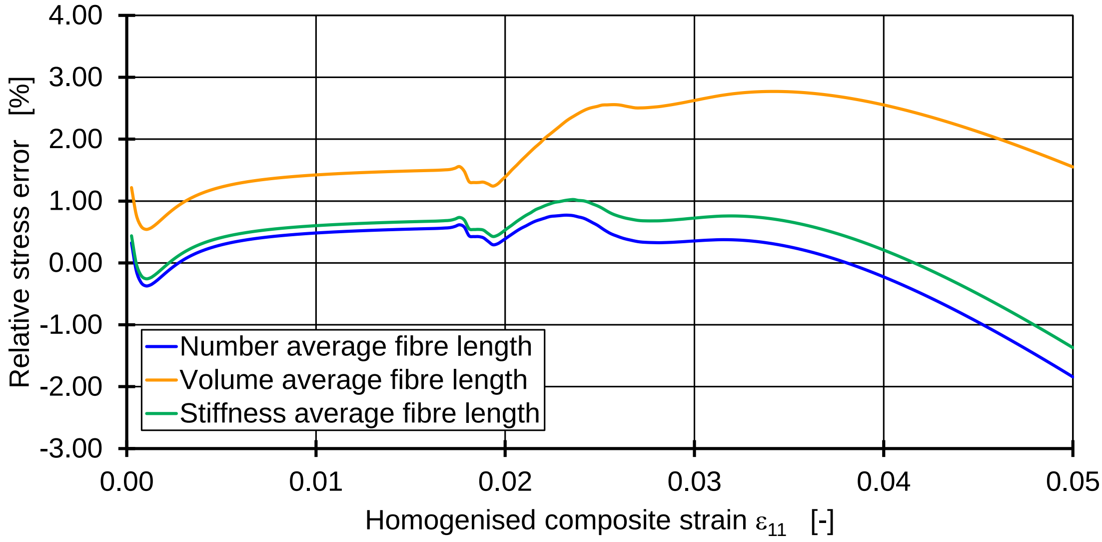

Figure 5.20: Relative error for the OA-predictions with representative fibre lengths to the OA predictions using fibre length averaging with the self-consistent assumption.

The average absolute error is, however, generaly lower compared to the OA-predictions using the Voigt assumption. The values for the average relative error are summarised in **Fehler! Ungültiger Eigenverweis auf Textmarke.**.

Table 5.10: Average absolute error values for the OA-results with representative fibre lengths compared to OA-predictions with FLD for PA-GF15.

Interaction assumption	l_F	**OA-Voigt**	**OA-Reuss**	**OA-SC**
Average absolute error	[μm]	[%]	[%]	[%]
Number-averaged fibre length	430	0.59	1.04	0.51
Stiffness-averaged fibre length	443	0.62	1.01	0.60
Volume-averaged fibre length	532	1.98	2.21	1.94

It can be concluded that the volume-averaged fibre length tends to overpredict the material behaviour compared to the OA-predictions considering the FLD. The number- and the stiffness-averaged fibre lengths, however, rather underpredict the reference. Looking at the average absolute errors, it can be seen that the number- and stiffness-averaged fibre lengths give the better predictions compared to the reference.

With the presented OA-method, not only the uniaxial stress response is calculated, but the full strain response is evaluated as well. For this load case, contractions in the transverse 2- and 3-directions are expected. Shear strains can be neglected due to the symmetric FOD in respect to the sufaces spanned by the coordinate axes. The strain responses in the 2- and 3-directions are depicted in Figure 5.21. Note the inverted vertical axis in the graph. For the transverse contraction response, the three interaction assumption models show relatively similar behaviour. Also the resulting strain response is very similar for both directions in the initial, linear elastic domain. For the ongoing elasto-plastic domain, the strain in 3-direction seems to be more affected and the transverse contraction in that direction increases, compared to the

2-direction. Unforunately, there is no information from the literature about the transverse contraction response. Hence, the quality of the OA-predictions can not be evaluated in this case.

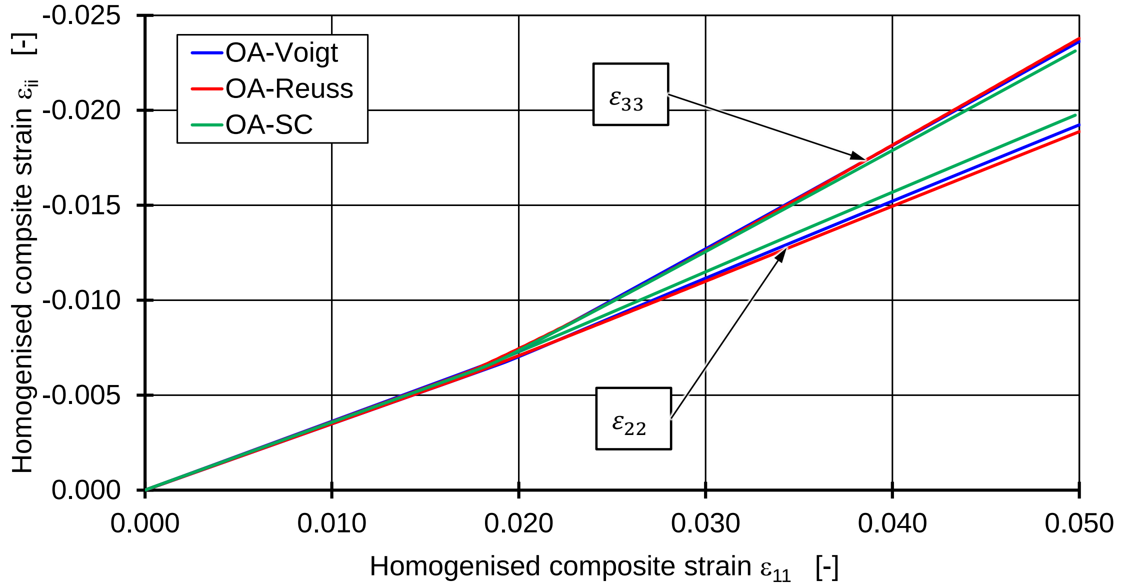

Figure 5.21: Elasto-plastic OA-prediction on the PA-GF15 composite for uniaxial stress in 1-direction for the transverse strain response.

The second material, PA-GF30 is handled in the following. In analogy to the previous example, first the OA-predictions considering the FLD for a uniaxial stress load case in 1-direction are presented. The resulting stress strain curves in comparison to the experimental results are shown in Figure 5.22. It is observed that, again, the predictions using the Voigt and the self-consistent assumptions are relativey close to each other. The prediction using the Reuss assumption is seperated more clearly from the other two.

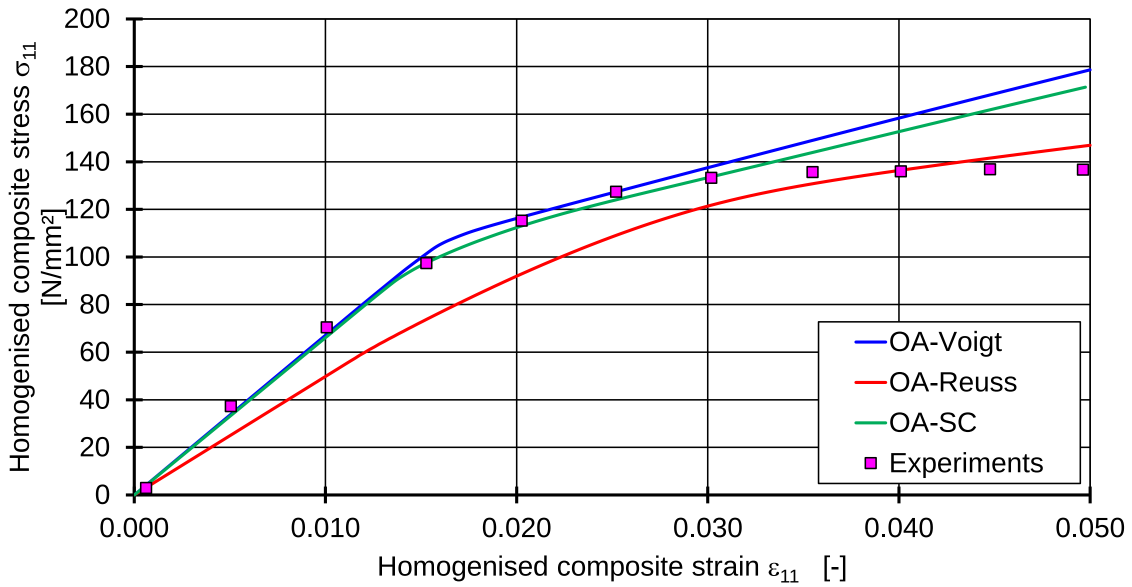

Figure 5.22: Elasto-plastic OA-prediction on the PA-GF30 composite for uniaxial stress in 1-direction in comparison to experimental results [27].

Compared to the experimental results, the Voigt and self-consistent assumption predictions show a very good agreement up to 3 % homogenised strain, where the OA-model starts to overestimate the stress response of the composite. It is to expect that the elasto-plastic model is only valid up to a certain strain. The presented model does not include any material damage such as for example fibre matrix debonding. Additionally, the used hardening behaviour in the surrogate model usually gets less accurate for increasing strain. This may explain the deviation of the elasto-plastic OA-model for higher strain loads.

Comparing the OA-results using FLDs to those with a single representative fibre length, again, a very good agreement between the models is found. Thus, the average absolute errors compared to the OA-method using the FLD-information is investigated with the values given in Table 5.11. It is seen that the number- and the stiffness-averaged fibre lengths give the better estimation of the reference prediction, with average absolute errors of under 1 %. The volume-averaged fibre length produces higher errors in the predictions with error values over 1 % and even greater than 2.5 % for the Voigt and the self-consistent assumption. Still this could be assessed as a good fit to the OA-model considering FLD.

Table 5.11: Average absolute error values for the OA-results with representative fibre lengths compared to OA-predictions with FLD for PA-GF30.

Interaction assumption	l_F	**OA-Voigt**	**OA-Reuss**	**OA-SC**
Average absolute error	[μm]	[%]	[%]	[%]
Number-averaged fibre length	366	0.61	0.46	0.62
Stiffness-averaged fibre length	372	0.61	0.40	0.66
Volume-averaged fibre length	425	2.65	1.21	2.59

The specimens for the tensile tests , which are referred to in this chapter are cut from injection moulded plates in relation to the Injection Flow Direction (IFD) as visualised in Figure 5.23.

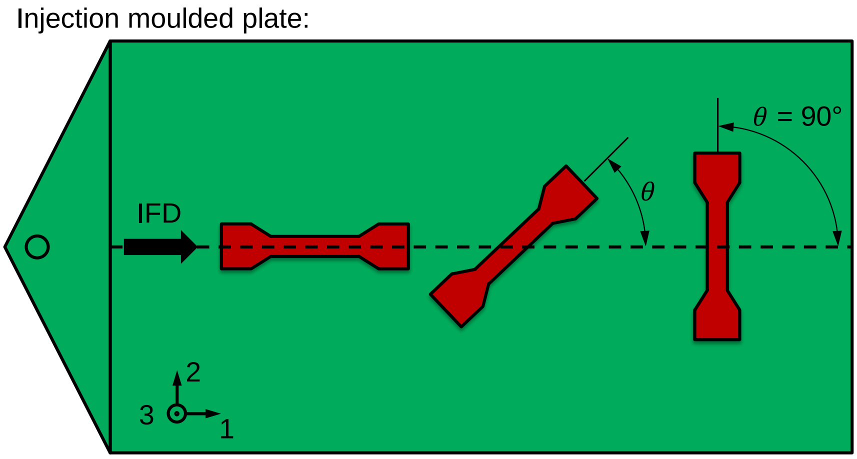

Figure 5.23: Schematic specimen extraction from the injection moulded plate in reference to the IFD.

With this, anisotropic response of the composite, due to the specific FOD, was captured. From the tests on specimens cut on an angle of $\theta = 90$ °, the material response for a uniaxial stress load in 2-direction can be obtained.

For the PA-GF30 composite the experimental results of specimens cut from an angle θ = 90 ° are compared to the corresponding OA-predichtions in the following. First, the OA-simulations considering the FLD are presented in Figure 5.24.

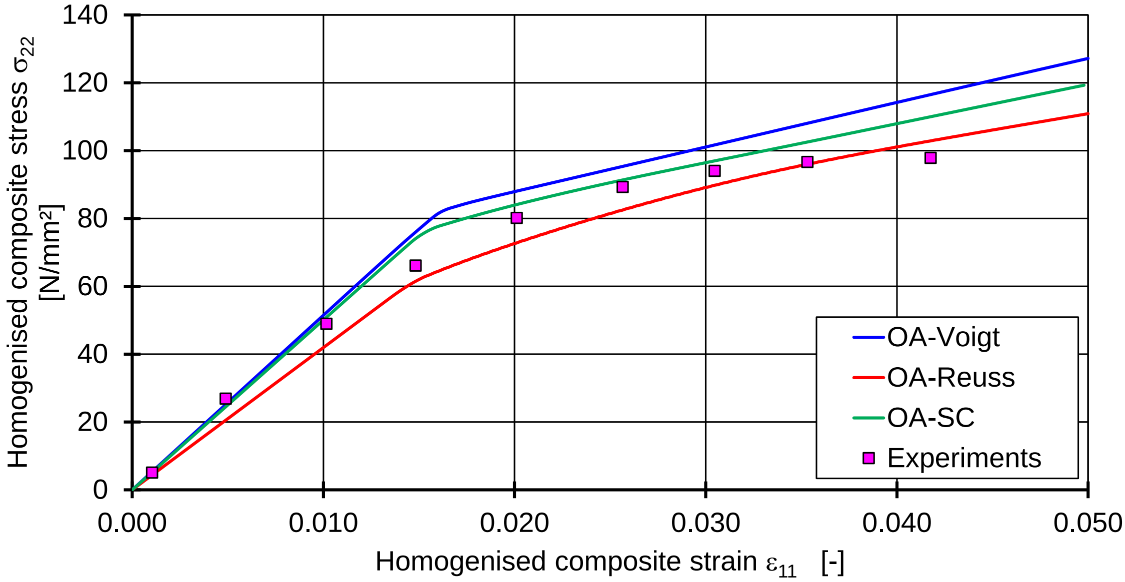

Figure 5.24: Elasto-plastic OA-prediction on the PA-GF30 composite for the uniaxial stress case in 2-direction in comparison to the experimental results [27].

Due to the lower frequency of fibre orientations in the 2-direction, the OA-predictions reach lower values for the composite stress response in the last strain increment compared to the 1-direction. The qualitative behaviour of the material, however, is very similar for the OA-predictions as well as for the experimental results. The OA-predictions represent the material behaviour very well, up until a certain strain load, where the OA-model predictions deviate to higher stresses than the experiments.

In terms of the OA-predictions using representative fibre lengths, again, a very good fit, compared to the previous predictions is observed. Table 5.12 shows the average absolute error, obtained from the OA-predictions with the respective interaction assumption. The maximum overall value is less than 1.5 %. Hence, the fit can be evaluated very good. In this case , the stiffness-averaged fibre length predictions show the best agreement with the full FLD OA-prediction for all interaction assumptions. However, the difference to the other two representative fibre lengths is not significant in most cases.

Table 5.12: Average absolue error values for the OA-results with representative fibre lengths compared to OA-predictions with FLD for PA-GF30 (load in 2-direction).

Interaction assumption	l_F	**OA-Voigt**	**OA-Reuss**	**OA-SC**
Average absolute error	[µm]	[%]	[%]	[%]
Number-averaged fibre length	366	0.72	1.07	0.73
Stiffness-averaged fibre length	372	0.64	0.86	0.70
Volume-averaged fibre length	425	1.49	0.97	1.38

5.2.2 Glass fibre reinforced Polyamide 6.6

The second analysis, conducted by the elasto-plastic Orientation Averaging model is carried out on a composite from *Sasayama, Okabe et al.* [52]. Therein the authors present four individual uniaxial stress tests on different types of specimens made of a glass fibre reinforced Polyamide 6.6 composite with a fibre volume fraction of 17 %. Again, the authors do not mention a commercial product. However, it can be assumed that the CM3001G30 composite or a similar material using the AMILAN PA-66 by Toray Industries is used [56]. This fibre matrix material combination is similar to the previously presented example. However, the used material properties differ from the previous example. Additionally, the FLDs and FODs presented here are quite different. Hence, this example is considered as a valid addition to the assessment of prediction capabilities of the OA-model.

5.2.2.1 Material parameters and model calibration

The elastic material properties of the composite are presented in Table 5.13. In comparison to the previous example, the fibre Young's modulus is given with a higher value of 76,000 MPa. The elastic parameters of the matrix are given with the Young's modulus of 2,800 MPa and a Poisson's ratio of 0.33. The average fibre diameter is considered with 13 μm.

Table 5.13: Elastic material properties of the constituents in glass fibre reinforced Polyamide-6.6 composite [52].

Property	**Symbol**	**Value**	**Unit**
Matrix Young's modulus	E_M	2,800	MPa
Matrix Poisson's ratio	ν_M	0.33	-
Fibre Young's modulus	E_F	76,000	MPa
Fibre Poisson's ratio	ν_F	0.2	-
Mean fibre diameter	d_F	13	μm
Fibre volume fraction	φ	0.170	-

Considering the elasto-plastic behaviour of the matrix, *Sasayama, Okabe et al.* conducted tensile tests on a pure matrix specimen. The authors calibrate a material model on the obtained stress-strain behaviour [52]. The model consists of a substantial number of parameters and is therefore not used in this work. Instead, in accordance with the previous example, a von Mises yield criterion with a linear hardening model is used. The material behaviour from the experiments is compared to the calibrated elasto-plastic model in Figure 5.25. The material behaviour is represented very well by the von Mises yield criterion with linear hardening plasticity up to a maximum logarithmic strain of 0.2. From the calibration, the matrix yield stress is obtained with σ_y = 79.04 N/mm² and the hardening modulus with H = 95.36 N/mm².

Two different specimen types are considered in this example. A smaller, dumbbell shaped specimen, cut from an injection moulded plate is referred to as the 'Type 1' specimen. Another

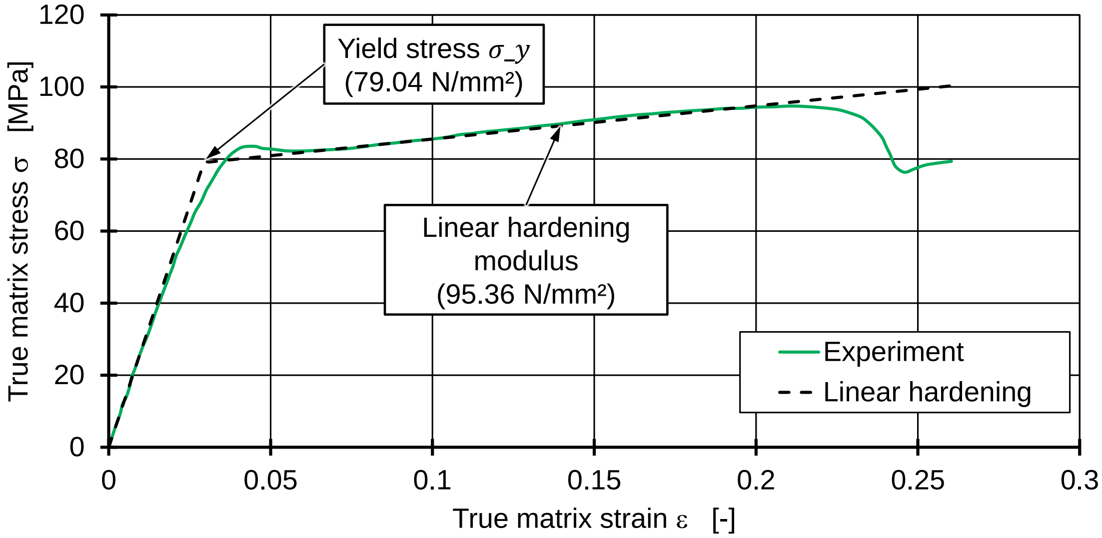

Figure 5.25: Stress-strain experiment on a PA-6.6 matrix [52] in comparison to the elasto-plastic model with linear hardening.

other, larger specimen, which is directly injection moulded in the dumbbell shape, is noted as the 'Type 2' specimen. Further, two different initial fibre lengths are taken for the injection moulding of each of the two specimen types. A longer initial fibre length, referred to as LGF and a shorter fibre referred to as SGF. The FOD in all specimens is here interpreted as planar (a_{33} = 0), due to the low thickness of the specimens. Generally, Type 2 specimens show an FOD with a higher concentration of fibres in the 1-direction. In contrast to that, Type 1 specimens have a nearly 2D-random distribution with a slight preference in the 2-direction. Due to the different initial fibre lengths and the different flow conditions in the two moulds, the specimens result with different FLDs.

The FLDs and FODs for each LGF and SGF, with the specimen shapes Type 1 and 2 are depicted in the Figures 5.26, 5.27, 5.28 and 5.29. The fibre length distribution is divided in

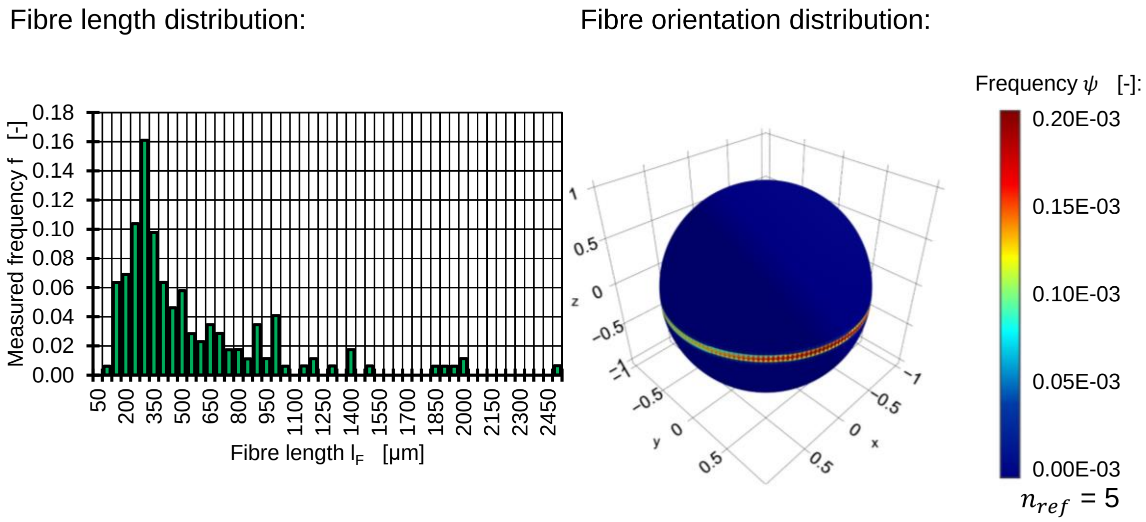

Figure 5.26: Fibre length distribution and fibre orientation distribution of the LGF Type 1 specimen from Sasayama, Okabe et al. [52].

Fibre length distribution: Fibre orientation distribution:

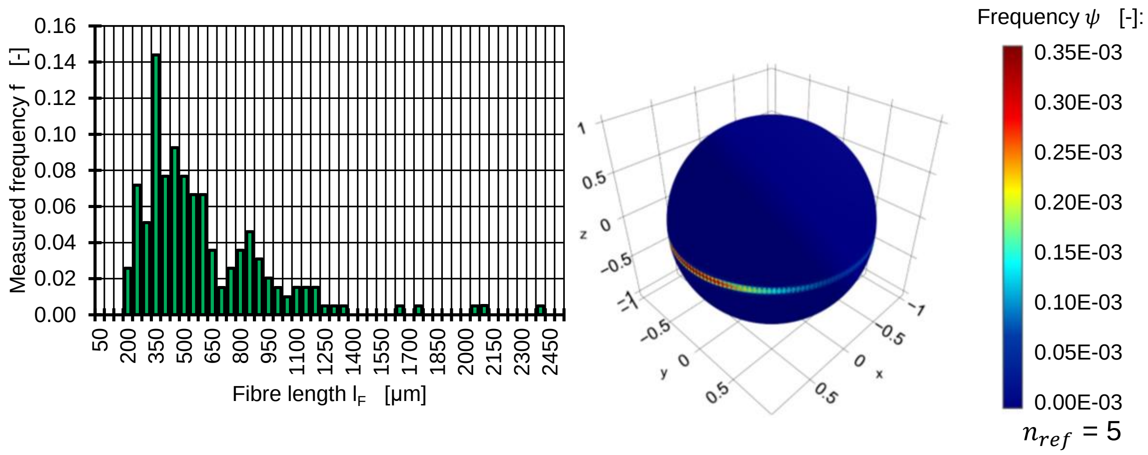

Figure 5.27: Fibre length distribution and fibre orientation distribution of the LGF Type 2 specimen from Sasayama, Okabe et al. [52].

Fibre length distribution: Fibre orientation distribution:

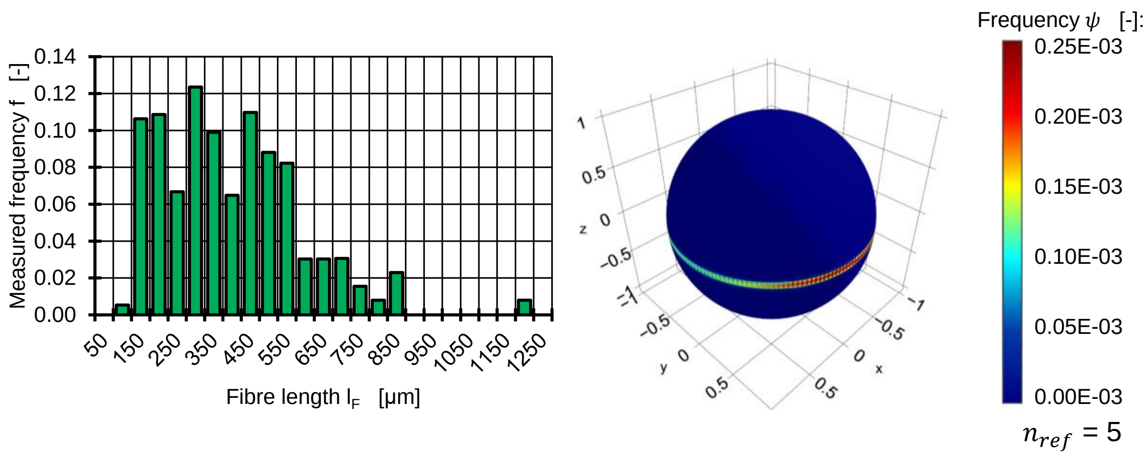

Figure 5.28: Fibre length distribution and fibre orientation distribution of the SGF Type 1 specimen from Sasayama, Okabe et al. [52].

Fibre length distribution: Fibre orientation distribution:

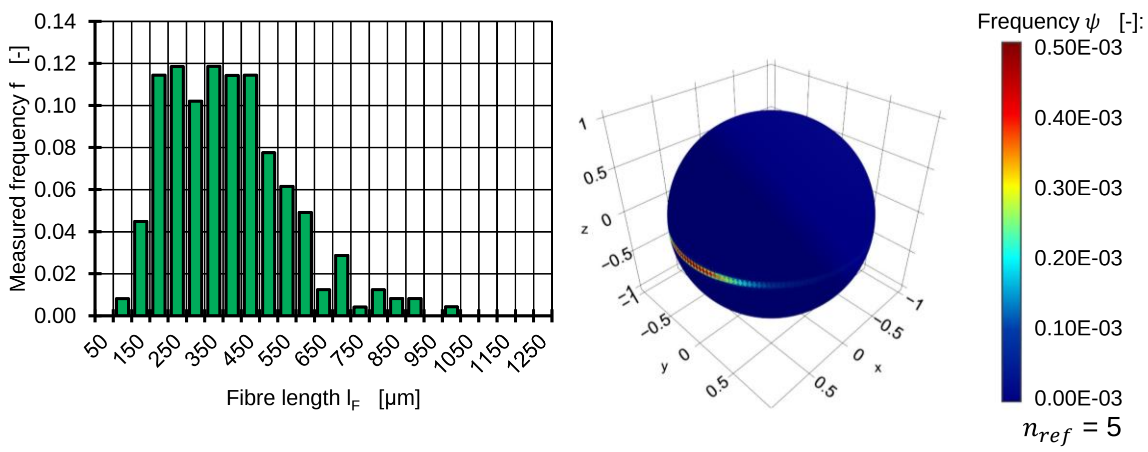

Figure 5.29: Fibre length distribution and fibre orientation distribution of the SGF Type 2 specimen from Sasayama, Okabe et al. [52].

length intervals of 50 μm. For a total range from 0 μm to 2,500 μm, 50 fibre length classes are obtained. From the FODs, on the right side of the figures, it is seen that the planar distribution is not fully representable with the icosphere discretisation method, since the triangle center points do not perfectly represent the equator of the Unit Sphere. However, for the LGF Type 1 specimen, the resulting FOD from the Bingham distribution with a standard number of four refinement steps results in a diagonal FODT $\boldsymbol{a} = diag(0.450, 0.549, 0.001)$. This can still be considered as a planar FOD. The resulting FODT and averaged fibre lengths are presented in Table 5.14.

Table 5.14: FOD and FLD for the four different specimen types [52].

Initial fibre length	**LGF**		**SGF**	
Specimen type	**Type 1**	**Type 2**	**Type 1**	**Type 2**
Orientation distribution a_{11} [-]	0.451	0.692	0.412	0.815
Orientation distribution a_{22} [-]	0.549	0.308	0.588	0.184
Number-averaged fibre length [μm]	542	590	385	392
Stiffness-averaged fibre length [μm]	562	607	398	400
Volume-averaged fibre length [μm]	862	795	478	461

The UC-simulations for the corresponding fibre length classes and representative fibre length are conducted and the homogenised material response is obtained. With the material response from the simulation, the surrogate material model is calibrated as described in the previous chapters. The full set of surrogate model parameters for both the fibre length classes and the representative fibre lengths can be found in Appendix B. The overall surrogate model calibration results are considered good with an overall range of the elastic objective function ϵ_{fit}^{el} of $2.720 \cdot 10^{-3}$ to $7.677 \cdot 10^{-3}$ and for the elasto-plastic objective function ϵ_{fit}^{pl} of $7.126 \cdot 10^{-3}$ to $1.407 \cdot 10^{-2}$. The presented fit is, therefore, significantly better than for the one, presented in Subsection 5.2.1.

5.2.2.2 Orientation Averaging predictions

The OA-predictions for the four different FLD and FOD combinations are compared to the experimental results separately. First, the LGF Type 1 specimen is investigated. The corresponding material response for a uniaxial load case in 1-direction is presented in Figure 5.30 in comparison to the OA-prediction using the FLD. A very good agreement with the experimental results is found, as the obtained data points are well within the range of the OA-predictions with the different interaction assumptions. The three different interaction assumptions result in three destinguishable OA-predictions with the Reuss assumption building the minimum, the Voigt assumption represents the maximum and the self-consistent assumption giving an intermediate approach for the expected stress response of the composite.

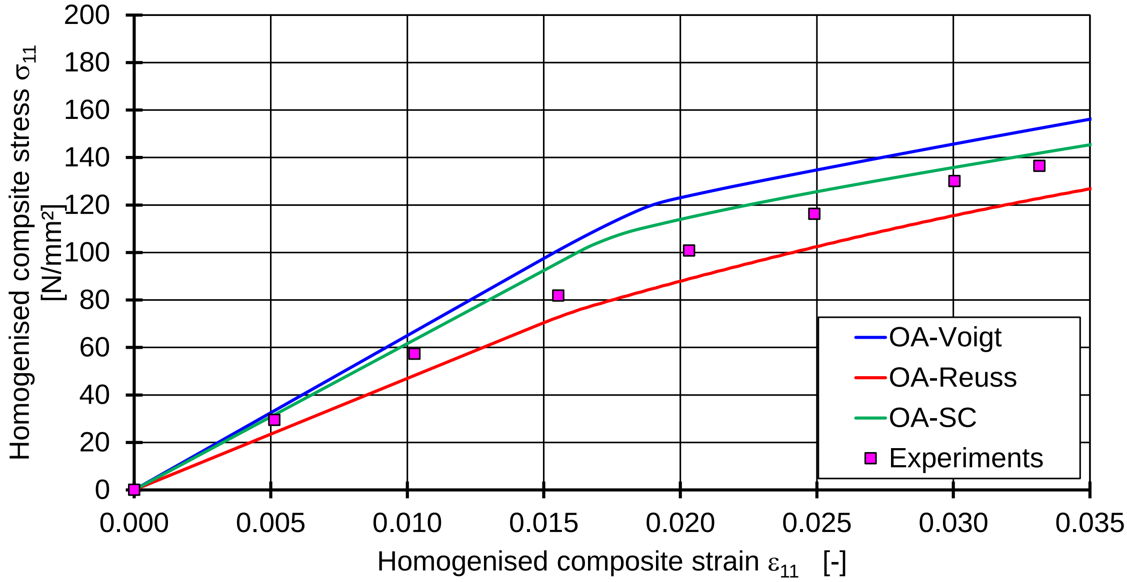

Figure 5.30: Elasto-plastic OA-prediction on the LGF Type 1 composite for the uniaxial stress load case in 1-direction in comparison to experimental results [52].

The well destinguishable stress responses of the interaction assumption predictions in the graph allow for a grouped comparison of those with the OA-predictions using the representative fibre lengths. This comparison is shown in Figure 5.31. It is observed that the OA-predictions with

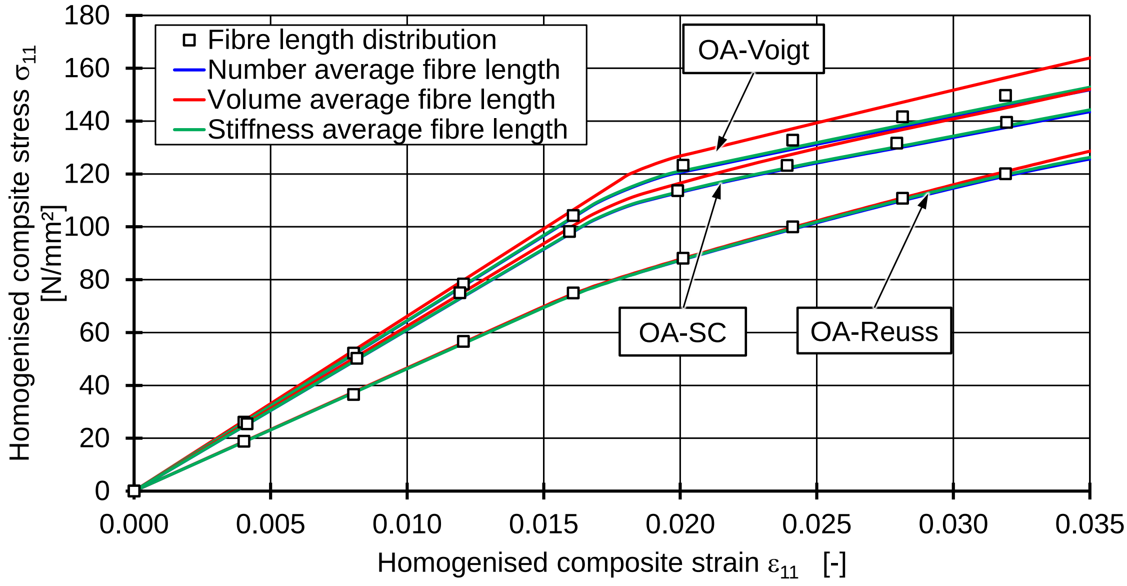

Figure 5.31: Direct comparison of OA-predictions using representetive fibre lengths with the method using fibre length averaging.

the representative fibre lengths are very close to its corresponding prediction using the fibre length distribution. However the volume-averaged fibre length exceeds those values by a significant amount for the Voigt and the self-consistent interaction assumption in the elasto-plastic domain. The predictions for the number- and the stiffness-averaged fibre length using the Voigt assumption are underestimating the stress response. However, this difference is not so significant. To quantify the agreement of the representative fibre lengths compared to the OA-prediction using the FLD, the average absolute error values for the three interactionassumptions are given in Table 5.15. It is seen that for all interaction asumptions the stiffness-averaged fibre length gives the best approximation to the OA-method using the FLD-information.

Table 5.15: Average absolute error values for the OA-results with representative fibre lengths compared to OA-predictions with FLD for LGF Type 1.

Interaction assumption	l_F	**OA-Voigt**	**OA-Reuss**	**OA-SC**
Average absolute error	[μm]	[%]	[%]	[%]
Number-averaged fibre length	542	2.00	1.27	1.05
Stiffness-averaged fibre length	562	1.53	0.98	0.70
Volume-averaged fibre length	862	3.78	1.16	3.39

As second specimen, the LGF Type 2 material is chosen. The FOD with a more pronounced fibre orientation concentration in the testing direction is expected to result in a higher initial stiffness and maximum stress in the OA-predictions, as experimental results suggest [52]. The corresponding OA-predictions using the FLD are presented in Figure 5.32 in comparison with the experimental results. Again, a very good fit between the OA-model and experimental results

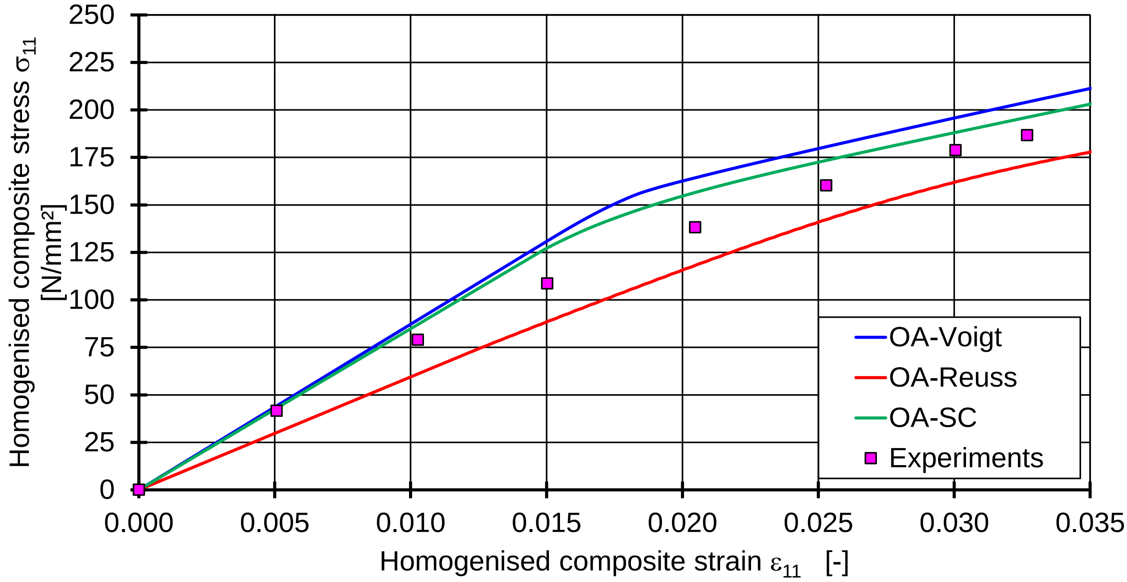

Figure 5.32: Elasto-plastic OA-prediction on the LGF Type 2 composite for the uniaxial stress load case in 1-direction in comparison to experimental results [52].

is observed. Also, the expected higher stress response for that model is observed. The stress at 3 % strain is noted with 195 N/mm² for the Voigt assumption in comparison to 145 N/mm² in the previous example. For the Reuss assumption these values are obtained with 115 N/mm² for the LGF Type 1 and 161 N/mm² for the LGF Type 2 specimen. The corresponding values for the self-consistent are found for the LGF Type 1 with 136 N/mm² and the LGF Type 2 with 187 N/mm².

Comparing the OA-predictions using FLD with those using the representative fibre lengths a very good agreement could be found, presened in Table 5.16 with the average absolute errors.

Table 5.16: Average absolute error values for the OA-results with representative fibre lengths compared to OA-predictions with FLD for LGF Type 2.

Interaction assumption	l_F	**OA-Voigt**	**OA-Reuss**	**OA-SC**
Average absolute error	[μm]	[%]	[%]	[%]
Number-averaged fibre length	590	1.24	2.12	0.51
Stiffness-averaged fibre length	607	0.76	0.45	0.17
Volume-averaged fibre length	795	3.52	2.58	3.74

It is found that for this model, a clear order of conformity with the reference results applies. For all interaction assumptions, the stiffness-averaged fibre length gives the closest predictions to the OA-predictions using the FLD. The other representative fibre lengths producing larger average errors with the volume-averaged giving the least accurate prediction of the stress response and the number-averaged producing intermediate error values. The average error for the stiffness-averaged fibre length in all interaction assumptions is less than 1 %. Hence the fit to the reference is considered very good.

With the LGF specimens investigated, it is now continued with the SGF specimens produced with the shorter initial fibre length. In analogy to the previous two examples, first, the OA-predictions for the Type 1 specimen are analysed.

The stress responses from the OA-predictions using the full FLD-information are presented in Figure 5.33 in comparison to the experimental results. The overall stress response for this material is found to be smaller than the two examples discussed earlier. This is due to the on average shorter fibres in the composite. The OA-predictions represent the experimental material behavior fairly well. In this case, the Reuss assumption seems to give a very good prediction of the material behaviour.

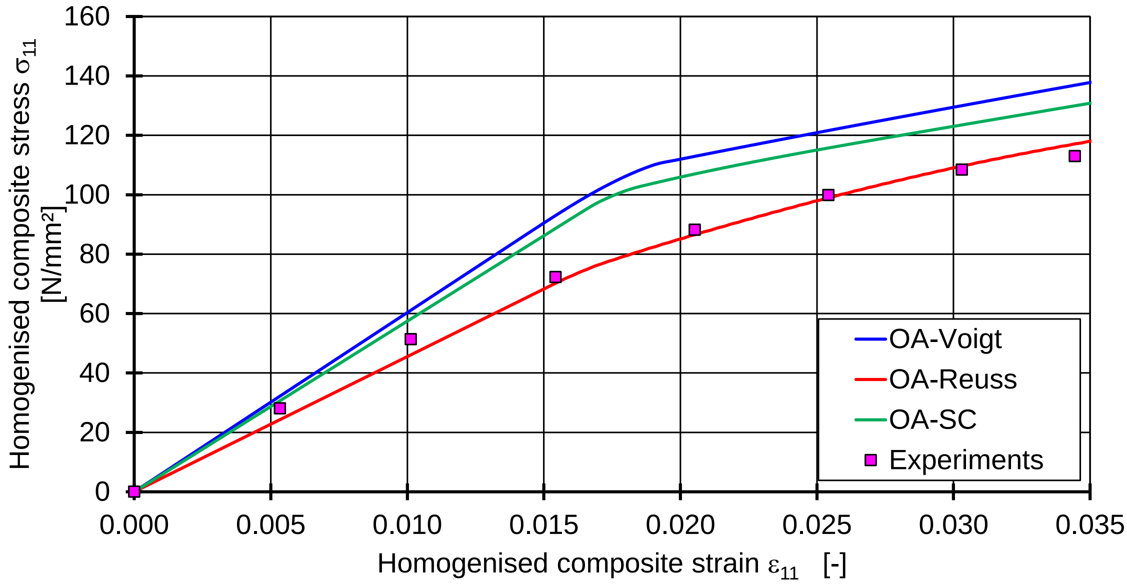

Figure 5.33: Elasto-plastic OA-prediction on the SGF Type 1 composite for the uniaxial stress load case in 1-direction in comparison to experimental results [52].

Comparing these predictions to those obtained with a single representative fibre length, a very good agreement is found between them. This is shown in Table 5.17, in which the average absolute error compared to the reference is presented. Again, an order of the fits of the representative fibre lengths for all interaction assumptions can be given. In analogy to the previous example, using the stiffness-averaged fibre length gives the best predictions. The second-best predictions result from the number-averaged fibre length. And the volume-averaged fibre length gives the least accurate prediction.

Table 5.17: Average absolute error values for the OA-results with representative fibre lengths compared to OA-predictions with FLD for SGF Type 1.

Interaction assumption	l_F	**OA-Voigt**	**OA-Reuss**	**OA-SC**
Average absolute error	[μm]	[%]	[%]	[%]
Number-averaged fibre length	385	1.51	0.80	1.07
Stiffness-averaged fibre length	398	1.07	0.64	0.72
Volume-averaged fibre length	478	1.61	0.87	1.38

Finally, the last example from *Sasayama et al.* [52] is investigated. The specimen SGF Type 2 has the FOD with the highest orientation concentration in loading direction of all four specimens in this chapter. Hence, a higher resulting stress response is to expect for this model. Figure 5.34 shows the corresponding OA-predictions using the FLD information in comparison to the experimental results. Despite the lower averaged fibre lengths, the OA-predictions estimate a higher initial stiffness as well as a higher maximum stress than all other examples of this material.

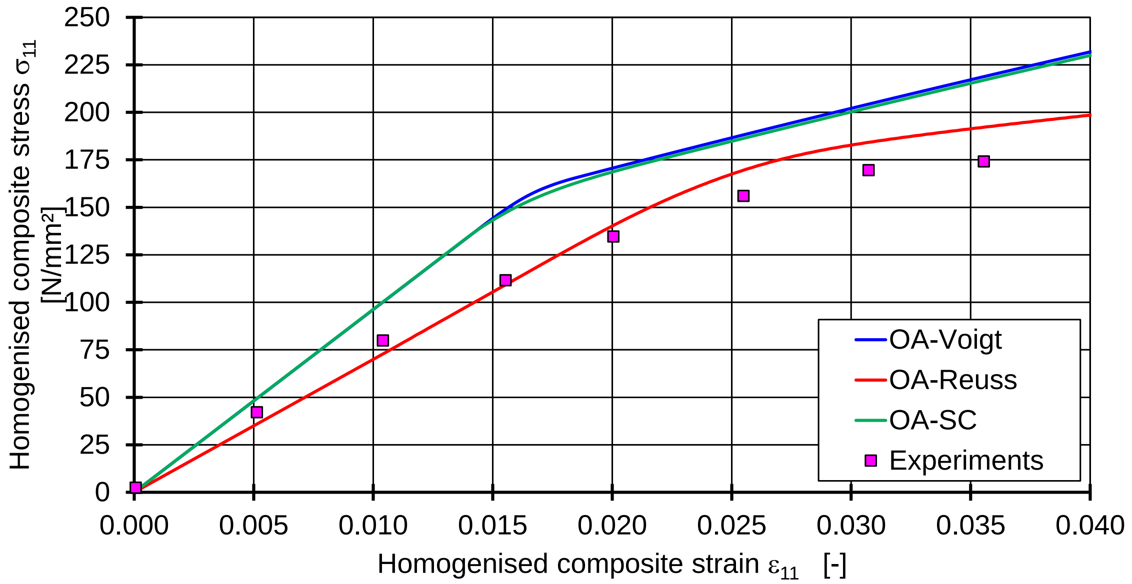

Figure 5.34: Elasto-plastic OA-prediction on the SGF Type 2 composite for the uniaxial stress load case in 1-direction in comparison to experimental results [52].

The experimental results show a similar behaviour compared to the previous examples, with a very similar initial stiffness compared to the LGF Type 2 specimen. The maximum stress, however, is lower than that for the longer fibre composite; maximum values are 175 N/mm² and 187 N/mm² respectively. This difference between the model and the experimental results may be explained with damage that is expected in the material for such high strain loads. The OA-model, however, does not represent any damage evolution in the material behaviour. Nevertheless, the OA-predictions can still be interpreted as a good fit compared to the experimental results, as the initial stresses from the experimental results are well inside the range of the OA-predictions. It is additionally observed that the Voigt and self-consistent assumptions produce very similar results in this case. In comparison to the experimental results the Reuss assumption gives the best prediction of the material behaviour.

Comparing the OA-predictions using the FLD information to the OA-predictions obtained with the averaged fibre lengths a good agreement is found. The resulting average absolute errors are presented in Table 5.18. As mentioned in the previous examples, a clear order of the agreement with the OA-predictions using FLD-information is found for the averaged fibre lengths. The OA-method using the stiffness-averaged fibre length gives the best prediction compared to the reference. From this, the number-averaged fibre length follows ahead of the volume-averaged fibre length, which OA-predictions give the least accurate agreement with the reference.

Table 5.18: Average absolute error values for the OA-results with representative fibre lengths compared to OA-predictions with FLD for SGF Type 2.

Interaction assumption	l_F	**OA-Voigt**	**OA-Reuss**	**OA-SC**
Average absolute error	[μm]	[%]	[%]	[%]
Number-averaged fibre length	392	1.28	1.34	0.74
Stiffness-averaged fibre length	400	0.86	1.10	0.40
Volume-averaged fibre length	461	2.52	1.85	2.98

With this, all examples for the elasto-plastic OA-method are presented. It can be summarised that the method using FLD-information gives good predictions compared to the experimental results. For higher strains, however, where material damage starts to occur in the experiments, the predictions start to overestimate the stress response of the composite. The OA-predictions using single representative fibre lengths all show very good agreement with the OA-predictions using the FLD-information. Due to that and the much higher computational costs in using the full FLD method, it is reasonable to represent the FLD with a single averaged fibre length for engineering predictions. In case of the averaging method to use, the stiffness-averaged fibre length shows the best agreement to the FLD-predictions. However, the difference compared to the other presented averaging methods is not significant for composites studied in this work.

5.3 Fibre-matrix interface debonding

In a final test, the prediction capabilities of the presented Orientation Averaging model is tested considering the effects of fibre-matrix interface debonding in the numerical simulations. It seems unlikely that the surrogate model is capable of representing the effects of reduced interaction length of the fibre and the matrix. Effects, like the reduction in fibre parallel Young’s modulus, cannot be represented. Also, the irreversible damage on the interface is not represented in this method. However, for a uniaxial stress load case, it might be possible to predict the stress response with the current Orientation Averaging model.

The tests are conducted for the PA-GF30 material presented in the Chapters 5.1.2 and 5.2.1 taken from *Holmström et al.* [27]. To model the fibre-matrix interface behaviour, the fibre cylinder wall is connected to the matrix with cohesive surface to surface contact. Additional to the cohesive behaviour, a tangential interaction property is added to introduce friction into the debonded surfaces. The tips of the fibre are not interconnected with cohesive behaviour. The cohesive behaviour is modelled with a linear traction-separation model, using a quadratic damage initiation criterion and the Power Law defining the critical fracture energy as described in Chapter 2.2. To avoid penetration of the fibre and the matrix instances, the tip surfaces are provided with a hard contact interaction. Since no information on the interface parameters is given in *Holmström et al.*, standard values for the interfacial shear strength are assumed, proposed by *Bowyer* and *Bader* [8]. These values have been used for a similar material combination (Polyamide 6 with glass fibre reinforcement) in other literature, and good predictions could be made with them [46]. The critical fracture energies and interface stiffnesses are chosen to ensure a stable simulation outcome. Assuming isotropic interface behaviour, the fracture modes II and III are modelled with the equal parameters. The used model parameters are listed in Table 5.19. Simulations are conducted for a single representative fibre length using the stiffness-averaged fibre length with 373 μm.

Table 5.19: Cohesive zone modelling parameters for PA-GF30 composite.

Property	**Symbol**	**Value**	**Unit**
Normal stiffness	K_I	$1 \cdot 10^5$	N/mm³
Shear stiffness	K_{II}, K_{III}	$1 \cdot 10^5$	N/mm³
Normal interface strength	$\sigma_I^{\max}$	40	MPa
Shear interface strength	$\tau_{II}^{\max}, \tau_{III}^{max}$	45	MPa
Normal critical energy	$G_{C,I}$	9	J/m²
Shear critical energy	$G_{C,II}, G_{C,III}$	9	J/m²
Power Law exponent	α	1.45	-
Tangential friction	μ	0.2	-

5.3.1 Numerical simulations and surrogate model calibration

With the given parameter set, a stable analysis could be conducted. The obtained stress response is presented in Figure 5.35. In the initial stages of all load cases, a linear elastic material response is obtained. The resulting moduli are similar to those obtained from the elasto-plastic simulations. The yield points in the normal load cases are, however, found much earlier in the simulations considering the cohesive behavior. Additionally, a more noticeable gradient reduction is observed in the yield point. It is followed by an initial softening, indicating the start of the interface debonding mechanism.

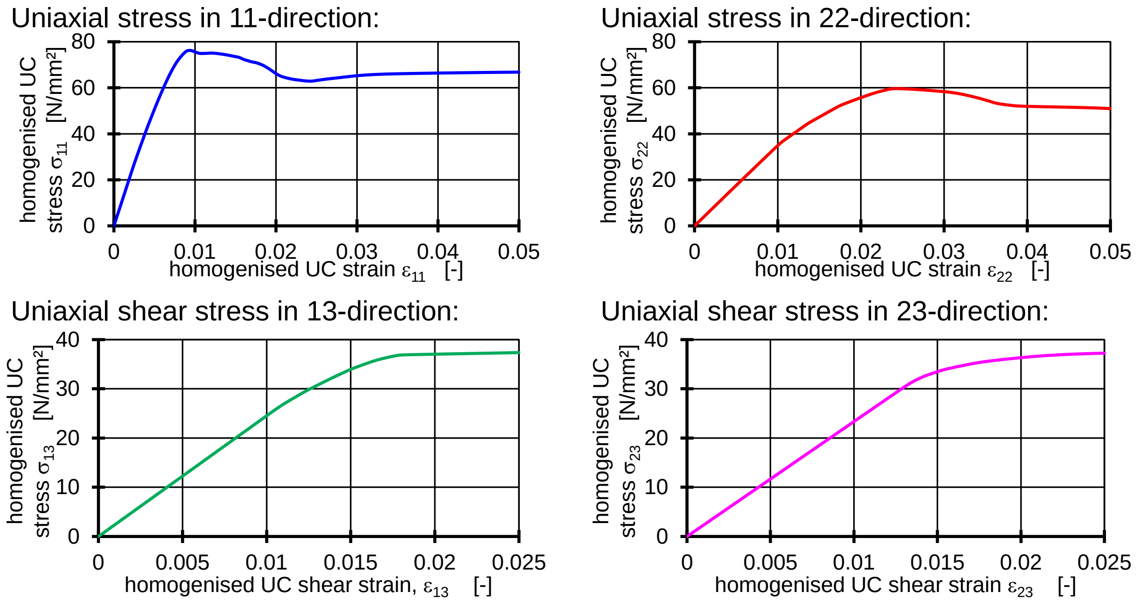

Figure 5.35: Stress strain curves for uniaxial stress loads on a UC including fibre-matrix debonding for the PA-GF30 composite.

The maximum stresses in the normal load cases are not exceeding 80 N/mm² neither the 11-direction nor the 22-direction. Consequently, it can be expected that these values will also not be reached in an Orientation Averaging simulation based on these simulations. With the experimental results having significantly higher stresses, it is obvious that the numerical simulations do not represent the actual damage propagation behaviour in the composite material. It is worth mentioning that a comparable behaviour between uniaxial stress in 11- and 22-direction is observed. This provides the possibility to represent the material behaviour with the surrogate elasto-plastic model. Considering the shear load cases, a good agreement with the easto plastic simulations is found. This indicates that the interfacial shear strength is not exceeded within these load cases.

Reasons for unrepresentative numerical simulations could be the negligence of matrix creeping and damage in the high loaded areas around the fibre tips. Further, with the UC-simulations, fibre-fibre interactions are neglected which have a significant effect on the damage propagation within the composite. Also, the effect of eigen-stresses in the fibre-matrix interface resulting from the processing of the composites, due to the different temperature expansion coefficients might have an effect on the friction between the two constituents after deboning. *Thomason* mentions this effect as a reason for different interface behaviour for varying fibre volume fractions [54]. Also, the parameter set defining the debonding behaviour could be poorly chosen. Increasing the interface strengths and critical fracture energies significantly, however, leads to instabilities in the numerical model. The matrix material becomes subject to large local deformations, especially in the area of the fibre edge. This may be due to the singularity in the edge of the fibre cylinder. Different fibre tip geometries could be tried to eliminate this singularity. Finally, observations on the damage propagation of short fibre reinforced composites show that fibre-matrix debonding is not observed as frequently as expected. Further, the damage behaviour is mainly dominated by matrix micro-cracks starting a the fibre tips and propagating along the fibre axis [7, 53]. Following this, introducing matrix damage behaviour instead of fibre matrix debonding might lead to a more realistic modelling of the material behaviour.

Nevertheless, to describe the homogenised mechanical response of the UC, the surrogate model is fitted to the simulations. The parameter set obtained in the calibration process is presented in Table 5.20. Major differences compared to the model fits considering solely elasto-plastic matrix behaviour are found in the yielding parameters and the hardening rule. Most importantly, the hardening parameter κ_2 should be mentioned. Due to its negative value, softening behaviour is introduced for higher strain loads.

Table 5.20: Surrogate model parameters on UC simulations considering fibre-matrix debonding.

l_F	E	ν	k	σ_y	R	κ_1	κ_2	κ_3
[µm]	[MPa]	[-]	[-]	[N/mm²]	[-]	[-]	[-]	[-]
373	3,203	0.3306	2.593	49.39	1.555	105.5	-4,983	9,992

In analogy to the previously presented calibrations, the model fits are displayed in Figures 5.36 and 5.37. The expected softening behavior can be found in the normal stress load cases. It is

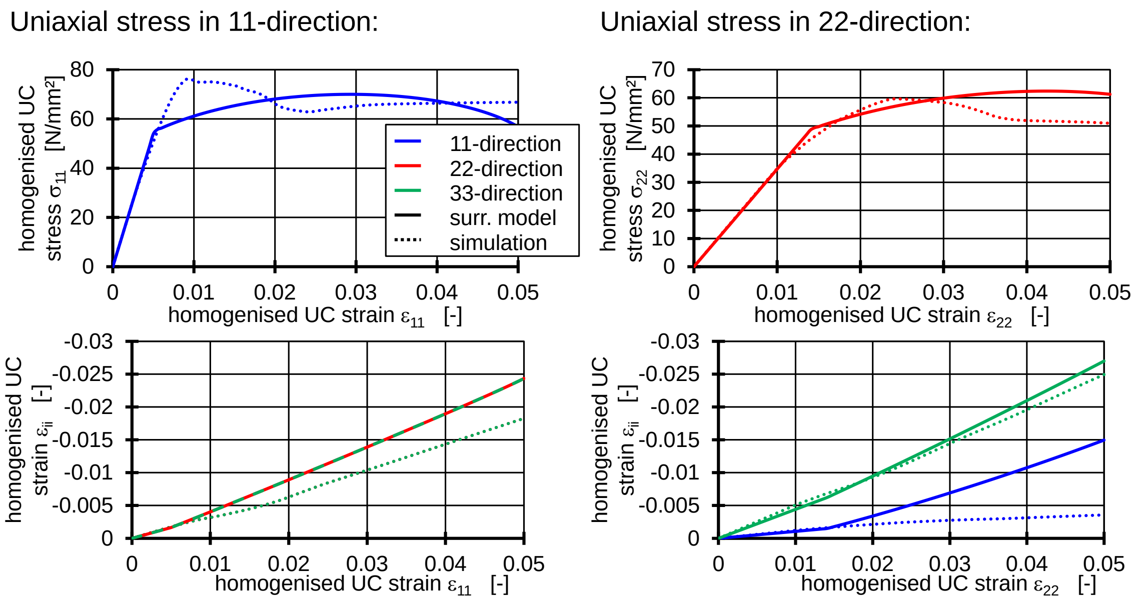

Figure 5.36: Elasto-plastic surrogate model fit on UC-simulation results for the PA-GF30 composite considering fibre-matrix debonding (normal stress case).

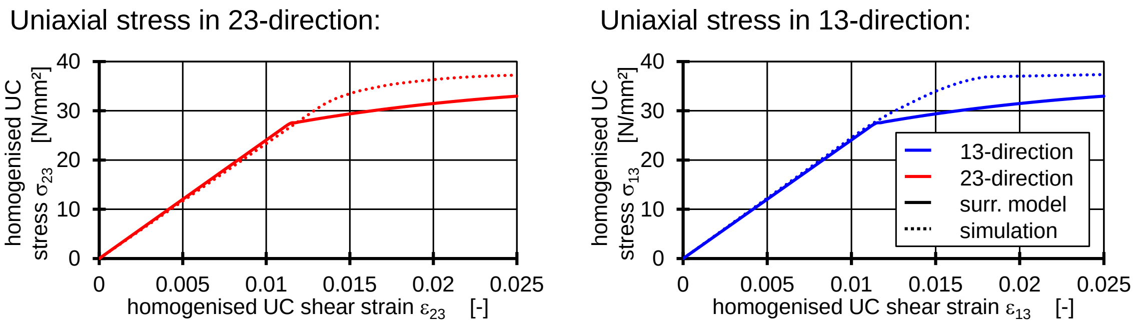

Figure 5.37: Elasto-plastic surrogate model fit on UC-simulation results for the PA-GF30 composite considering fibre-matrix debonding (shear stress case).

obvious that the presented model fit is not fully capable of picturing the material response, obtained from the numerical simulations. Considering the stress response in loading direction for the normal load cases The surrogate model trend is capturing the simulation response relatively well. However, there are some major differences especially in the fibre parallel loading direction (11-direction). The surrogate model shows clear softening for strain levels greater than 0.035 with a decreasing gradient in the stress-strain curve, presumably also for strain values exceeding the investigated range.

The transverse contraction behaviour for the normal load cases produce large errors in comparison to the numerical simulations. The linear elastic response is still captured well, but for increasing strains the surrogate model prediction deviates substantially from the numerical simulation response. In case of the transverse contraction in 33-direction for the 22-direction load case, a good fit is found. Considering the shear load cases, a relatively good fit is found between the numerical simulation and the surrogate model. Although, for the elasto-plastic domain, the homogenised stress response is underpredicted.

The objective function in the linear elastic calibration produces a value of $\epsilon_{fit}^{el} = 7.650 \cdot 10^{-3}$. In the elasto plastic calibration the objective function reaches a value of $\epsilon_{fit}^{pl} = 8.989 \cdot 10^{-2}$. This supports the observation that the linear elastic behaviour is captured well, whereas larger errors occur in the elasto-plastic domain.

5.3.2 Orientation Averaging predictions on PA-GF30

Using the calibrated surrogate model to conduct Orientation Averaging simulations does not promise to give any reasonable estimation of the actual material behaviour. As discussed earlier, the obtained maximum stresses in the numerical simulations are already significantly lower than those obtained from the experimental results. A comparison with results from the literature is, therefore, not considered. Nevertheless, to identify possible difficulties within the Orientation Averaging procedure, the simulations are conducted and presented in the following.

Running the Orientation Averaging simulations, a first observation can be noted. When reaching higher strain values, the computational time for each strain increment increases drastically in case of the Orientation Averaging procedures using the Reuss and the self-consistent assumption. The simulation results are depicted in Figure 5.38. It is observed that for the initial linear elastic behaviour a similar picture is obtained as for the corresponding Orientation Averaging prediction without fibre-matrix debonding. Considering the predicted yielding of the materials for the Voigt and the self-consistent assumption, a good correlation between both points is found at around 37 N/mm². The yield point, predicted with the Reuss assumption is much higher with around 52 N/mm². It is also worth mentioning, that at the yield points both the self-consistent and the Reuss assumption predictions exceed the stress levels of the Voigt assumption for the corresponding strain load. However, for the subsequent strain increments, the stress responses return to the usual order of Voigt predicting the maximal stress response, self-consistent the intermediate and Reuss the minimum.

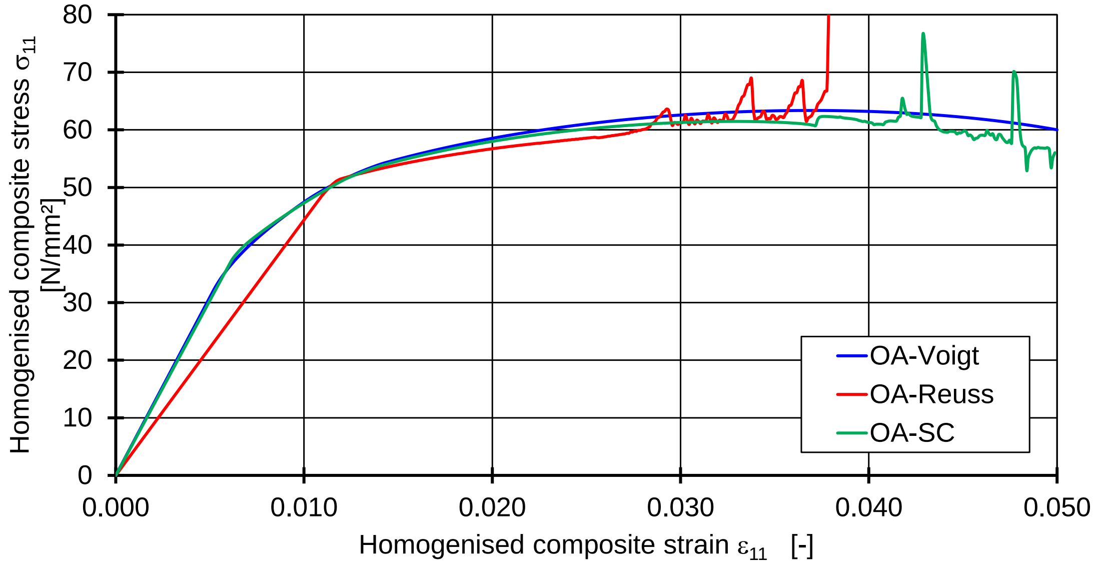

Figure 5.38: Orientation Averagingn predictions for PA-GF30 considering fibre-matrix debonding.

Inspecting the resulting stress-strain responses for higher strain values, reveals several discontinuities for the Reuss and self-consistent assumptions in the strain region where material softening is observed for the UC-simulations. In case of the Reuss interaction assumption, these discontinuities lead to an explosion of the stress response and subsequently to physically unacceptable stress and strain values. Hence, in the Figure, the stress-strain curve for the OA-prediction with Reuss interaction assumption is cut at a strain load of 0.038. The discontinuities in the prediction using the self-consistent assumption do not deviate that much from the expected stress response, compared to the deviations using the Reuss assumption. However, they are still quite significant. Also, these discontinuities in the stress-strain response might be much higher for transverse contractions.

Following this, the transverse contraction response prediction from the Orientation Averaging predictions for all three interaction assumptions is presented in Figure 5.39. Again, attention

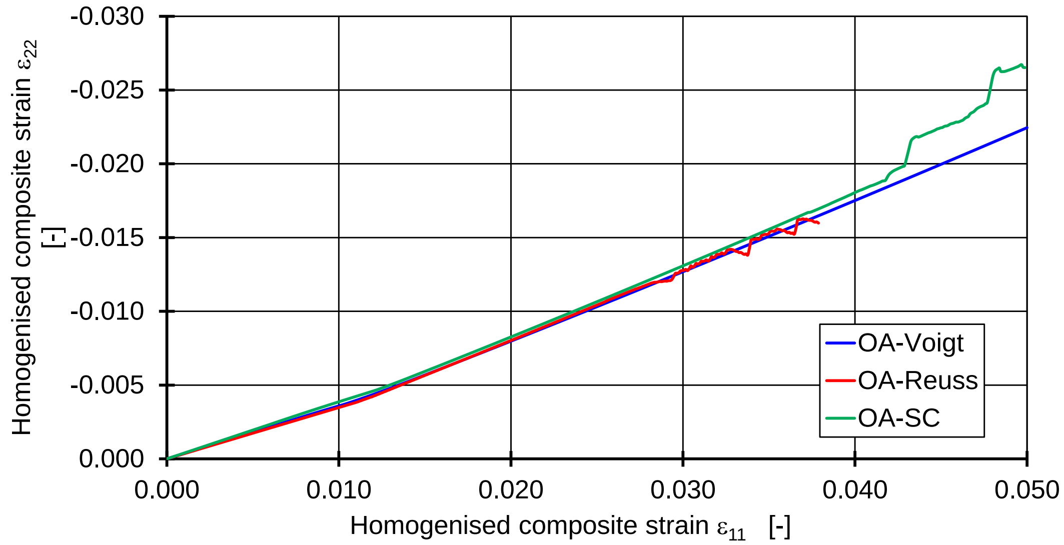

Figure 5.39: Orientation Av eraging predictions for the PA-GF30 composite considering fibre-matrix debonding, transverse contraction.

should be given to the inverted vertical axis of the presented graph. Looking at the initial behaviour of the three different predictions, very similar transverse contraction behaviour is found. At approximately 0.028 strain, discontinuities start to appear in the Reuss-prediction. In this case, however, the deviation from the other two predictions is not significant. For the self-consistant prediction, discontinuities start from a strain level of 0.042. Here, the deviation from the Voigt-prediction is more significant and tends to lower strain levels.

The observed discontinuities are not directly caused by the surrogate material model, otherwise they be observed in the Voigt-prediction as well as in the homogenised material response of the Unit Cell. Hence, the problem might appear from the Orientation Averaging procedure itself. The obtained softening behaviour from the surrogate model results in a change of sign in one of the inverted eigenvalues of the tangent compliance tensor ${}^{4}\boldsymbol{S}^{\tan}$. This can be illustrated with the special case of an FOD producing an orthotropic response in alignment with the global coordinate system. For a uniaxial stress case, the tangent Young's modulus in 11-direction can be considered as $E_{11}^{\tan} = \frac{\delta\sigma_{11}}{\delta\varepsilon_{11}} \approx 0$. At this point, the inverse tangent stiffness entry $\left({}^{4}\boldsymbol{C}^{tan}\right)_{1111}^{-1} = S_{1111}^{tan} = 1/E_{11}^{tan}$ has a singularity, causing numerical errors in the script. Possible sources of errors could be the estimation of the global strain increment. Hence, methods relying on the inverse tangent stiffness produce errors as one or more orientation's surrogate models transit to softening behaviour.

Another point causing issues in the prediction using Reuss assumption is the uniform stress assumption and consequently the estimation of the local UC-strain. For a local stress response greater than the maximum possible stress for a certain fibre orientation., the local UC-strain can not be estimated correctly. An inverse tangent stiffness close to the singularity could, additionally, produce a physically impossible strain in the local constitution and consequently affecting the global constitution as well.

With this, it is clear that the current OA-model is not capable of representing the composite behaviour considering material damage in the form of fibre-matrix debonding. Several issues could be identified that need to be addressed in a future application of these phenomenon to the Orientation Averaging algorithm. First, the numerical model needs to be improved. It should also be investigated in how far fibre-fibre interactions affect the damage propagation mechanism in the composite by using RVE-simulations. Further, the surrogate model needs to be adjusted to account for material damage, resulting in a reduction of elastic composite stiffness as well as in terms of the plastic deformation. And finally, the Orientation Averaging procedure needs some adjustments in terms of handling the material softening. Additionally, further state variables defining the damage state might need to be stored during the simulation. Several analytical models using Orientation Averaging or similar principles have been developed which account for material damage. Many show great correlations with experimental results [11, 12, 29, 46].

6 CONCLUSIONS AND OUTLOOK

In the work presented in this thesis, three methods of representing fibre length distributions in SFRC are elaborated and compared for the linear elastic and the elasto-plastic material behaviour in an Orientation Averaging method.

Two methods are chosen to be investigated in more detail. The first method uses an additional averaging scheme over the fibre lengths and the corresponding material response to obtain the homogenised composite material response. For the second method the material response for an averaged fibre length is obtained using different averaging strategies and with that, the Orientation Averaging is conducted. The averaging methods used are represented by the number-averaged fibre length, the volume-averaged fibre length and a novel approach represented by a stiffness-averaged fibre length. Both methods are implemented in a Python environment, and tested and compared on results from the literature, both for the linear elastic and elasto-plastic material responses.

In case of the linear elastic as well as the elasto-plastic material behaviour, good agreement between the experiments and the model predictions is found. The resulting stress-strain behaviour is captured well by the OA-model, up to a certain strain load. The predictions using representative fibre lengths are compared to the predictions from the method using FLDs. A very good agreement between both models is found. Hence, the use of representative fibre lengths is recommended, due to the high computational costs for the method using FLDs. In terms of which averaging method to use for obtaining the representative fibre length, the number- and stiffness-averaged fibre lengths are identified for producing the best results compared to the OA-method using the FLD. In the elasto-plastic model, the stiffness-averaged fibre length shows a clear trend of producting a closer fit than the number-averaged fibre length.

Further investigation on the presented OA-model is needed, particularly for the elasto-plastic version. The investigations should contain the influence of more advanced hardening rules on the surrogate elasto-plastic model, to improve the representation of the transversal isotropic material behaviour. Further, the model should be extended to represent material damage in addition to the elasto-plastic material behaviour. A first test of modelling fibre matrix debonding with the present model revealed possible difficulties that need to be addressed. Major concerns that are expected lay in the adequate modelling of the failure propagation mechanisms in a single fibre UC, as well as the implementation into the surrogate material model for the homogenisation of the material behaviour.

The computational performance of the model needs to be addressed, too. Improvements could be found in parallelising the Orientation Averaging procedure. Also the number of orientations, considered in this model could be reduced by locally adapting the number of refinements based on the FODF.

ABBREVIATIONS, SYMBOLS AND INDICES

Abbreviations

Abbreviation	**Meaning**
C3SE	Chalmers Centre for Computational Science and Engineering
CFRP	Carbon fibre reinforced plastics
FE	Finite Element
FEM	Finite Element Method
FLD	Fibre Length Distribution
FOD	Fibre Orientation Distribution
FODF	Fibre Orientation Distribution Function
FODT	Fibre Orientation Distribution Tensor
GEV	Generalised Extreme Value (probability distribution)
GF	Glass Fibre
IFD	Injection Flow Direction
LGF	Long Glass Fibre reinforcement
OA	Orientation Averaging
PA	Polyamide
PA-GF15	15 %wt glassfibre reinforced Polyamide
PA-GF30	30 %wt glassfibre reinforced Polyamide
PBC	Periodic Boundary Condition
PBT	Polybutylene Terephthalate
PDF	Probability Density Function
RP	Reference Point
RVE	Representative Volume Element
SC	Self-Consistent
SFRC	Short Fibre Reinforced Composites

SGF	Short Glass Fibre Reinforcement
SLSQP	Sequential Least SQuares Programming
UC	(Single fibre) Unit Cell
UD	UniDirectional (one single fibre direction)

Symbols

Symbol	Unit	Meaning
$\boldsymbol{A}$	[-]	Rotational tensor defining fibre orientation in UC
$\boldsymbol{a}$	[-]	Fibre orientation distribution tensor
α	[-]	Hardening parameter for yield function, Power Law exponent (cohesive zone modelling)
b	[mm]	Width
c	[mm]	Equidistant dimension for UC geometry
$\boldsymbol{C}$	[N/mm²]	Stiffness tensor, either 4th or 2nd order (Voigt notation)
d	[mm]	Diameter
δ	[mm]	Surface separation
E	[N/mm²]	Young’s modulus
$\boldsymbol{E}$	[-]	Eshelby tensor
ε	[-]	Strain
ϵ	[-]	Error value or objective function
η	[-]	dimensionless parameter value in *Halpin-Tsai* model
F	[N]	Force
f	[-]	number-weighted frequency
G	[N/mm²]	Shear modulus
G	[J/m]	Absorbed energy

K	[N/mm²]	Bulk modulus
K	[N/mm³]	Fibre-matrix interface stiffness
k	[-]	Transversal isotropy material parameter
κ	[-]	Material parameter defining the polynomial hardening
H	[N/mm²]	Hardening modulus for linear elasto-plastic hardening
l	[mm]	Length
μ	[-]	Fibre mass fraction
n	[-]	Number of something
ν	[-]	Poisson's ratio
Φ	[-]	Yield function
$\boldsymbol{p}$	[-]	Fibre orientation vector
φ	[-]	Fibre volume fraction
ψ	[-]	Fibre orientation distribution function
ϕ	[-]	Azimuthal angle around 3-axis
q	[-]	Normalising constant
R	[-]	Relating fibre parallel yield stress to isotropic plane
$\boldsymbol{R}$	[-]	Second order rotational tensor
ρ	[kg/mm³]	Density
s	[µm], [-]	Shape parameters for Weibull distribution
$\boldsymbol{S}$	[mm²/N]	Compliance tensor either, 4th or 2nd order (Voigt notation)
τ	[N/mm²]	Shear stress
σ	[N/mm²]	Stress
θ	[-]	Azimuthal angle around 2-axis
u	[mm]	Displacement
w	[-]	Volume-weighted frequency

Indices

Index	Meaning
I, II, III	Interface failure modes I, II and III
4	Indicating a fourth order tensor
C	Global value referring to the composite
crit	Critical value
el	Elastic case
eff	Effective value
f	At failure
fit	Corresponding to an optimisation fit
glob	Tensor in Global coordinate system
HT	*Halpin-Tsai* model
iso	Isotropic case
it	Iteration
loc	Tensor in local coordinate system
max	maximum or maximum possible value
num	Number-averaged value; value, produced with number-averaged fibre length
pl	Plastic case
R	Using the *Reuss* assumption
ref	Refinement steps
rep	Representative value
RP	Referring to a certain Reaction Point
SC	Using the self-consistent assumption
stiff	Sitffness averaged value; value, produced with stiffness-averaged fibre length
UC	Value referring to a Unit Cell (usually in the local coordinate system of the UC)

ult	Ultimate value
V	Using the *Voigt* assumption
vol	Volume-averaged value; value, produced with volume-averaged fibre length
y	Yield point

REFERENCES

[1] Advani, S. G. and Tucker, C. L. 1987. The Use of Tensors to Describe and Predict Fiber Orientation in Short Fiber Composites. *Journal of Rheology* 31, 8, 751–784.

[2] Ashton, J. E., Halpin, J. C., and Petit, P. H. 1969. *Primer on composite materials: analysis*. Technomic Publishing Company.

[3] Bargmann, S., Klusemann, B., Markmann, J., Schnabel, J. E., Schneider, K., Soyarslan, C., and Wilmers, J. 2018. Generation of 3D representative volume elements for heterogeneous materials: A review. *Progress in Materials Science* 96, 322–384.

[4] Bažant, P. and Oh, B. H. 1986. Efficient Numerical Integration on the Surface of a Sphere. *ZAMM - Journal of Applied Mathematics and Mechanics / Zeitschrift für Angewandte Mathematik und Mechanik* 66, 1, 37–49.

[5] Beurden, T.J.H. van. 2019. *Multi-scale modeling of short fiber composites via orientation averaging using self-consistent interaction*. Internship Report, Chalmers University of Technology; Eindhoven University of Technology.

[6] Bingham, C. 1974. An Antipodally Symmetric Distribution on the Sphere. *Ann. Statist.* 2, 6, 1201–1225.

[7] Bourmaud, A., Ausias, G., Lebrun, G., Tachon, M.-L., and Baley, C. 2013. Observation of the structure of a composite polypropylene/flax and damage mechanisms under stress. *Industrial Crops and Products* 43, 225–236.

[8] Bowyer, W. H. and Bader, M. G. 1972. On the re-inforcement of thermoplastics by imperfectly aligned discontinuous fibres. *J Mater Sci* 7, 11, 1315–1321.

[9] Breuer, K. and Stommel, M. 2020. RVE modelling of short fiber reinforced thermoplastics with discrete fiber orientation and fiber length distribution. *SN Appl. Sci.* 2, 91.

[10] Breuer, K., Stommel, M., and Korte, W. 2019. Analysis and Evaluation of Fiber Orientation Reconstruction Methods. *J. Compos. Sci.* 3, 3, 67.

[11] Brighenti, R. 2004. A mechanical model for fiber reinforced composite materials with elasto-plastic matrix and interface debonding. *Computational Materials Science* 29, 4, 475–493.

[12] Brighenti, R. and Scorza, D. 2012. A micro-mechanical model for statistically unidirectional and randomly distributed fibre-reinforced solids. *Mathematics and Mechanics of Solids* 17, 8, 876–893.

[13] Castricum, B., Beurden, T., Mirkhalaf, M., Fagerström, M., and Larsson, F. 2021. A hierarchical coupled multi-scale model for short fiber composites. In *14th WCCM-ECCOMAS Congress*. CIMNE. DOI=10.23967/wccm-eccomas.2020.022.

[14] Castricum, B.A. 2020. *A hierarchical coupled multi-scale model for short fibre-reinforced composites*. Internship Report, Chalmers University of Technology; Eindhoven University of Technology.

[15] Celanese Corporation. 2017. *Celanex 2300 GV1/20. Data Sheet*. http://catalog.ides.com/Datasheet.aspx?I=26793&E=73487.

[16] Chin, W., Liu, H., and Lee, Y. 1988. Effects of fiber length and orientation distribution on the elastic modulus of short fiber reinforced thermoplastics. *Polymer Composites* 9, 27–35.

[17] Cox, H. L. 1952. The elasticity and strength of paper and other fibrous materials. *British Journal of Applied Physics* 3, 3, 72–79.

[18] Eggels, E. H. 2018. *Modeling the mechanical behavior of short fiber composites via orientation averaging*. Internship Report, Chalmers University of Technology; Eindhoven University of Technology.

[19] Eshelby, J.D. 1957. The determination of the elastic field of an ellipsoidal inclusion, and related problems. *Proc. R. Soc. Lond. A* 241, 1226, 376–396.

[20] Fu, S. Y. and Lauke, B. 1998. The elastic modulus of misaligned short-fiber-reinforced polymers. *Composites Science and Technology* 58, 3-4, 389–400.

[21] Fu, S.-Y., Lauke, B., and Mai, Y. W. 2009. *Science and engineering of short fibre reinforced polymers composites*. Woodhead Publishing in materials. Woodhead Publishing, Cambridge, UK, Boca Raton, FL.

[22] Hallett, S. R. and Harper, P. W. 2015. Modelling delamination with cohesive interface elements. In *Numerical Modelling of Failure in Advanced Composite Materials*. Elsevier, 55–72. DOI=10.1016/B978-0-08-100332-9.00002-5.

[23] Halpin, J. C. 1969. Stiffness and Expansion Estimates for Oriented Short Fiber Composites. *Journal of Composite Materials* 3, 732–734.

[24] Harris, C. R., Millman, K. J., Walt, S. J. van der, and Gommers, R. 2020. Array programming with NumPy. *Nature* 585, 7825, 357–362.

[25] Hine, P. J., Lusti, H. R., and Gusev, A. A. 2002. Numerical simulation of the effects of volume fraction, aspect ratio and fibre length distribution on the elastic and thermoelastic properties of short fibre composites. *Composites Science and Technology* 62, 1445–1453.

[26] Holmström, P. H. 2020. *Data for: Anisotropic tensile behaviour of short glass-fibre reinforced polyamide-6*. https://data.mendeley.com/datasets/v6jxkjtrt3/1. Accessed 29 March 2020.

[27] Holmström, P. H., Hopperstad, O. S., and Clausen, A. H. 2020. Anisotropic tensile behaviour of short glass-fibre reinforced polyamide-6. *Composites Part C: Open Access* 2.

[28] ISO International Organization for Standardization. 2019. *Metallic materials - Tensile testing -. Part 1: Method of test at room temperature*. ISO International Organization for Standardization, Vernier, CH, 6892- 1. Accessed 30 January 2020.

[29] Kammoun, S., Doghri, I., Brassart, L., and Delannay, L. 2015. Micromechanical modeling of the progressive failure in short glass–fiber reinforced thermoplastics – First Pseudo-Grain Damage model. *Composites Part A: Applied Science and Manufacturing* 73, 166–175.

[30] Köbler, J., Schneider, M., Ospald, F., Andrä, H., and Müller, R. 2018. Fiber orientation interpolation for the multiscale analysis of short fiber reinforced composite parts. *Comput Mech* 61, 6, 729–750.

[31] Lam, S. K., Pitrou, A., and Seibert, S. 2015. Numba. In *Proceedings of the Second Workshop on the LLVM Compiler Infrastructure in HPC*. ACM, New York, NY, 1–6. DOI=10.1145/2833157.2833162.

[32] Lee, D. J., Oh, H., Song, Y. S., and Youn, J. R. 2012. Analysis of effective elastic modulus for multiphased hybrid composites. *Composites Science and Technology* 72, 2, 278–283.

[33] Lee, D.J., Hwang, S.H., Song, Y.S., and Youn, J.R. 2015. Statistical modeling of effective elastic modulus for multiphased hybrid composites. *Polymer Testing* 41, 99–105.

[34] Lusti, H. 2002. Direct numerical predictions for the elastic and thermoelastic properties of short fibre composites. *Composites Science and Technology* 62, 15, 1927–1934.

[35] McKinney, W. 2010. Data Structures for Statistical Computing in Python. In *Proceedings of the 9th Python in Science Conference*, 56–61. DOI=10.25080/Majora-92bf1922-00a.

[36] Mirkhalaf, S. M. 2021. A finite element based orientation averaging model for predicting elasto-plastic behaviour of short fiber reinforced composites - !!!Under Review!!! *Composites Part B: Engineering*.

[37] Mirkhalaf, S. M., Andrade Pires, F. M., and Simoes, R. 2016. Determination of the size of the Representative Volume Element (RVE) for the simulation of heterogeneous polymers at finite strains. *Finite Elements in Analysis and Design* 119, 30–44.

[38] Mirkhalaf, S. M., Eggels, E., Anantharanga, A. T., Larsson, F., and Fagerström, M. 2019. Short fiber composites: computational homoginisation vs. orientation averaging. In *ICCM22*, Melbourne, Autralia.

[39] Mirkhalaf, S.M., Eggels, E.H., Beurden, T.J.H. van, Larsson, F., and Fagerström, M. 2020. A finite element based orientation averaging method for predicting elastic properties of short fiber reinforced composites. *Composites Part B: Engineering* 202.

[40] Modniks, J. and Andersons, J. 2010. Modeling elastic properties of short flax fiber-reinforced composites by orientation averaging. *Computational Materials Science* 50, 2, 595–599.

[41] Mori, T. and Tanaka, K. 1973. Average stress in matrix and average elastic energy of materials with misfitting inclusions. *Acta Metallurgica* 21, 5, 571–574.

[42] Mortazavian, S. and Fatemi, A. 2015. Effects of fiber orientation and anisotropy on tensile strength and elastic modulus of short fiber reinforced polymer composites. *Composites Part B: Engineering* 72, 116–129.

[43] MSC Software company. 2019. *Digimat*. *User's Manual*, Newport Beach, CA, USA.

[44] Müller, V., Brylka, B., Dillenberger, F., Glöckner, R., Kolling, S., and Böhlke, T. 2016. Homogenization of elastic properties of short-fiber reinforced composites based on measured microstructure data. *Journal of Composite Materials* 50, 3, 297–312.

[45] Nguyen, B. N., Bapanapalli, S. K., Holbery, J. D., Smith, M. T., Kunc, V., Frame, B. J., Phelps, J. H., and Tucker, C. L. 2008. Fiber Length and Orientation in Long-Fiber Injection-Molded Thermoplastics. Part I: Modeling of Microstructure and Elastic Properties. *Journal of Composite Materials* 42, 10, 1003–1029.

[46] Notta-Cuvier, D., Lauro, F., and Bennani, B. 2015. Modelling of progressive fibre/matrix debonding in short-fibre reinforced composites up to failure. *International Journal of Solids and Structures* 66, 140–150.

[47] Onat, E. T. and Leckie, F. A. 1988. Representation of Mechanical Behavior in the Presence of Changing Internal Structure. *Journal of Applied Mechanics* 55, 1, 1–10.

[48] Overvelde, J.T.B. 2015. *Periodic Boundary Conditions in Abaqus*. http://www.overvelde.com/downloads/. Accessed 16 November 2020.

[49] Pierard, O., Friebel, C., and Doghri, I. 2004. Mean-field homogenization of multi-phase thermo-elastic composites: a general framework and its validation. *Composites Science and Technology* 64, 10, 1587–1603.

[50] Runesson, K., Steinmann, P., Ekh, M., and Menzel, A. 2019. *Constitutive Modeling of Engineering Materials*. *Theory and Computation*.

[51] S. H. Munson-Mcgee and R. L. McCullough. 1994. Orientation parameters for the specification of effective properties of heterogeneous materials. *Polymer Engineering & Science* 34, 4, 361–370.

[52] Sasayama, T., Okabe, T., Aoyagi, Y., and Nishikawa, M. 2013. Prediction of failure properties of injection-molded short glass fiber-reinforced polyamide 6,6. *Composites Part A: Applied Science and Manufacturing* 52, 45–54.

[53] Sato, N., Kurauchi, T., Sato, S., and Kamigaito, O. 1991. Microfailure behaviour of randomly dispersed short fibre reinforced thermoplastic composites obtained by direct SEM observation. *J Mater Sci* 26, 14, 3891–3898.

[54] Thomason, J. L. 2001. Micromechanical parameters from macromechanical measurements on glass reinforced polyamide 6,6. *Composites Science and Technology* 61, 14, 2007–2016.

[55] Tian, W., Qi, L., Zhou, J., Liang, J., and Ma, Y. 2015. Representative volume element for composites reinforced by spatially randomly distributed discontinuous fibers and its applications. *Composite Structures* 131, 366–373.

[56] Toray Industries. 2013. *PA66-GF30. data sheet*. http://product.toray.com/en_plastics/detail.x?uriNo=1040. Accessed 29 March 2021.

[57] Virtanen, P., Gommers, R., Oliphant, T. E., Haberland, M., Reddy, T., and Cournapeau, D. 2020. SciPy 1.0: Fundamental Algorithms for Scientific Computing in Python. *Nature Methods* 17, 261–272.

A TENSOR NOTATION AND OPERATIONS

In this chapter, the used convention for tensor notation and all mentioned tensor operations in this work are listed and explained. Examples are given in using the tensor notation and *Einstein* convention. The operators used are in agreement with *Runesson et al. 2019* [50].

The tensors used in this work are of first order (vectors), second order and fourth order. All tensors used in the presented equations are written as bold letters. Other symbols are to be considered as scalar values. Vectors are represented by a lower-case letter ($\boldsymbol{a}$), whereas for second and fourth order tensors capital letters are used ($\boldsymbol{B},\ \boldsymbol{\Lambda}$). To distinguish between second and fourth order tensors, the latter ones are marked with a 4 in the upper left of the symbol (${}^4\boldsymbol{C}$).

Table A.1: Explanation and examples on the used tensor operations in this work.

Operator	Explanation	Examples
$\cdot$	<u>*Single contraction product or vector product:*</u> Summation over the last index of the first constituent and the first index of the second constituent. Operation results in a tesor of the sum of the first and second constituents orders minus two.	$c = \boldsymbol{a} \cdot \boldsymbol{b}$ $c = a_i b_i$ $\boldsymbol{c} = \boldsymbol{A} \cdot \boldsymbol{b}$ $c_i = a_{ij} b_j$ $\boldsymbol{C} = \boldsymbol{A} \cdot \boldsymbol{B}$ $c_{ik} = a_{ij} b_{jk}$
$:$	<u>*Double contraction product or matrix product:*</u> Summation over the last two indices of the first constituent and the first two indices of the second constituent. Operation results in a tesor of the sum of the first and second constituents orders minus four.	$c = \boldsymbol{A} : \boldsymbol{B}$ $c = a_{ij} b_{ij}$ $\boldsymbol{C} = {}^4\boldsymbol{A} : \boldsymbol{B}$ $c_{ij} = a_{ijkl} b_{kl}$ ${}^4\boldsymbol{C} = {}^4\boldsymbol{A} : {}^4\boldsymbol{B}$ $c_{ijmn} = a_{ijkl} b_{klmn}$
$\otimes$	<u>*Open product or dyadic product:*</u> Combination of both tensors of order n and m to a tensor of order $(n+m)$	$\boldsymbol{C} = \boldsymbol{a} \otimes \boldsymbol{b}$ $c_{ij} = a_i b_j$ ${}^4\boldsymbol{C} = \boldsymbol{A} \otimes \boldsymbol{B}$ $c_{ijkl} = a_{ij} b_{kl}$
$\overline{\otimes}$	<u>*Non-standard open product:*</u> Open product of two second order tesors with additional transformation in the second and third index of the resulting tensor.	${}^4\boldsymbol{C} = \boldsymbol{A} \,\overline{\otimes}\, \boldsymbol{B}$ $c_{ijkl} = a_{ik} b_{jl}$
$\boldsymbol{X}^T$	<u>*Tensor transposition:*</u> Operation is only used for 2nd order tensors $\boldsymbol{X}$ in this work. Transposing the tensor results in a mirror image of it with the diagonal from the upper left entry as mirroring axis.	$\boldsymbol{B} = \boldsymbol{A}^T$ $b_{ij} = a_{ji}$

$\boldsymbol{X}^{-1}$	*Tensor inversion:* Operation which creates the opposing tensor of the same order, which, when applied in a product operation, maintaining the tensor order, results in a unit tensor $\boldsymbol{I}$. For a second order tensor this operation is the single contraction, and for the fourth order product, it is the double contraction product.	$\boldsymbol{B} = \boldsymbol{A}^{-1}$ $\boldsymbol{I} = \boldsymbol{B} \cdot \boldsymbol{A}$ $\delta_{ik} = b_{ij}a_{jk}$
		${}^4\boldsymbol{B} = {}^4\boldsymbol{A}^{-1}$ ${}^4\boldsymbol{I} = {}^4\boldsymbol{B} : {}^4\boldsymbol{A}$ $\delta_{in}\delta_{jm} = b_{ijkl}a_{klmn}$
		Kronecker delta δ_{ij}: $\delta_{ij} := \begin{cases} 1, & \text{if } i = j \\ 0, & \text{else} \end{cases}$
$\lVert\boldsymbol{X}\rVert$	*Tensor norm:* Reducing the tensor to a single value; in analogy to the vector norm being the length of the vector	$\lVert\boldsymbol{A}\rVert = \sqrt{\sum_i \sum_j A_{ij}^2}$

B PARAMETER FITS OF THE SURROGATE MODELS FOR THE PRESENTED MATERIALS

***Holmström, Hopperstad et al. 2020* [27]:**

PA-GF15:

Table B.1: Surrogate model parameters fits for the different fibre length classes for PA-GF15 from [27].

l_F	ϵ_{fit}^{el}	ϵ_{fit}^{pl}	E	ν	k	σ_y	R	κ_1	κ_2	κ_3
[µm]	[-]	[-]	[MPa]	[-]	[-]	[N/mm²]	[-]	[-]	[-]	[-]
50	$3.264 \cdot 10^{-2}$	$3.845 \cdot 10^{-2}$	2,993	0.3046	1.300	61.33	1.463	20.38	0.000	0.0000
150	$3.748 \cdot 10^{-2}$	$2.735 \cdot 10^{-2}$	3,041	0.3225	1.504	64.24	2.333	38.66	68.24	0.0066
250	$2.420 \cdot 10^{-2}$	$1.834 \cdot 10^{-2}$	3,052	0.3347	1.609	65.13	3.818	30.70	943.0	22.12
350	$1.657 \cdot 10^{-2}$	$9.410 \cdot 10^{-3}$	3,059	0.3441	1.648	65.52	5.402	25.70	1,008	125.4
450	$1.186 \cdot 10^{-2}$	$6.227 \cdot 10^{-3}$	3,066	0.3515	1.661	65.77	6.618	23.73	1,074	135.9
550	$8.787 \cdot 10^{-3}$	$5.382 \cdot 10^{-3}$	3,072	0.3576	1.664	65.91	7.525	23.48	1,116	182.1
650	$6.659 \cdot 10^{-3}$	$5.123 \cdot 10^{-3}$	3,077	0.3626	1.662	65.98	8.220	23.11	1,205	194.2
750	$5.078 \cdot 10^{-3}$	$5.052 \cdot 10^{-3}$	3,082	0.3669	1.657	66.05	8.834	22.62	1,245	212.8
850	$3.922 \cdot 10^{-3}$	$5.012 \cdot 10^{-3}$	3,086	0.3705	1.652	66.10	9.374	22.71	1,227	316.1
950	$3.055 \cdot 10^{-3}$	$5.026 \cdot 10^{-3}$	3,089	0.3737	1.647	66.15	9.747	22.41	1,316	328.5
1,050	$2.367 \cdot 10^{-3}$	$5.087 \cdot 10^{-3}$	3,091	0.3764	1.641	66.21	10.20	21.65	1,316	328.5
1,150	$1.901 \cdot 10^{-3}$	$5.132 \cdot 10^{-3}$	3,094	0.3788	1.636	66.21	10.58	22.40	1,254	392.5

Averaged fibre lengths:

Table B.2: Surrogate model parameters fits for the representative fibre lengths for PA-GF15 from [27].

l_F	ϵ_{fit}^{el}	ϵ_{fit}^{pl}	E	ν	k	σ_y	R	κ_1	κ_2	κ_3
[µm]	[-]	[-]	[MPa]	[-]	[-]	[N/mm²]	[-]	[-]	[-]	[-]
430	$4.139 \cdot 10^{-4}$	$1.490 \cdot 10^{-2}$	3,119	0.3971	1.487	65.74	6.396	38.72	0.000	110.8
443	$4.247 \cdot 10^{-4}$	$1.439 \cdot 10^{-2}$	3,119	0.3973	1.489	65.76	6.510	38.87	0.000	110.9
532	$4.656 \cdot 10^{-4}$	$1.198 \cdot 10^{-2}$	3,121	0.3983	1.501	65.86	7.241	36.14	250.0	112.5

PA-GF30:

Table B.3: Surrogate model parameters fits for the different fibre length classes for PA-GF30 from [27].

l_F	ϵ_{fit}^{el}	ϵ_{fit}^{pl}	E	ν	k	σ_y	R	κ_1	κ_2	κ_3
[µm]	[-]	[-]	[MPa]	[-]	[-]	[N/mm²]	[-]	[-]	[-]	[-]
50	$9.161 \cdot 10^{-3}$	$6.879 \cdot 10^{-3}$	3,620	0.3543	1.536	62.15	2.690	38.40	0.000	0.000
150	$4.807 \cdot 10^{-3}$	$6.603 \cdot 10^{-3}$	3,602	0.3701	1.940	63.97	7.794	44.78	88.60	86.83
250	$3.306 \cdot 10^{-3}$	$6.891 \cdot 10^{-3}$	3,601	0.3768	2.063	64.40	12.01	38.03	1,033	208.8
350	$2.541 \cdot 10^{-3}$	$7.606 \cdot 10^{-3}$	3,604	0.3822	2.107	64.56	15.85	34.71	1,285	138.7
450	$2.198 \cdot 10^{-3}$	$8.152 \cdot 10^{-3}$	3,608	0.3866	2.122	64.66	19.22	33.81	1,267	1,948
550	$2.238 \cdot 10^{-3}$	$8.867 \cdot 10^{-3}$	3,615	0.3932	2.101	64.72	22.22	33.62	1,248	1,117
650	$2.423 \cdot 10^{-3}$	$9.199 \cdot 10^{-3}$	3,617	0.3958	2.102	64.76	24.91	33.65	1,188	1,412
750	$2.682 \cdot 10^{-3}$	$9.514 \cdot 10^{-3}$	3,619	0.3982	2.098	64.80	27.20	33.77	1,156	1,614
850	$2.975 \cdot 10^{-3}$	$9.887 \cdot 10^{-3}$	3,621	0.4001	2.093	64.73	29.28	35.43	1,031	1,971
950	$3.278 \cdot 10^{-3}$	$1.008 \cdot 10^{-2}$	3,622	0.4018	2.088	64.77	31.25	35.82	964.4	1,657
1,050	$3.598 \cdot 10^{-3}$	$1.033 \cdot 10^{-2}$	3,624	0.4034	2.081	64.76	32.99	36.11	919.9	2,000
1,150	$3.891 \cdot 10^{-3}$	$1.049 \cdot 10^{-2}$	3,625	0.4047	2.077	64.80	34.65	36.22	874.8	1,647

Averaged fibre lengths:

Table B.4: Surrogate model parameters fits for the representative fibre lengths for PA-GF30 from [27].

l_F	ϵ_{fit}^{el}	ϵ_{fit}^{pl}	E	ν	k	σ_y	R	κ_1	κ_2	κ_3
[µm]	[-]	[-]	[MPa]	[-]	[-]	[N/mm²]	[-]	[-]	[-]	[-]
366	$2.257 \cdot 10^{-2}$	$7.954 \cdot 10^{-3}$	3,543	0.3377	2.428	64.58	16.06	38.22	1,417	457.5
372	$2.255 \cdot 10^{-2}$	$8.009 \cdot 10^{-3}$	3,542	0.3376	2.434	64.61	16.26	37.83	1,470	28.32
425	$2.253 \cdot 10^{-2}$	$8.278 \cdot 10^{-3}$	3,542	0.3379	2.463	64.64	17.71	37.35	1,652	153.2

Sasayama, Okabe et al. 2013 **[52]:**

Table B.5: Surrogate model parameters fits for the different fibre length classes for the glass fibre reinforced Polyamide-6.6 composite from [52].

l_F	ϵ_{fit}^{el}	ϵ_{fit}^{pl}	E	ν	k	σ_y	R	κ_1	κ_2	κ_3
[µm]	[-]	[-]	[MPa]	[-]	[-]	[N/mm²]	[-]	[-]	[-]	[-]
100	$4.188 \cdot 10^{-3}$	$1.003 \cdot 10^{-2}$	3,741	0.3364	1.940	77.64	4.571	57.01	0.000	965.5
150	$5.500 \cdot 10^{-3}$	$1.149 \cdot 10^{-2}$	3,733	0.3408	2.138	78.25	6.207	55.52	374.9	1,002
200	$6.540 \cdot 10^{-3}$	$1.259 \cdot 10^{-2}$	3,731	0.3437	2.263	78.53	7.660	52.00	785.4	1,002
250	$7.110 \cdot 10^{-3}$	$1.323 \cdot 10^{-2}$	3,727	0.3450	2.356	78.77	8.979	49.53	1,034	1,029
300	$7.490 \cdot 10^{-3}$	$1.375 \cdot 10^{-2}$	3,726	0.3459	2.425	78.86	10.10	48.93	1,241	1,032
350	$7.648 \cdot 10^{-3}$	$1.395 \cdot 10^{-2}$	3,724	0.3461	2.482	78.98	11.25	47.80	1,329	1,077
400	$7.672 \cdot 10^{-3}$	$1.407 \cdot 10^{-2}$	3,723	0.3461	2.527	79.01	12.35	47.18	1,376	1,076
450	$7.585 \cdot 10^{-3}$	$1.406 \cdot 10^{-2}$	3,721	0.3458	2.566	79.07	13.26	46.95	1,491	1,143
500	$7.420 \cdot 10^{-3}$	$1.393 \cdot 10^{-2}$	3,719	0.3452	2.603	79.15	14.27	46.51	1,471	1,522
550	$7.235 \cdot 10^{-3}$	$1.383 \cdot 10^{-2}$	3,717	0.3447	2.634	79.18	15.08	46.12	1,574	1,223
600	$7.069 \cdot 10^{-3}$	$1.374 \cdot 10^{-2}$	3,716	0.3443	2.659	79.17	16.02	46.33	1,533	1,504
650	$6.868 \cdot 10^{-3}$	$1.355 \cdot 10^{-2}$	3,714	0.3437	2.685	79.24	16.96	45.80	1,492	1,552
700	$6.689 \cdot 10^{-3}$	$1.339 \cdot 10^{-2}$	3,713	0.3431	2.706	79.26	17.65	45.85	1,563	1,451
750	$6.517 \cdot 10^{-3}$	$1.326 \cdot 10^{-2}$	3,712	0.3426	2.726	79.28	18.53	45.56	1,521	1,519
800	$6.380 \cdot 10^{-3}$	$1.318 \cdot 10^{-2}$	3,712	0.3423	2.742	79.26	19.18	46.12	1,550	1,431
850	$6.224 \cdot 10^{-3}$	$1.300 \cdot 10^{-2}$	3,710	0.3417	2.759	79.31	20.04	45.63	1,498	1,510
900	$6.114 \cdot 10^{-3}$	$1.292 \cdot 10^{-2}$	3,710	0.3415	2.771	79.28	20.65	46.24	1,518	1,497
950	$5.984 \cdot 10^{-3}$	$1.275 \cdot 10^{-2}$	3,709	0.3410	2.786	79.33	21.48	45.80	1,456	1,559
1,000	$5.895 \cdot 10^{-3}$	$1.268 \cdot 10^{-2}$	3,709	0.3408	2.796	79.31	22.14	46.99	1,349	3,326
1,050	$5.785 \cdot 10^{-3}$	$1.253 \cdot 10^{-2}$	3,707	0.3403	2.808	79.35	22.85	46.32	1,348	3,425
1,100	$5.695 \cdot 10^{-3}$	$1.244 \cdot 10^{-2}$	3,707	0.3400	2.818	79.36	23.41	46.29	1,374	3,168
1,150	$5.634 \cdot 10^{-3}$	$1.240 \cdot 10^{-2}$	3,707	0.3399	2.826	79.33	23.87	46.31	1,404	5,000
1,200	$5.570 \cdot 10^{-3}$	$1.234 \cdot 10^{-2}$	3,707	0.3397	2.834	79.34	24.70	46.95	1,294	3,003
1,250	$5.492 \cdot 10^{-3}$	$1.221 \cdot 10^{-2}$	3,706	0.3394	2.844	79.38	25.20	46.65	1,320	3,025
1,300	$5.431 \cdot 10^{-3}$	$1.214 \cdot 10^{-2}$	3,705	0.3392	2.851	79.39	25.51	45.65	1,449	4,991
1,350	$5.396 \cdot 10^{-3}$	$1.213 \cdot 10^{-2}$	3,705	0.3391	2.856	79.36	26.43	47.35	1,227	3,023
1,400	$5.355 \cdot 10^{-3}$	$1.208 \cdot 10^{-2}$	3,705	0.3390	2.862	79.36	26.96	47.92	1,170	3,264

1,450	$5.297 \cdot 10^{-3}$	$1.075 \cdot 10^{-2}$	3,704	0.3387	2.869	66.08	34.46	52.19	1,117	3,342
1,500	$5.272 \cdot 10^{-3}$	$1.200 \cdot 10^{-2}$	3,705	0.3387	2.874	79.37	28.05	47.51	1,169	3,006
1,550	$5.224 \cdot 10^{-3}$	$1.187 \cdot 10^{-2}$	3,704	0.3385	2.880	79.42	28.49	47.63	1,162	3,067
1,600	$5.209 \cdot 10^{-3}$	$1.188 \cdot 10^{-2}$	3,704	0.3385	2.883	79.38	28.91	48.03	1,155	3,048
1,650	$5.186 \cdot 10^{-3}$	$1.185 \cdot 10^{-2}$	3,704	0.3384	2.887	79.39	29.69	48.09	1,053	3,026
1,700	$5.161 \cdot 10^{-3}$	$1.183 \cdot 10^{-2}$2	3,704	0.3383	2.892	79.39	30.06	48.38	1,052	3,010
1,750	$5.123 \cdot 10^{-3}$	$1.172 \cdot 10^{-2}$	3,703	0.3381	2.897	79.43	30.43	48.19	1,074	3,000
1,800	$5.096 \cdot 10^{-3}$	$1.168 \cdot 10^{-2}$	3,703	0.3380	2.901	79.43	30.76	48.33	1,081	3,000
1,850	$5.068 \cdot 10^{-3}$	$1.166 \cdot 10^{-2}$	3,703	0.3379	2.905	79.44	31.53	48.16	990.7	2,998
1,900	$5.070 \cdot 10^{-3}$	$1.168 \cdot 10^{-2}$	3,703	0.3380	2.906	79.40	31.90	49.11	950.7	3,019
1,950	$5.059 \cdot 10^{-3}$	$1.166 \cdot 10^{-2}$	3,703	0.3380	2.909	79.41	32.19	49.22	964.6	3,019
2,000	$5.046 \cdot 10^{-3}$	$1.165 \cdot 10^{-2}$	3,703	0.3379	2.913	79.41	32.73	49.40	906.2	3,032
2,050	$5.018 \cdot 10^{-3}$	$1.155 \cdot 10^{-2}$	3,702	0.3377	2.916	79.45	33.55	50.60	696.6	3,009
2,100	$5.022 \cdot 10^{-3}$	$1.158 \cdot 10^{-2}$	3,703	0.3378	2.917	79.41	33.62	49.65	856.1	3,082
2,150	$4.992 \cdot 10^{-3}$	$1.150 \cdot 10^{-2}$	3,702	0.3376	2.921	79.45	34.07	49.52	822.2	3,049
2,200	$5.000 \cdot 10^{-3}$	$1.154 \cdot 10^{-2}$	3,702	0.3377	2.922	79.42	34.43	50.03	801.5	3,030
2,250	$4.969 \cdot 10^{-3}$	$1.147 \cdot 10^{-2}$	3,702	0.3376	2.927	79.46	34.32	47.53	1,076	3,000
2,300	$4.954 \cdot 10^{-3}$	$1.145 \cdot 10^{-2}$	3,702	0.3375	2.929	79.46	34.67	47.92	1,044	2,999
2,350	$4.965 \cdot 10^{-3}$	$1.150 \cdot 10^{-2}$	3,702	0.3376	2.930	79.42	34.90	48.16	1,071	3,000
2,400	$4.962 \cdot 10^{-3}$	$1.149 \cdot 10^{-2}$	3,702	0.3376	2.931	79.43	35.78	46.69	1,053	2,999
2,450	$4.935 \cdot 10^{-3}$	$1.140 \cdot 10^{-2}$	3,701	0.3374	2.935	79.46	35.93	46.74	1,056	3,024
2,500	$4.913 \cdot 10^{-3}$	$1.184 \cdot 10^{-2}$	3,702	0.3375	2.935	79.43	36.79	52.91	713.2	3,260

Averaged fibre lengths LGF Type 1:

Table B.6: Surrogate model parameters fits for the representative fibre lengths for the glass fibre reinforced Polyamide-6.6 composite from [52], specimen LGF Type 1.

l_F	ϵ_{fit}^{el}	ϵ_{fit}^{pl}	E	ν	k	σ_y	R	κ_1	κ_2	κ_3
[µm]	[-]	[-]	[MPa]	[-]	[-]	[N/mm²]	[-]	[-]	[-]	[-]
542	$2.733 \cdot 10^{-3}$	$7.774 \cdot 10^{-3}$	3,669	0.3088	2.888	79.17	14.83	49.80	1,917	234.4
562	$3.443 \cdot 10^{-3}$	$7.126 \cdot 10^{-3}$	3,658	0.3031	2.945	79.15	15.07	50.05	2,004	157.4
862	$2.679 \cdot 10^{-3}$	$8.975 \cdot 10^{-3}$	3,667	0.3095	3.009	79.27	19.04	50.63	2,486	171.5

Averaged fibre lengths LGF Type 2:

Table B.7: Surrogate model parameters fits for the representative fibre lengths for the glass fibre reinforced Polyamide-6.6 composite from [52], specimen LGF Type 2.

l_F	ϵ_{fit}^{el}	ϵ_{fit}^{pl}	E	ν	k	σ_y	R	κ_1	κ_2	κ_3
[µm]	[-]	[-]	[MPa]	[-]	[-]	[N/mm²]	[-]	[-]	[-]	[-]
590	$2.720 \cdot 10^{-3}$	$7.905 \cdot 10^{-3}$	3,668	0.3090	2.914	79.20	15.71	49.94	1,918	455.0
607	$2.721 \cdot 10^{-3}$	$8.011 \cdot 10^{-3}$	3,669	0.3091	2.922	79.18	15.95	50.13	1,968	155.9
795	$2.682 \cdot 10^{-3}$	$8.640 \cdot 10^{-3}$	3,667	0.3093	2.991	79.29	18.27	50.09	2,402	169.6

Averaged fibre lengths SGF Type 1:

Table B.8: Surrogate model parameters fits for the representative fibre lengths for the glass fibre reinforced Polyamide-6.6 composite from [52], specimen SGF Type 1.

l_F	ϵ_{fit}^{el}	ϵ_{fit}^{pl}	E	ν	k	σ_y	R	κ_1	κ_2	κ_3
[µm]	[-]	[-]	[MPa]	[-]	[-]	[N/mm²]	[-]	[-]	[-]	[-]
385	$2.797 \cdot 10^{-3}$	$7.476 \cdot 10^{-3}$	3,672	0.3085	2.771	78.99	11.72	49.74	1,736	1,992
398	$2.785 \cdot 10^{-3}$	$7.445 \cdot 10^{-3}$	3,671	0.3084	2.783	79.04	11.94	49.05	1,854	274.9
478	$2.753 \cdot 10^{-3}$	$7.619 \cdot 10^{-3}$	3,670	0.3087	2.848	79.13	13.57	49.08	1,972	155.0

Averaged fibre lengths SGF Type 2:

Table B.9: Surrogate model parameters fits for the representative fibre lengths for the glass fibre reinforced Polyamide-6.6 composite from [52], specimen SGF Type 2.

l_F	ϵ_{fit}^{el}	ϵ_{fit}^{pl}	E	ν	k	σ_y	R	κ_1	κ_2	κ_3
[µm]	[-]	[-]	[MPa]	[-]	[-]	[N/mm²]	[-]	[-]	[-]	[-]
392	$2.796 \cdot 10^{-3}$	$7.477 \cdot 10^{-3}$	3,672	0.3085	2.776	79.00	11.84	49.49	1,807	347.6
400	$2.784 \cdot 10^{-3}$	$7.450 \cdot 10^{-3}$	3,671	0.3084	2.785	79.05	12.00	49.07	1,858	366.5
461	$2.759 \cdot 10^{-3}$	$7.579 \cdot 10^{-3}$	3,670	0.3086	2.836	79.11	13.26	49.04	1,938	154.5

DEPARTMENT OF INDUSTRIAL AND MATERIALS SCIENCE
CHALMERS UNIVERSITY OF TECHNOLOGY
Gothenburg, Sweden
www.chalmers.se

CHALMERS
UNIVERSITY OF TECHNOLOGY